



**NTNU – Trondheim**  
Norwegian University of  
Science and Technology

# In-situ Compression Testing of Nanosized Pillars

**Anette Brocks Hagen**

Materials Technology

Submission date: June 2014

Supervisor: Christian Thaulow, IPM

Norwegian University of Science and Technology  
Department of Engineering Design and Materials



## **Problem text**

THE NORWEGIAN UNIVERSITY  
OF SCIENCE AND TECHNOLOGY  
DEPARTMENT OF ENGINEERING DESIGN  
AND MATERIALS

### **MASTER THESIS 2014 FOR STUD.TECHN. ANETTE BROCKS HAGEN**

#### **IN-SITU COMPRESSION TESTING OF NANOSIZED PILLARS**

In-situ prøving av nano-pillarer

The activity in the Arctic areas is on the increase. 25 % of the worlds undiscovered oil and natural gas are believed to be located in the northern area. The exploration of these areas requires high quality materials due to the harsh climate conditions and low temperatures down to  $-60^{\circ}\text{C}$ . Understanding material deformation mechanisms under these environmental conditions can help prevent dangerous failure from occurring and allow for the development of both strong and cost-efficient materials. In order to be able to understand the local properties of complex microstructures required for arctic conditions, it is crucial to understand the fundamental deformation mechanisms of pure single crystals like pure Fe. The rapid developments within nanotechnology have made it possible to get a detailed characterization of the material by means of different nanomechanical testing methods.

During this work, the following process will be conducted:

- Sample preparation for metallographic examination, EBSD- and FIB analysis
- Determination of grain boundary orientations with EBSD examinations.
- Machine pillars in micro- and nanosize with Focused Ion Beam at NTNU Nanolab from selected areas within the crystalline material. In this way, very precise mechanical properties can be obtained.
- Nanocompression with a Picoindenter mounted inside a SEM in order to continuously observe the process of deformation. By using a cooling system consisting of a liquid-nitrogen cold finger, the pillar compression shall be conducted at low temperatures ( $-60^{\circ}\text{C}$ ) related to arctic conditions.
- From the compression testing of the pillars, the recorded load-deformation relationships shall be used for further analyzing to get a detailed understanding of the deformation mechanisms.

Three weeks after start of the thesis work, an A3 sheet illustrating the work is to be handed in. A template for this presentation is available on the IPM's web site under the menu "Masteroppgave"

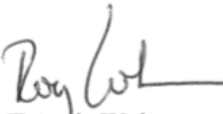
(<http://www.ntnu.no/ipm/masteroppgave>). This sheet should be updated one week before the Master's thesis is submitted.


Performing a risk assessment of the planned work is obligatory. Known main activities must be risk assessed before they start, and the form must be handed in within 3 weeks of receiving the problem text. The form must be signed by your supervisor. All projects are to be assessed, even theoretical and virtual. Risk assessment is a running activity, and must be carried out before starting any activity that might lead to injury to humans or damage to materials/equipment or the external environment. Copies of signed risk assessments should also be included as an appendix of the finished project report.

The thesis should include the signed problem text, and be written as a research report with summary both in English and Norwegian, conclusion, literature references, table of contents, etc. During preparation of the text, the candidate should make efforts to create a well arranged and well written report. To ease the evaluation of the thesis, it is important to cross-reference text, tables and figures. For evaluation of the work a thorough discussion of results is appreciated.

The thesis shall be submitted electronically via DAIM, NTNU's system for Digital Archiving and Submission of Master's thesis.

The contact person is

  
Torgeir Welo  
Head of Division

  
Christian Thaulow  
Professor/Supervisor

 NTNU  
Norges teknisk-  
naturvitenskapelige universitet  
Institutt for produktutvikling  
og materialer

## Preface

This thesis is written as a requirement to obtain the degree of Master of Science and Technology at the Norwegian University of Science and Technology (NTNU). The Master thesis serve as a documentation of the specialization done within the nanomechanical testing field, and performed at the Department of Engineering Design and Materials, where my supervisor has been Prof. Dr. Christian Thaulow.

Extensive work has been put into designing and developing a cooling system interfaced with a picoindenter and SEM, in order to cool down the sample before in-situ compression testing of Focused Ion Beam (FIB) fabricated pillars. The designing and construction of the cooling system, proved to be challenging and a significantly time consuming part of this investigation. Due to the sensitivity of the picoindenter and the limited size inside the SEM chamber, several factors were important to consider. The development of new testing equipment involved series of trial and error before a successful solution was obtained. Several discussions and considerations with professionals within different fields were crucial to obtain reliable solutions. Some components were ordered externally which resulted in some delays due to shipping problems. A series of components had to be fabricated by different finemechanical workshops at NTNU. By this, progress in the experimental work was dependent of external personnel. During the time of this project, some downtime of Focused Ion Beam at the NanoLab (NTNU) delayed some of the experimental work related to pillar production, hence the intension of producing pillars within several grain orientations was prevented.

I had the pleasure of attending the Nanomechanical workshop “Nanobrücken” in Saarbrücken in the period 23<sup>th</sup>-23<sup>th</sup> mars. This was a great opportunity to consult my work with expertise within the field of nanomechanical testing. At the conference my work was presented with a poster, which is included in Appendix G.

Performing a risk assessment of the planned worked in the Master thesis, was obligatory and is presented in Appendix G. Additionally, the project were presented on a poster at the department, in the beginning and at the end of the work, where both posters are included in Appendix F.

## Abstract

Applications of nanomechanical testing methods have become increasingly important in all fields of material research. There is a significant interest in obtaining information about material features at small scales, in order to get a detailed characterization of the materials deformation behavior. To meet the needs, various experimental techniques have been developed to explore mechanical properties at micro-and nanoscale. So far, most small-scale mechanical testing methods have been done at room temperature, since it does not require the special modification of equipment. However, engineering materials are often used at temperatures other than room temperature. The oil and gas industry in the arctic areas are on increase and exploration of these fields require high strength materials capable of significantly reducing the probability of failure in the critical extreme environments. Iron alloys along with other metals are by far the most common metals used in the industry due to their great range of desirable properties.

In view of the long-standing contradictory statements on the deformation of bcc single crystals and their macroscopic slip planes, recent insights and developments are reported in this thesis. The literatures reveals that the flow stress of Fe have a pronounced dependence of crystal orientation and temperature, mostly due to non-planar spreading of  $a/2\langle 111 \rangle$  type dislocation cores [1]. They exhibit complex slip modes during deformation and show a severe glide direction sensitivity due to the dislocation core structure. Recently conducted experiments on pure Fe micropillars, shows that slip is activated on both  $\{110\}$  and  $\{112\}$  planes at room temperature. Additionally, slip systems with lower stressed planes are sometimes preferable. However, experimental confrontations of the slip behavior of pure Fe at low temperatures are generally missing in the literature.

In the present investigation, attention is focused on constructing and developing a nanomechanical cooling system to study slip behavior of bcc  $\alpha$ -Fe at low temperatures. The experimental work included in-situ uniaxial compression tests of Focused Ion Beam (FIB) fabricated pillars with a diameter of  $1\mu\text{m}$ , in the single slip orientations  $\langle 235 \rangle$  and  $\langle 149 \rangle$ . Characterization of the crystallographic orientations was done by Electron Backscatter Diffraction (EBSD) analysis, where grains of interest were highlighted. The testing was conducted inside of a Scanning Electron Microscope (SEM) equipped with a PI85 PicoIndenter provided by Hysitron, and the constructed cooling system.

From the experimental and analytical work it is concluded that the constructed cooling system has the capability to reduce the sample temperature down to  $-90^\circ\text{C}$ , whereas the simultaneous cooling of the sample ensure reliable mechanical tests. From the in-situ compression tests at low temperatures, it is seen from slip trace analysis that slip is activated in both  $\{110\}$  and  $\{112\}$  planes, where slip systems with lower Schmid factors are more preferable than the ones with higher stresses, for  $\langle 235 \rangle$  oriented pillars. Furthermore, it is observed an increased strength with decreasing temperature, by comparing the present results with Rogne and Thallow's work [2], where Fe pillars of same size were tested at room temperature. The temperature dependency is more prominent for  $\langle 235 \rangle$  oriented pillars, than for  $\langle 149 \rangle$  oriented pillars.  $\langle 235 \rangle$  oriented pillars exhibits 39.8% higher stress at 2.5% strain at  $-90^\circ\text{C}$ , than  $\langle 235 \rangle$  oriented pillars obtain at room temperature (1070MPa vs. 644MPa). For  $\langle 149 \rangle$  oriented pillars a 10.3% higher stress is obtained at  $-90^\circ\text{C}$ , than  $\langle 149 \rangle$  oriented pillars obtain at room temperature (710 vs. 637MPa). It is assumed that the subsequent deformation mechanisms are affected of the relative microstructural features of the bcc structure for the different grain orientations. Additionally, activation of secondary slip systems could be a

result of the breakdown of Schmid`s law as well as small misalignments between indenter tip and pillar top-surface.

## Sammendrag

Anvendelser av nanomekaniske testmetoder har stadig blitt viktigere i alle felt innen materialforskning. Det er av høy interesse å få en bedre forståelse om materialenes funksjoner på en mindre skala, for å få en detaljert karakterisering av materialenes deformasjonsoppførsel. For å møte disse behov, har ulike eksperimentelle teknikker blitt utviklet med hensikt å utforske materialers mekaniske egenskaper på mikro- og nanonivå. Frem til nå har de fleste mekaniske testmetodene på mikro skala blitt gjennomført ved romtemperatur, siden det ikke krever noen spesiell modifikasjon av utstyr. Likevel, konstruksjonsmaterialer er ofte benyttet ved andre temperaturer enn romtemperatur. Olje-og gassindustrien i arktiske strøk er i vekst og utforskning av disse områdene krever materialer med høy styrke, som betydelig kan redusere sannsynligheten for materialsvikt under de ekstreme forholdene. Jernlegeringer sammen med andre metaller, er de mest vanlige metaller som brukes i industrien på grunn av et stort spekter av gode materialegenskaper.

Det har over lang tid vært motstridende uttalelser om deformasjonsmekanismene til bcc enkrystaller og deres makroskopiske glidesystemer. Noen nylige innsikter og utviklinger er presentert i denne rapporten. Det er i litteraturen påstått at spennings-og tøyningkurvene til jern har en fremtredende avhengighet av krystallorientering og temperatur, som et resultat av den ikke-planare spredningen av  $a/2\langle 111 \rangle$  skru dislokasjoner i bcc strukturen. Bcc metaller opplever komplekse glidefunksjoner ved deformasjon og viser en sterk glideretning avhengighet, som skyldes den komplekse strukturen til krystallet. Nylig forskning på mikropillarar av renjern, viser at glidning, kan skje i både  $\{110\}$ -og  $\{112\}$  plan ved romtemperatur. I tillegg så har det blitt observert at aktiviserte glidesystemer ikke alltid er det systemet med høyest spenning. Eksperimentelt arbeid som omfatter analysering av aktiviserte glidesystemer til ren jern, er midlertidig bare utført ved romtemperatur. Det er generelt lite informasjon i litteraturen som omfatter aktivisering av glidesystemer ved forskjellige krystallorienteringer i jern ved lave temperaturer.

I det foreliggende arbeidet, har fokuset vært å utvikle og konstruere et nanomekanisk kjølesystem, for å studere glidemekanismene til bcc  $\alpha$ -Fe ved lave temperaturer. Det eksperimentelle arbeidet inkluderer in-situ kompresjonstesting av Focused Ion Beam (FIB) maskinerte pillarer med en diameter på  $1\mu\text{m}$ , i kornorienteringene  $\langle 235 \rangle$  og  $\langle 149 \rangle$ . Karakterisering av de krystallografiske orienteringene ble gjennomført ved hjelp av Electron Backscatter Diffraction (EBSD) analyser, der de refererte kornorienteringene ble fremhevet og lokalisert på prøven. Selve kompresjonstesting ble gjennomført i en Scanning Electron Microscope (SEM), supplert med en PI85 PicoIndenter fra Hysitron og det konstruerte kjølesystemet.

Fra det eksperimentelle og analytiske arbeid, er det konkludert med at det konstruerte kjølesystemet har evnen til å redusere prøve temperaturen ned til  $-90^\circ\text{C}$ , samt gjennomføre pålitelig mekanisk testing. Fra in-situ kompresjonstesting, ved lave temperaturer, er det sett fra "slip trace" analysen at slip er aktivert i både  $\{110\}$  og  $\{112\}$  plan, hvor glidesystemer med lavere Schmid faktorer i  $\langle 235 \rangle$  orienterte pillarer, dominerer deformasjonen. I tillegg er det observert økt styrke med synkende temperatur, ved å sammenligne de foreliggende resultater med Rogne og Thallow 's arbeid [2], hvor jerpillarar av samme størrelsesorden, ble testet ved romtemperatur. Temperaturavhengigheten er mer fremtredende for  $\langle 235 \rangle$  orienterte pillarer, enn for de  $\langle 149 \rangle$  orienterte pillarene.  $\langle 235 \rangle$  orienterte pillarer viser 39,8% høyere styrke ved 2,5% tøyning ved  $-90^\circ\text{C}$ , enn hva  $\langle 235 \rangle$  orienterte pillarer viste ved romtemperatur (1070MPa vs. 644MPa). For  $\langle 149 \rangle$  orienterte pillarer, ble 10,3% høyere



styrke oppnådd ved  $-90^{\circ}\text{C}$ , enn hva  $\langle 149 \rangle$  orienterte pillarer oppnådde ved romtemperatur (710 vs 637MPa). Det antas at de etterfølgende deformasjonsmekanismene er preget bcc krystallets komplekse struktur, for de ulike kornorienteringene. I tillegg fører aktivering av sekundære glidesystemer kan være et resultat av de omdiskuterte motstridelser av Schmid 's lov. Det er også tatt i betraktning at unøyaktig plassering av indenteren i forhold til pillaroverflaten, kan ha påvirket deformasjonen i en liten grad.

# Content

Problem text.....	i
Preface .....	iii
Abstract .....	iv
Sammendrag .....	vi
Content .....	viii
<b>1. Introduction .....</b>	<b>1</b>
<b>2. Theoretical background.....</b>	<b>4</b>
<b>2.1. Material deformation, properties and defects.....</b>	<b>4</b>
2.1.1. Crystal plasticity .....	4
2.1.2. Material defects in bcc crystals .....	5
2.1.3. Slip mechanisms in bcc .....	8
2.1.4. Slip activation - Critical Resolved Shear Stress .....	10
2.1.5. Peierls stress .....	11
2.1.6. Low temperature slip mechanisms of bcc .....	13
<b>2.2. Nanomechanical testing.....</b>	<b>18</b>
2.2.1. Nanoindentation .....	18
2.2.2. Pillar compression testing.....	20
2.2.3. Determining mechanical properties.....	22
<b>2.3. Slip mechanisms in bcc pillars.....</b>	<b>23</b>
2.3.1. Slip system analysis.....	24
2.3.2. Low temperature deformation of bcc pillars .....	30
<b>3. Experimental procedure .....</b>	<b>33</b>
<b>3.1. Sample preparation for General Metallographic, EBSD- and FIB- Analysis.....</b>	<b>33</b>
3.1.1. Sample .....	33
3.1.2. Grinding.....	33
3.1.3. Electropolishing.....	33
<b>3.2. Microindentation .....</b>	<b>34</b>
<b>3.3. EBSD analysis .....</b>	<b>34</b>
3.3.1. Surface Scan .....	34
3.3.2. Crystal Orientation Mapping.....	35
<b>3.4. Cooling system set-up .....</b>	<b>36</b>
<b>3.5. Pillar fabrication .....</b>	<b>43</b>
<b>3.6. In-situ pillar compression .....</b>	<b>46</b>
<b>3.7. Slip trace analysis.....</b>	<b>47</b>
<b>4. Results and discussion.....</b>	<b>48</b>
<b>4.1. Pillar Fabrication .....</b>	<b>48</b>
<b>4.2. Drift analysis .....</b>	<b>49</b>
<b>4.3. Nanocompression in-situ .....</b>	<b>52</b>
<b>4.4. Crystallographic slip.....</b>	<b>56</b>
<b>4.5. Mechanical behavior and the influence on flow curves.....</b>	<b>60</b>
<b>5. Conclusion.....</b>	<b>64</b>
<b>6. Further work .....</b>	<b>65</b>
<b>7. Acknowledgements.....</b>	<b>66</b>

<b>Bibliography .....</b>	<b>67</b>
<b>Appendix A: Pillar dimensions .....</b>	<b>71</b>
<b>Appendix B: Load-displacement curves .....</b>	<b>72</b>
<b>Appendix C: Pillars post compression .....</b>	<b>76</b>
<b>Appendix D: Stress-strain .....</b>	<b>79</b>
<b>Appendix E: Thermal drift data .....</b>	<b>83</b>
<b>Appendix F: Master thesis Posters .....</b>	<b>88</b>
<b>Appendix G: Poster submitted to Nanobrücken workshop .....</b>	<b>89</b>
<b>Appendix H: Risk evaluation .....</b>	<b>90</b>

# 1. Introduction

The activity in the Arctic areas is on the increase. 25 % of the worlds undiscovered oil and natural gas are believed to be located in the northern area. The exploration of these areas requires high quality materials today due to the harsh climate conditions and low temperatures down to  $-60^{\circ}\text{C}$ . Materials in an arctic environment meet a large number of challenges. Wind, sea waves, drifting icebergs and icing of constructions are some of the challenges that can result in high construction loads, illustratively shown in Figure 1. In combination with the extreme low temperatures this gives the toughest requirements to mechanical performance, fracture resistance and lifetime integrity. Arctic areas are highly vulnerable and even small accidents can easily lead to greater ecological problems than in warmer climates. Understanding material deformation mechanisms under these environmental conditions can help prevent dangerous failure from occurring and allow for the development of both strong and cost-efficient materials. [3-7].

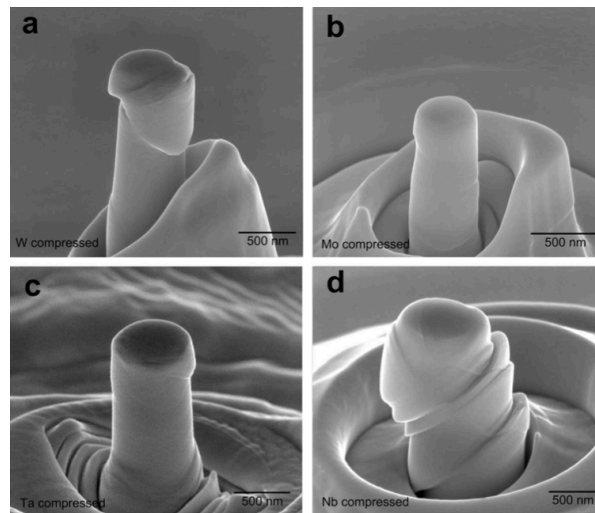


Figure 1: Illustration photo of an arctic environment [8].

Technological development has made it possible to get a better fundamentally understanding of the mechanisms behind material deformation. Today's scientific and engineering research is undoubtedly in the realm of nanotechnology. Imaging, manipulation, fabrication and application of systems at micro- and nanometerscale have opened up for new insight into the local material properties. To maintain the progress of current research and industrial progress, the continued development of new state of the art tools for nanotechnology is a clear necessity. In the recent years Focused Ion beam (FIB) instruments have emerged as tools for materials characterization with the ability to conduct material fabrication with precise micro- and nano machining. The technology has become imperative to the progress of materials science and other fields relying on nanotechnology. Among several other multiple analysis methods, there have been an extensively use in fabrication of micro- and nanosized pillars [1, 2, 9-11], due to the relatively simple and cost efficient procedures involved and the ability to extract material properties and deformation mechanisms from a restricted material volume. Compression testing of micropillars has proved to be a valuable method to study the resistance to plastic flow and obtain a better understanding of the underlying dislocation mechanisms as well as slip behavior of the material.

Among the common crystal structures found in metals, body centered cubic (bcc) metals pose different conditions for plasticity compared with the fcc metals, because of the higher Peierls stress and easier cross slip for the slower screw dislocations. The high Peierls potential leads to a reduced mobility of screw dislocations relative to the edge dislocations. In fcc metals, the Peierls potential is relatively small, and thus edge and screw dislocation have similar mobility [12, 13]. Various discussions on the behavior of bcc crystals reveal a number of contractions with respect to slip plane activity. Even though there is no generally accepted explanation to

the deformation behavior of bcc materials, recent studies provides good basis for a fundamentally understanding and further investigations on the deformation behavior of bcc crystals. Seeger [14] suggests that the slip nature of bcc crystals is highly dependent on temperature, upon which dislocations may accommodate either a straight  $\{110\}$  slip or a wavy type of  $\{112\}$  cross slip pattern. Furthermore, at room temperature the  $a/2 \langle 111 \rangle$  type of screw dislocations move on  $\{112\}$  slip planes, which enable cross slip [15]. At low temperatures, the dislocations in bcc are no longer mobile. The particular core structure of the screw dislocations induces some complexity in the slip geometry. This complexity is related to the asymmetry on  $\{112\}$  planes in the bcc materials. The slip resistance in one direction is different from the resistance in the opposite direction, indicated as the twinning/anti-twinning asymmetry. Moreover, due to small edge fractional dislocation components in the screw dislocation core, stress components other than the resolved Schmid stress affect the glide or the Critical Resolved Shear Stress (CRSS) of the material. These effects, are caused by the non-planar spreading of the dislocation cores and it is stated that Schmid's law is not applicable to bcc for these reasons [14, 16].



**Figure 2: SEM micrographs showing compressed nanopillars from the bcc materials (a) tungsten, W, (b) molybdenum, Mo, (c) tantalum, Ta and (d) niobium, Nb [17].**

The experimental aspects of glide mechanisms in bcc materials, in terms of pillar compression have been the objects of several articles [1, 18-20]. Figure 2 shows illustrative SEM images of the mechanisms of slip in bcc pillars. Especially the temperature dependence of the flow stress has been an active research area until the 90s [21, 22]. At present, atomistic computer simulations studying deformation mechanisms of nanopillars are still an active area of research. It has been shown that besides dislocation glide and climb, deformation twinning is an important deformation mechanism for bcc metals [23]. However, atomistic simulations of nanopillars are performed at conditions that are rather different from the experimental world, since the simulations are based on defect free crystals that are deformed at strain rates of  $5 \times 10^7$ .

Recently, there has been conducted compression test on Fe micropillars, where orientation dependence and strengthening mechanisms have been of interest. Additionally, examination of slip traces in pillars, with constant diameter but varying crystallographic orientation, were conducted. The referred investigations, conducted by B.R.S. Rogne and C. Thaulow [2, 24], are soon to be published (submitted to Materials Science and Engineering A) and has been an important source in this thesis, considering his work is comparable to the present work. The study of slip traces after pillar loading have evidenced that loading along  $\langle 149 \rangle$  direction is dominated by a primary slip system. Additionally it is observed from the slip traces that

loading in the directions  $\langle 149 \rangle$ ,  $\langle 235 \rangle$  and  $\langle 011 \rangle$ , were identified to follow the  $\{110\}\langle 111 \rangle$  slip system. Large pillars will include several dislocations on each available plane and consequently the highest stressed plane will determine where the deformation starts. Slip planes of type  $\{110\}$  have earlier been most frequently observed, as well as some activation from  $\{112\}$ . Furthermore, most of such experiments have been conducted at room temperature since it does not require special modification of equipment. However, since material properties play an important role in the design and construction of low-temperature environments, e.g. arctic environments, it is essential to have a thorough knowledge of their behavior at these temperature regimes as well. Development of experimental techniques that reveals mechanical properties on smallscale materials at different temperatures is necessary.

Thus, the purpose of this study is to develop a cooling system interfaced with a SEM in order to be able to study the orientation dependent behavior of the mechanical properties of bcc  $\alpha$ -iron and the slip mechanisms, at lower temperatures. The cooling system based on liquid nitrogen and a cold finger have been designed, produced and connected to the iron sample mounted on a picoindenter, inside the SEM vacuum chamber. Initially, sample preparation for general metallographic-, EBSD- and FIB analysis was performed. Furthermore, electron backscatter diffraction (EBSD) analysis were conducted in order to correlate the effect of crystal lattice orientation to the compression response by investigation of grain orientation and slip systems. Finally, FIB fabricated pillars in the  $\langle 149 \rangle$  and  $\langle 235 \rangle$  oriented grains were compressed with temperatures down to  $\approx -90^\circ\text{C}$ . The obtained stress-strain response from the compression test were analyzed together with the in situ recorded video frames and slip traces on the pillar surface.

## **2. Theoretical background**

The theoretical background in this thesis, are divided into 3 chapters (2.1., 2.2., and 2.3.), which build up a theoretical background necessary to obtain a relevant understanding for the present work. It is appropriate to start the theoretical background by giving an introduction to the general mechanisms behind crystal plasticity, dislocation mechanisms, defects and slip mechanisms related bcc crystals in order to understand the deformation mechanisms of bcc in a proper perspective. The first section further emphasizes the slip mechanisms in bcc metals, where temperature dependence of slip plane activation is also presented. Schmid's law and its violation in bcc crystals is handled in the following chapter, along with its connection to the non-planar spreading of screw dislocation cores. To further increase the knowledge of iron's deformation mechanisms, low temperature properties of iron are also introduced. Chapter 2.2. explains the concept of the nanomechanical testing methods performed in this thesis. It is necessary to obtain an understanding of the concept of pillar compression testing, hence it is given a short introduction to nanoindentation, followed by the principle of pillar compression and analysis methods. Towards the end of the theory i.e. chapter 2.3., the focus turns to connect the crystallographic features and dislocation mechanisms, to the slip mechanisms previously observed in iron pillars at both room temperature and low temperatures. The intrinsic properties, whereby examples are presented and confronted with experimental results.

### **2.1. Material deformation, properties and defects**

This chapter has the purpose to give a brief introduction to the basic principles behind general crystal plasticity in order to give an elementary understanding of material deformation. Followed by an overview of material defects and dislocation mechanisms related to the bcc structure. In order to give an understanding of the slip system activity of bcc crystals and the connection between the core structure and the intrinsic properties. The line properties of dislocations will be introduced, thereby translating much of crystal plasticity into dislocation mechanisms.

#### **2.1.1. Crystal plasticity**

A perfect metallic single crystal, which is characterized by a specific periodic arrangement of atoms, can respond only in a reversible elastic manner in thermal equilibrium with its surroundings when stressed monotonically well below the critical levels that destabilize the crystal structure. Under an applied homogeneous stress, the elastic response is homogeneous down to the atomic level. In contrast, the plastic response is locally heterogeneous and requires crystal defects for its development. The type and intensity of the plastic response depend on the character of the defect state. For this purpose the crystal defects are introduced in a hierarchy of increasing dimensionality from point, through line, to planar defects. Among these defects, the line defects, i.e. dislocations, are regarded as the principal carriers of plastic deformation [25]. Under an applied stress, the atomic lattice deforms elastically until the stretched bonds near a dislocation break down and new bonds are formed. During this process, a part of the crystal gradually slips one interatomic distance with respect to the other part. The dislocations enable sections of the slip plane to shear, depending on the specific arrangement of atoms. The crystallographic slip of dislocations occurs on the most close-packed slip planes in the most close-packed directions, which together form the slip systems.

The stress directly affecting the motion of dislocations is the projected shear stress on the specific slip systems, also referred to as the resolved *Schmid* stress. This phenomenon is based on the process when the resolved shear stress is larger than the resistance on the respective slip system, a glide is activated. Conceptually, all the slip systems are active but the most favorable ones carry most plastic deformation. Each material has specific crystal structures and specific slip systems. The crystallographic structure that is considered in this thesis is the body centered cubic (bcc) crystal.

### 2.1.2. Material defects in bcc crystals

Crystalline materials do always contain some kind of defects, which might influence many of their properties. This includes point defects, planar defects and bulk defects [26]. Point defects (e.g. vacancies, interstitials and impurities) and bulk defects (e.g. voids and precipitates) have not been topics in this thesis, and will not be described further. Instead defects like dislocations and planar defects have a more central part in this work, considering it is relevant for the obtained results in this thesis.

The most important two-dimensional, or line defect is the above mentioned dislocation. The dislocation is responsible for the phenomenon of slip, by which most metals deform plastically. The earliest calculations of the stress required to induce plastic deformation in a crystal containing no dislocation, known as the theoretical strength of the material, were performed by Frenkel in 1926 [27]. The deformation occurs by atomic planes sliding over each other. In a perfect crystal, i.e. in the absence of crystal defects, the sliding of one plane past an adjacent plane would have to be a rigid co-operative movement of all the atoms from one position to another. The atoms are out of position in the crystal structure, which are generated and moved when a stress is applied as illustrated in Figure 3. The shear stress required to move the top row of atoms, across the bottom row is given by the sinusoidal relation:

$$\tau = \frac{Gb}{2\pi a} \sin \frac{2\pi x}{b} \quad (1)$$

where  $\tau$  is the applied shear stress,  $G$  is the shear modulus,  $b$  the spacing between atoms in the direction of the shear stress,  $a$  the spacing of the rows of atoms and  $x$  is the shear translation of the two rows away from the low energy position of stable equilibrium ( $x=0$ ) [28].

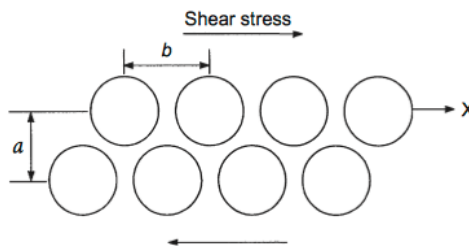


Figure 3: Schematic illustration of atom positions used to estimate the theoretical critical shear stress for slip [28].

The atoms close to the core of the dislocation are displaced from their thermal equilibrium positions and thus have a higher energy. In order to keep the energy as low as possible the dislocation tries to be as short as possible. The energy necessary to generate a dislocation is proportional to the square of burgers vector,  $b^2$ . This means that the most stable (minimum energy) dislocations have the minimum length of  $b$ , and justifies why dislocations mostly



move in close-packed planes in close-packed directions. The burgers vector is the vector that represents the magnitude and direction of the lattice distortion of dislocation in the crystal, and is represented by

$$|b| = \frac{a}{2} \sqrt{h^2 + k^2 + l^2} \quad (2)$$

where  $a$  is the unit cell length of the crystal,  $b$  is the magnitude of burgers vector and  $h$ ,  $k$  and  $l$  are the components of Burgers vector,  $b = \langle hkl \rangle$ . There are generally two basic types of dislocations; edge dislocation and screw dislocation. An edge dislocation can be easily visualized as an extra half-plane of atoms in a lattice. The extra half plane will break its existing bonds and form new bonds with its neighbor, opposite of the dislocation motion. This step is repeated in many steps until the dislocation has moved entirely through the lattice and formed an edge as illustrated in Figure 4 (a). A defining characteristic of an edge dislocation is that its Burgers vector is always perpendicular to the dislocation line. The second basic type of dislocation is called screw dislocation, illustrated in Figure 4 (b), where the burgers vector lies in the direction of the dislocation line. A screw dislocation does not have preferred slip plane, as an edge dislocation has, and therefore the motion of a screw dislocation is less restricted than the motion of an edge dislocation. The dislocation may slip in any plane containing the dislocation, which make it comparatively easy for screw dislocations to change glide planes. This phenomenon is called cross-slip, and are schematically illustrated in Figure 5 [29].

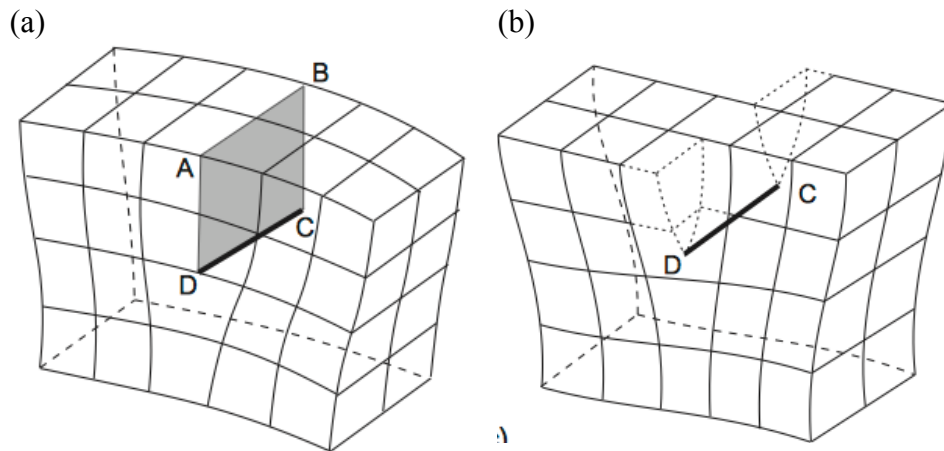


Figure 4: A simple cubic lattice with (a) an edge dislocation  $DC$  formed by inserting an extra half-plane of atoms in  $ABCD$  and (b) a screw dislocation  $DC$  formed by displacing the faces  $ABCD$  relative to each other in the direction,  $AB$  [28].

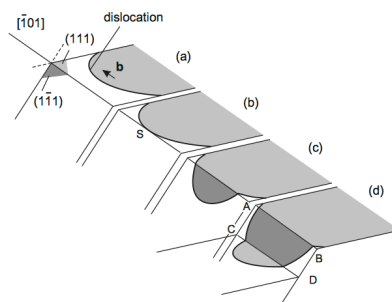
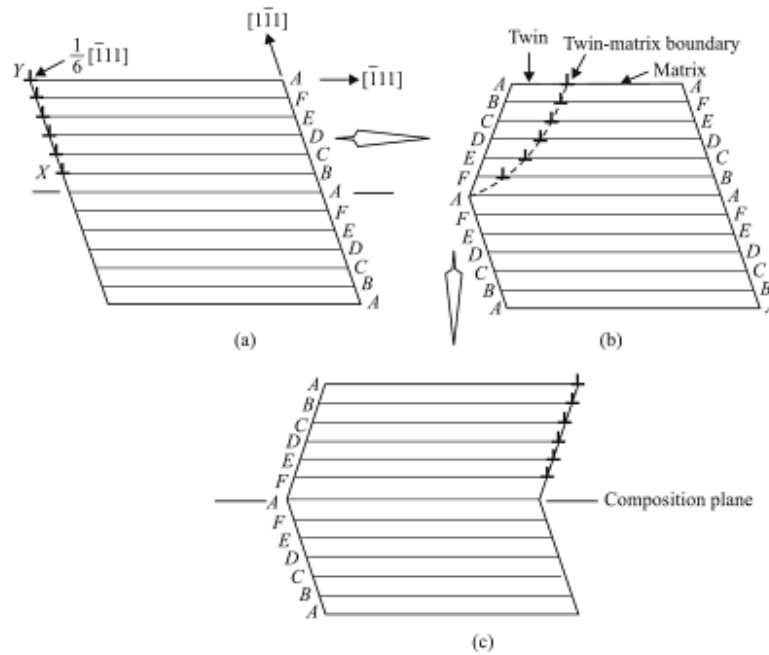


Figure 5: Illustration of the phenomena cross slip, where a screw dislocation move from one slip plane to another [30].

The dislocation motion is particularly complicated in bcc materials, due to the likelihood of cross-slip. Since the preferred slip planes share the same  $\langle 111 \rangle$  direction, it makes it easy for the screw dislocations to move in a haphazard way on different  $\{110\}$  planes or combinations of  $\{110\}$  and  $\{112\}$  planes, favored by the applied stress. For this reason slip lines can often be wavy and ill-defined. Both edge and screw dislocations are important for plasticity in bcc metals and many particular aspects of the deformation characteristics in bcc metals are ascribed to the 3-dimensional core structure of the screw dislocation, which is consequently anchored in the lattice [1]. The literature states that at low and moderate temperatures screw dislocations move much slower than edge dislocations. Additionally, recent work by Caillard [15, 31] on pure iron at temperatures between 100 and 300K shows that screw dislocations move on  $\{110\}$  planes. His findings also indicate that edge dislocations can glide either on  $\{110\}$  or  $\{112\}$  planes. However, dislocation sources, which require the motion of screw dislocations, always move on  $\{110\}$  planes.

Bcc metals show an asymmetry in the core structure, which result in different slip resistance in different slip directions, indicated as the twinning/ antitwinning asymmetry. The planar defect twinning is another important mode of strain energy relaxation in metals, and competes with dislocation slip to be the dominant carrier of plasticity. The competition between deformation twinning and full slip depends on the orientation and magnitude of applied stress, as well as temperature, defects and intrinsic material properties [32].

Twinning becomes a more dominant mode of plastic deformation as the temperature is decreased and at high strain rates of deformation [33]. It is a process where a region of a lattice locally changes orientation, mirrored over a twin plane, due to shear strain. The unique feature of twinning is that the reorientation between the twinned region and the matrix occurs in an abrupt manner while the lattice reorientation in deformation due to slip is gradual. However, twinning, like slip, must occur through the movement of dislocations. The Burgers vector of these dislocations must have the magnitude and direction of the shear between successive planes. In all bcc metals, the twinning shear is  $1/\sqrt{2}=0,707$  along the direction  $\langle 111 \rangle$  on a  $\{112\}$  plane. A coherent twin can be produced by a uniform shear of  $1/6 \langle 111 \rangle$  on successive  $\{112\}$  planes, which can occur by a layer by layer motion of a partial dislocation with Burgers vector  $1/6 \langle 111 \rangle$ , as illustrated in Figure 6. As a set of twinning dislocations X-Y moves into the crystal, the volume swept becomes twinned. Figure 6 (c) shows a completely twinned crystal with all the twinning dislocations having swept through the entire crystal [26]. There is an equivalence of high strain rates and low temperatures in twinning. An explanation for this is that an enclosed lenticular twin must always have some accommodating slip near its edge due to the high stress concentration near the edge. The applied stress necessary to start the twin will increase when the slip activity near the edge increases. Dislocation glide is thermally activated, hence at low temperatures accommodating slip activity is low, resulting in a lower stress needed to propagate the twin. A fully understanding why twin can propagate much more rapidly than a slip band at high strain rate is not yet established. However, it appears that dislocations related to twin growth are more mobile than dislocations related to slip [34].



**Figure 6: Twinning in bcc lattice (a) section parallel to  $(110)$  showing stacking sequence of  $\{112\}$  planes, where plane  $A$  in the middle of the sequence is the twinning plane.  $X$ - $Y$  illustrates a row of twinning partials, where it is one dislocation in each plane after plane  $A$ . (b) the dislocations have partially moved into the crystal and starts to produce a twinned region. The stacking order within the region has now changed. (c) A twinned crystal [26].**

### 2.1.3. Slip mechanisms in bcc

Metals and many types of non-metallic solids are crystalline, i.e. the atoms are arranged in a pattern that repeats itself periodically in three dimensions. The body centered cubic structure is one of the most common crystallographic structures, where the atoms are situated at the corners of the unit cell and at the center site as shown in Figure 7.

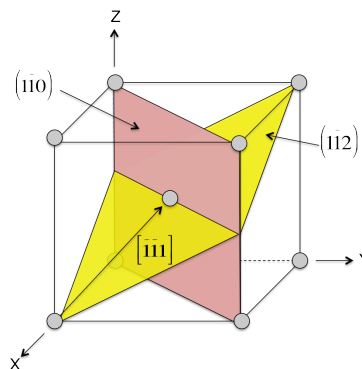


**Figure 7: Unit cell of body-centered cubic structure with the possible slip planes  $(1-10)$  and  $(1-12)$ , adapted from [35].**

There have been several contradicting statements on the active slip planes of bcc metals. The different concepts will not be discussed here in detail, however a summary including the current developments will be presented in the following paragraphs.

The first attempt goes back to the introduction of the pencil glide mechanisms by Taylor and Elam (1926), where slip was assumed to be oriented in the  $\langle 111 \rangle$  crystallographic direction, while the mean plane of slip was the one having the maximal projected shear stress. This plane might be crystallographic, but can also be a non-crystallographic plane. It was early stated by Gough (1928) and Barrett et al. (1937) that the  $\{110\}$ ,  $\{112\}$  and  $\{123\}$  families

contain the crystallographic slip planes during deformation of bcc metals, which is still stated in investigations of bcc metals. Another frequently used view is the participation of {110} and {112} slip planes only, whereby it is assumed that {123} planes requires a higher temperature for activation. Chen and Maddin (1954) stated that only the {110} slip planes are active at room temperature, based on the argument that apparent slip on both {112} and {123} planes is actually composed of slip on two non-parallel {110} planes. It is believed that the activation energies for slip on {123} and {112} planes are not exactly identical to that of {110}, but sufficiently close to allow slip on these planes under certain conditions. Thus, bcc slip systems require additional energy (in form of temperature dependence) in order to function. The planes in bcc with the highest atomic packing density are the (110) planes. These are known as primary slip planes, while the second set of planes upon which slip may occur, are termed secondary slip planes. Van der Walt considered slip activation in bcc crystals and claims, that (123) planes are rarely or never involved in slip, thus having no real secondary slip system [29, 36].

In bcc structures, deformation and the choice of slip systems are more complicated than in fcc structures, since three planes may be active, but the directions are always  $\langle 111 \rangle$ , which is the only closed packed direction in the bcc structure. Bcc  $\alpha$ -Fe can contain up to 48 slip systems, as indicated in Table 1. Usually in all the systems, slip occurs in the shortest direction, however, unlike fcc structures, there are no truly close-packed planes in bcc crystal structure. Vitek [37] studied the intrinsic properties observed in bcc metals, where it is suggested that the different deformation behavior observed in bcc compared to fcc metals, are related to the core structure of screw dislocations. It is also highly discussed that the slip system activation in bcc metals is highly dependent on crystal orientation and especially on the temperature. The temperature dependence for slip activation in bcc metals will be discussed further in section 2.1.6..

Slip in iron single crystals has been studied extensively[1], and as in studies of the other bcc metals, slip trace analysis shows that identifying slip planes is quite complex. Spitzig and Keh [38] provided an informative summary of the work performed before 1970, whereas in all of those investigations, the observed slip planes shows a wide range of possibilities, including {110}, {112}, {123} and general non-crystallographic orientations. However, specific comparisons are a challenge since the observations are complicated by issues of purity, loading condition, temperature, strain rate and crystallographic orientation. Additionally, crystal defects can play a significantly role on the materials properties.

**Table 1: Slip planes in bcc metals. Data obtained from [29].**

Lattice type	Slip planes	Slip directions	Number of slip planes	Number of slip directions per plane	Slip systems
bcc	{110}	$\langle 111 \rangle$	6	2	12
	{112}	$\langle 111 \rangle$	12	1	12
	{123}	$\langle 111 \rangle$	24	1	24

### 2.1.4. Slip activation - Critical Resolved Shear Stress

Schmid and co-workers (e.g. Schmid and Boas (1935)) first recognized that the yield stress of a metal crystal is strongly depending on the crystal orientation with respect to the loading direction. Yield on the slip plane of a crystallographic family occurs at a constant projected shear stress, termed critical resolved shear stress (CRSS), which is used to quantify how susceptible any given slip system is to activate. The resulting Schmid's law rationalizes the fact that different tensile loads are required to produce slip of different orientation. Slip movement begins when the shearing stress on the slip plane reach a certain threshold value of stress, the critical resolved shear stress, depending on composition and temperature.

To calculate the critical resolved shear stress, it is necessary to know the orientation with respect to the tensile axis of the plane on which slip first appears and the slip direction. This can be easily visualized in Figure 8: Resolved shear stress,  $\tau_R$  produced on a slip system, adapted from [30]., where we consider a cylindrical single crystal with cross section  $A$ . The angle between the normal to the slip plane and the tensile axis is  $\Phi$ , and the angle that the slip direction makes with the tensile axis, is  $\lambda$ . The area of the slip plane inclined at the angle  $\Phi$  will be  $A/\cos \Phi$ , and the component of the axial load acting in the slip plane in the slip direction is  $P \cos \lambda$ . Hence, Schmid's law is given by:

$$\tau_R = \frac{P \cos \lambda}{A / \cos \phi} = \frac{P}{A} \cos \phi \cos \lambda \quad (3)$$

Equation (3) gives the shear stress resolved on the slip plane in the slip direction. This shear stress is a maximum when  $\Phi = \lambda = 45^\circ$ , so that  $\tau_R = \frac{1}{2} P/A$ . If the tension is normal ( $\lambda = 90^\circ$ ) or parallel ( $\Phi = 90^\circ$ ) to the slip plane, the resolved shear stress is zero and slip will not occur for these orientations since there is no shear stress on the slip plane. Crystals close to these orientations tend to fracture rather than slip [29].

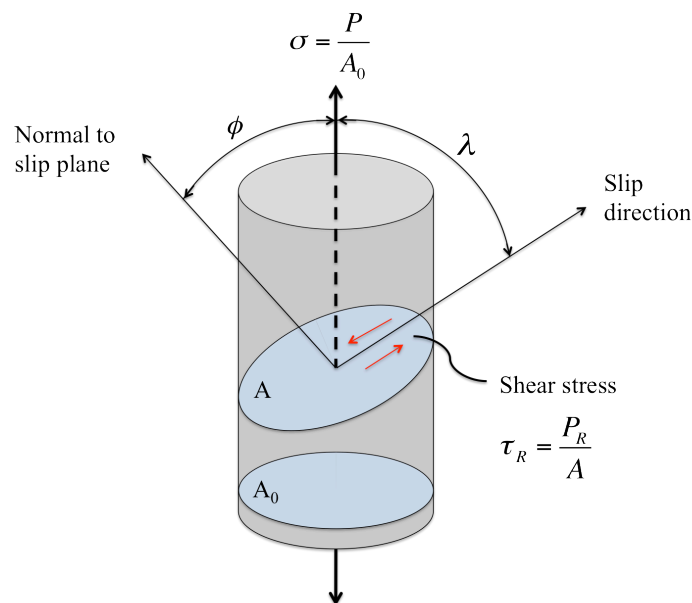


Figure 8: Resolved shear stress,  $\tau_R$  produced on a slip system, adapted from [30].

The geometrical factor

$$m = \cos\lambda\cos\phi \quad (4)$$

that relates the applied stress to the resolved shear stress on the slip plane is referred to as the Schmid factor,  $m$ , which is the maximum value of the term for all possible slip planes. The maximum Schmid factor will indicate the operational slip system(s) [29].

Schmid's law has generally been used for both fcc and bcc materials. However, several studies have stated that Schmid's law is not applicable to bcc metals as a result of their plastic anisotropy [16, 39]. The departures from the Schmid's law were early found by Taylor and Elam (1923) on Fe. These departures were of several different types and involved complexities that varied with temperature. Moreover, Hirsch (1960) and Duesbery and Vitek (1998) suggested that the presence of a variety of anomalous slip behavior in bcc metals resulted from a tension-compression asymmetry observed in uniaxial test of single crystals. This asymmetry is attributed to the twinning-antitwining asymmetry of shearing in the slip direction  $\langle 111 \rangle$  along  $\{112\}$  planes. The source of this asymmetry is related to the unique threefold symmetry in the structure of the cores of screw dislocations, which constrains the core and its properties to create symmetry of the lattice [16].

Duesbery and Vitek (1998) suggested that the effect of stress components other than the shear stress in the slip direction might be another important non-Schmid effect originating from the non-planar spreading of  $a/2\langle 111 \rangle$  type screw dislocation cores [25]. Vitek showed that these shear stresses can significantly elevate or reduce the critical resolved shear stress in the direction of the burgers vector needed for the dislocation motion, i.e. the Peierls stress. This occurs owing to the changes of the core induced by these stresses. This effect may be the reason why slip systems with smaller Schmid factors may be preferred over that with the largest Schmid factor.

A series of studies (found from [25]), starting with Vitek et al. (1970) and by other since (e.g. kuramoto et al. 1974), have been of great value because they go a long way toward explaining most of the anomalous selection of slip systems and the sensitivity of the stress required to move the dislocation components of the stress tensor other than resolved shear stress on the slip system, that is, stress components normal to the Burgers vector. These theories serve to demonstrate the complex nature of the screw dislocation core in bcc metals, which produces a variety of anomalies not present in other metals like, fcc, leading to the breakdown of Schmid law. These special characteristics of the cores of screw dislocations and their possible role in explaining the departures from the Schmid law and related anomalies require a more detailed study of the characteristics of screw dislocation cores to obtain a fully understanding.

### 2.1.5. Peierls stress

Dislocation mobility is a fundamental material property that controls strength and ductility of crystals. As mentioned above, the plastic flow of all bcc metals is characterized by the low mobility of  $a/2\langle 111 \rangle$  screw dislocations. The reason, now well established, is that their core is not planar but spreads spatially which leads to a high lattice friction, also referred to as the Peierls stress.

The concept of Peierl's stress is considered to control the low temperature deformation of bcc metals. It is defined as the minimal stress necessary to move a dislocation at zero temperature and can be visualized as a lattice friction [40]. The original model derives from Peierl's and Nabarro [41] who derived the lattice friction stress as an exponential function of the "width of the dislocation" and the Burgers vector. Wider dislocations have a lower Peierl's stress, and different slip systems have different values of Peierl's stress. Peierl's stress is a sensitive function of the structure of the core. This core is determined by the bonding in the crystal and the crystal structure. When the core is planar, i.e. lies on the slip plane, the Peierl's stress can be described by an exponential function. When the core is non-planar, atomistic calculations are required to calculate the Peierl's stress. To understand the origin of the Peierl's stress, one can consider a dislocation as is in a local metastable equilibrium, and stress has to be applied to "pull" the dislocation out of the equilibrium, and into the next position, illustrated in Figure 9. Peierl's stress decreases with increasing distance between atomic planes. Since the distance between planes increases with planar atomic density, slip of the dislocation is preferred on closely packed planes [29].

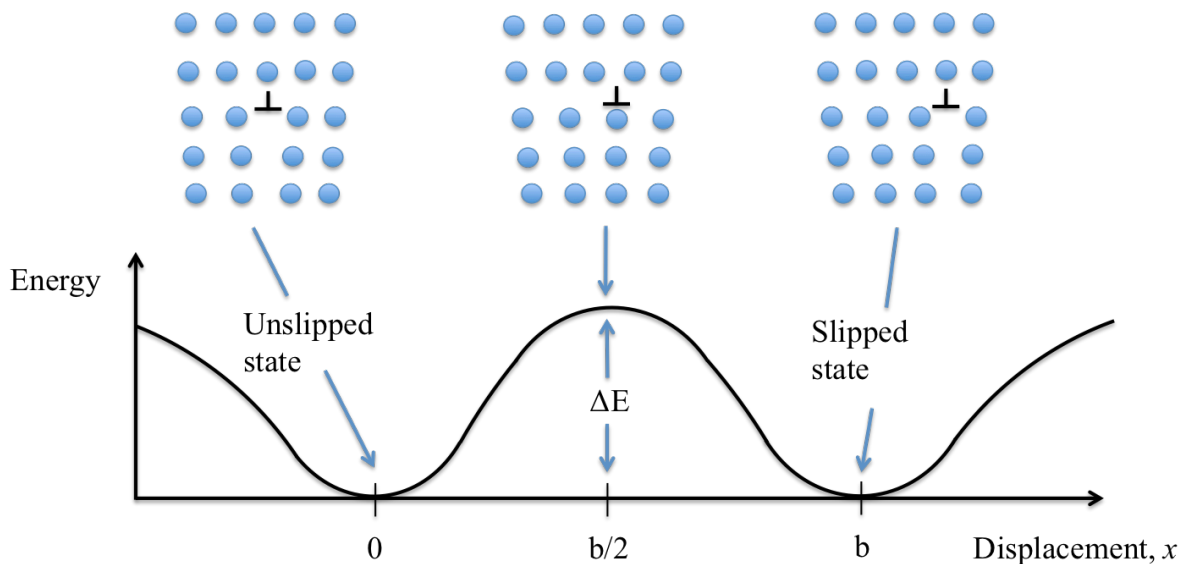


**Figure 9: The concept of Peierls energy barrier, showing a dislocation pass through a higher energy configuration in order to move. Figure adapted from [29].**

It was early established that the strong temperature dependence of the yield stress of high purity bcc metals is associated with the intrinsic nature of the crystal, namely, the core structure of a screw dislocation. The core structure and its role in the thermally activated motion of screw dislocation have been related to the Peierl's stress, and are now part of all models of low temperature plasticity. They are well described by the so-called Peierl's periodic potential, in which screw dislocations move either by nucleation and propagation of kinks or by other closely related mechanisms [15, 21, 42]. Low temperature kinetics is a major difficulty in the physics of dislocations and plastic deformation of bcc metals [42]. The complexity of the observed plastic properties is not completely understood yet. For instance, the kinetics effects associated with the existence of long screw segments in the dislocation microstructure and the different mobility between different dislocations are poorly explained [43].

### 2.1.6. Low temperature slip mechanisms of bcc

Until now it has been mentioned in the theory, that body centered cubic (bcc) metals pose different deformation conditions as a result of their intrinsic properties, compared to other structures such as fcc. The most significant differences between these structures, emerged when experiments were extended to lower temperatures and to high purity materials. The attention in the following paragraphs will only focus on the bcc behavior at lower temperatures.

Low temperature deformation in bcc crystals has specific characteristics such as large sensitivity to strain rate and temperature, a strong difference in dislocation mobility between screw and other dislocation characters and a length dependence of the mobility of screw dislocation segments [43]. Slip system activation in bcc is highly dependent of crystal orientation and especially on the temperature. By deformation, the glide motion of dislocations obeys several fundamental properties of the crystal structure. This is because of lattice periodicity, where the dislocations parallel to dense directions are subjected to periodic variations of core configuration and corresponding core energy. Additionally, as a result of the rotational symmetry around the  $\langle 111 \rangle$  densest direction of slip, the glide resistance is the highest for screw dislocations [42]. The screw dislocations move slower than dislocations of other characters. Hence, the mobility of screw dislocations is therefore expected to control the plastic flow in iron [1, 44].

Seeger (2001) [14], showed in his work that bcc metals show different features and different slip mechanisms in different temperatures ranges. Hence, the physical response below the so-called knee temperature, also called critical temperature,  $T_c$  (typically of the order of magnitude of 0,2 of the melting temperature,  $T_m$ ) and above the knee temperature is different. Below the knee temperature the slip is governed by the glide of  $a/2\langle 111 \rangle$  type screw dislocations in kink pairs as the mobility of screw dislocations is lower than the mobility of edge dislocations. In this temperature range, the flow stress (the stress to maintain plastic deformation after yield) of the metal is highly temperature and strain rate dependent. Above the knee temperature, the flow stress decreases considerably due to self diffusion and recovery processes. Here, the temperature is high enough to wipe out the difference in mobility between screw and non-screw dislocations.

The flow stress dependence on the temperature and the slip mechanism is visualized in Figure 10, where the present numerical values refer to work presented by Caillard [15]. At the absolute zero temperature there are no thermal vibrations of the crystal atoms and the energy needed for plastic flow is obtained by applied stress. The flow shear stress necessary for plastic deformation to occur at absolute zero degrees, is the Peierls shear stress,  $\tau_p$ . At the critical temperature,  $T_c$ , the thermal vibrations are alone adequate to overcome the small range dislocation barriers. At this point the flow stress is strain rate dependent and almost temperature dependent. The thermal region, in between the absolute zero temperature and  $T_c$ , is often divided into three sub-regions, as illustrated in Figure 10, in which it is expected different plastic mechanisms governing the different regions. Brunner and Diehl [45] termed these regions as *Regime I*, *Regime II* and *Regime III*. The transition between the regions is often referred to as the lower bend temperature,  $\hat{T}$ , and the upper bend,  $\hat{T}$  temperature, (in the older literature often called “the hump”). The upper bend temperature observed at  $\hat{T}$  is only found at sufficiently pure samples, and it is emphasized that the occurrence of the upper bend is not the result of a change in slip mechanism but an intrinsic feature of the kink-pair mechanisms.



Below the lower limit (about 100K for  $\alpha$ -Fe), the dislocation glide is confined to the  $\{110\}$  planes. Screw dislocation glide produces straight step patterns. In this temperature range, dislocations are stated to be in their ground state. They show a threefold symmetry and they are able to slip on any of the three  $\{110\}$  planes. Above the upper bend (about 250K for  $\alpha$ -Fe), the dislocation core configurations undergo a transition from their low temperature configurations, to their high temperature configurations, i.e. from slipping in  $\{110\}$  planes to slipping in  $\{112\}$  planes [14].

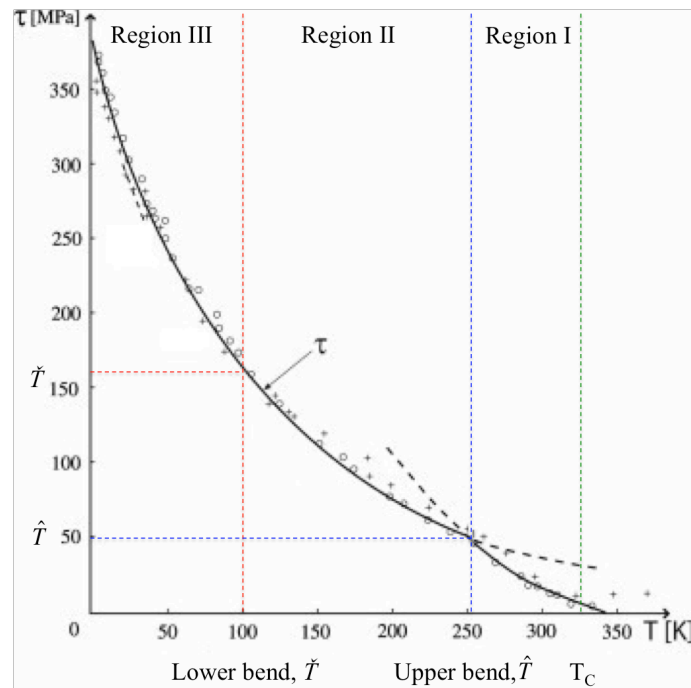


Figure 10: CRSS on  $\{110\}$  of pure Fe single crystals, as a function of temperature. Figure adapted from [15].

Brunner and Diehl applied Seegers (1985) theory of kink-pair formation in screw dislocations to calculate the kink height during deformation in the three temperature regimes [46-48] where the following was concluded: In temperature regime I, the kink length corresponds to kink formation along  $\{112\}$  planes, which indicated that the deformation is dominated by  $\frac{1}{2}\langle 111 \rangle \{112\}$  screw dislocations. Furthermore, regime II and regime II consisted of similar type of deformation, i.e. kink formation along  $\{110\}$  plane, which corresponds to  $\frac{1}{2}\langle 111 \rangle \{110\}$  screw dislocations. However, Caillard's [15] in situ straining experiments on Fe in the temperature range 100K to 300K, revealed elemental  $\{110\}$  slip plane deformation with extensive cross slip. According to Caillard [49], some of the assumptions in Seegers kink-pair nucleation model were assumed to be incorrect. Furthermore, his experimental in-situ tests indicated a strong increase in stress as the temperature was lowered. The results were quite equivalent to that measured by Kuramoto et al [21], for two different orientations, illustrated by the crosses and circles in Figure 11. Kuramoto's results also emphasize the fact that the flow stress of bcc metals is dependent on the orientation of the crystal. This pronounced orientation dependence, is controlled by two crucial aspects; slip asymmetry and the non-planar spreading of screw dislocation cores, as explained earlier in the Theoretical Background. The orientation dependence of  $\alpha$ -Fe single crystals under uniaxial tension was examined in a previous study (bcc materials). Figure 12 shows the pronounced influence of the orientation on the yielding.

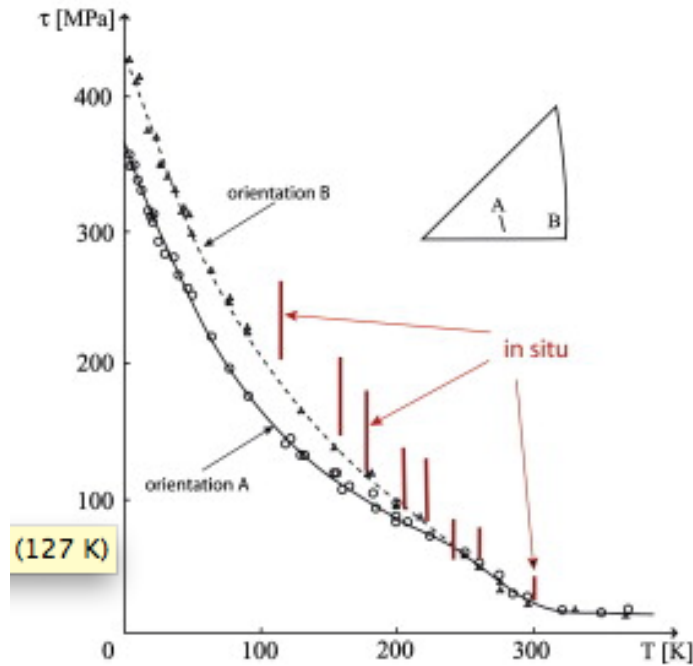


Figure 11: Temperature dependence of yield stress for iron single crystal [15]. Compared with tensile test by Kuramoto et al. [21].

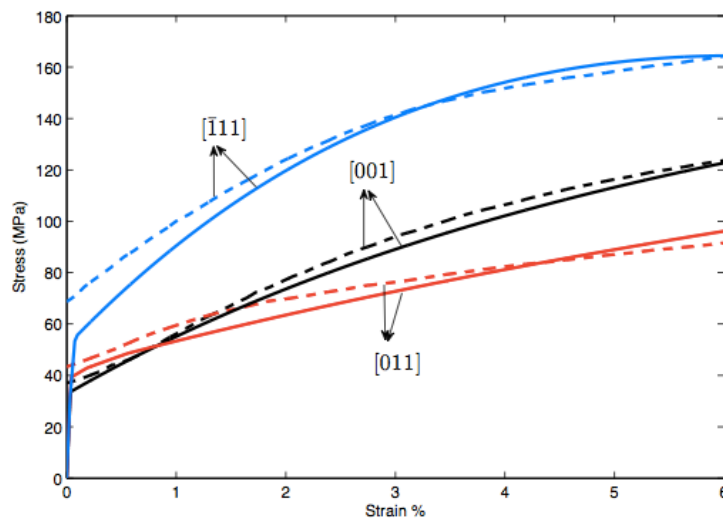


Figure 12: Tensile orientation dependence of [001], [011] and [111] oriented  $\alpha$ -Fe single crystals. Solid lines refer to simulations and dashed lines represent experiments [50].

Moreover, Caillard showed that the density of mobile dislocations increased, when the temperature decreased, i.e. when the stress decreased, shown in the in-situ images presented in Figure 13. The images also show that when the dislocations reach their critical configuration, the curved non-screw parts of dislocation loops move rapidly and trail a dipole of parallel screw segments. The image on the left side, shows the events before motion, the image in the middle is after motion, and the image on the right side shows the differences before and after motion.

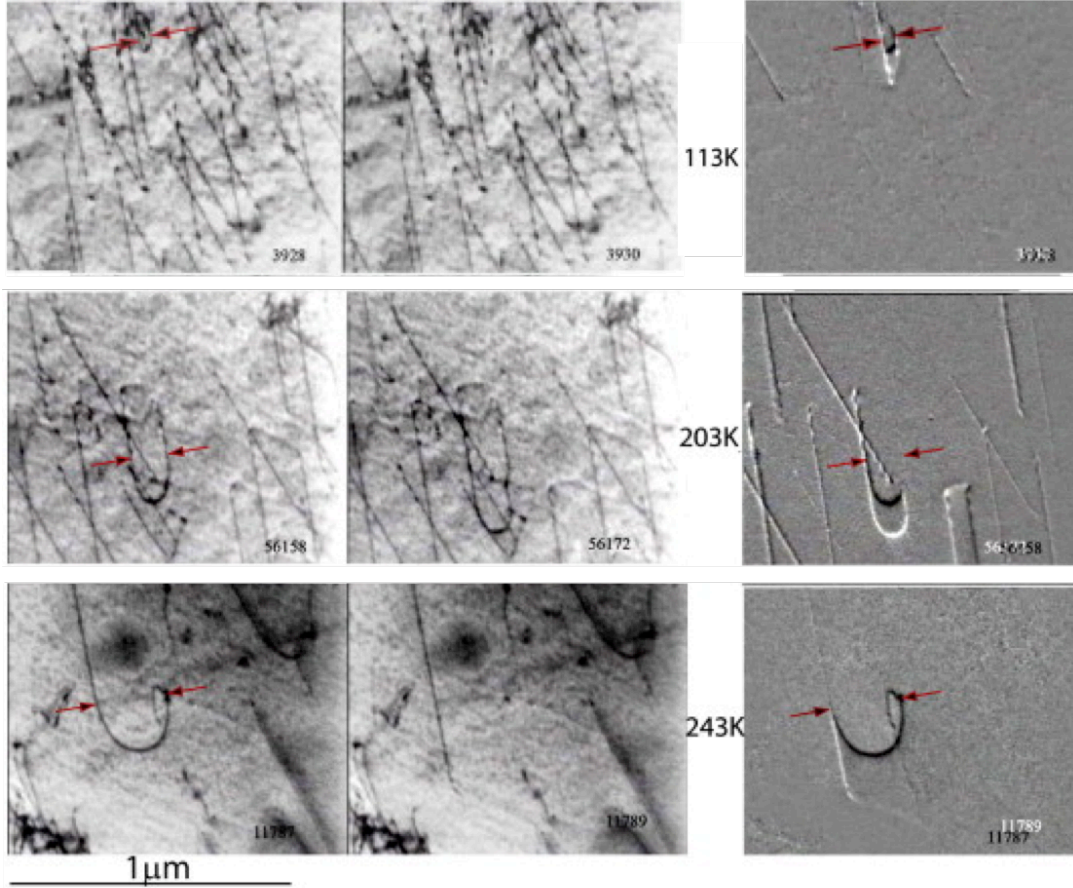


Figure 13: TEM in-situ images showing an increased dislocation density with decreasing temperatures. The red arrows are indicating critical screw dipole widths of dislocations. Figure adapted from [15].

Thermal activation analysis given in the literature [44, 51], explains the energetics of the process that governs the dislocation motion of bcc metals at low temperatures, i.e. in the regime govern by nucleation of double kinks. In this regime, the activation energy corresponds to the free Gibbs energy,  $\Delta G$ , required to displace a segment of dislocation to the next Peierl's valley. This energy is considered to be equal to the activation enthalpy only when the activation entropy terms are negligible [44]. Earlier investigations found that for iron, the Gibbs free energy associated with the double kink nucleation, can be approximated by the corresponding activation enthalpy. G. Taylor [22] considered the thermodynamics of dislocations glide, relating the thermodynamical quantities to experimental measurements of bcc metals. The energy balance during plastic flow caused by thermal activation and the thermal component, is written as

$$G^* = H^* - TS^* \quad \text{and} \quad S^* = -\left(\frac{\partial G^*}{\partial T}\right)_{\tau^*} \quad (5)$$

Where  $G^*$  is the activation energy,  $H^*$  is the activation enthalpy and  $S^*$  is the activation entropy. The rate equation for plastic flow controlled by thermal fluctuations were written as follows

$$\dot{\epsilon} = \dot{\epsilon}_0 e\left(-\frac{G^*(\tau)}{kT}\right) \quad (6)$$

where  $\dot{\varepsilon}$  is the shear strain rate,  $\dot{\varepsilon}_0$  is a constant which mainly depends on the dislocation density, vibration frequency and strain per successful activation,  $k$  is the Boltzmann constant,  $T$  is the absolute temperature.  $G$  is the change in Gibbs free energy of activation, which is strongly dependent on the shear stress  $\tau$ . By differentiation the rate equation with respect to temperature at a constant stress, the activation enthalpy,  $H^*$ , can be written as follows

$$H^* = G^* - T \left( \frac{\partial G^*}{\partial T} \right)_{\tau^*} = kT^2 \left( \frac{\partial \ln \left( \frac{\dot{\varepsilon}}{\dot{\varepsilon}_0} \right)}{\partial T} \right)_{\tau^*} \quad (7)$$

At a given temperature, effective stress and dislocation velocity are related so that  $\tau^* = \tau^*(T, \dot{\varepsilon}/\dot{\varepsilon}_0)$  and  $H^*$  can be re-written as

$$H^* = -kT^2 \left( \frac{\partial \ln \left( \frac{\dot{\varepsilon}}{\dot{\varepsilon}_0} \right)}{\partial \tau^*} \right)_T \left( \frac{\partial \tau^*}{\partial T} \right)_{(\dot{\varepsilon}/\dot{\varepsilon}_0)} = TV^* \left( \frac{\partial \tau^*}{\partial T} \right)_{(\dot{\varepsilon}/\dot{\varepsilon}_0)} \quad (8)$$

The activation volume,  $V$ , has been introduced to the relation in Eq. (8) and is a measure of the work done by the external stress during the activation process. By definition, the activation volume is the partial derivative of the activation free energy with respect to stress at constant temperature. Based on the strain rate equation and  $\Delta H = \Delta G$ ,  $V$  is deduced as

$$V = - \left( \frac{\partial \Delta H(\tau)}{\partial \tau} \right)_T = kT \left( \frac{\partial \ln(\dot{\varepsilon}/\dot{\varepsilon}_0)}{\partial \tau} \right)_T \quad (9)$$

This volume includes burgers vector of the glide dislocation so that  $V^* = bA^*$ , where  $A^*$  is known as the activation area. Many author prefer to use  $A^*$  rather than  $V^*$ , because it represents the area swept by the dislocation during activation. Furthermore, Naamane et al. [44] fitted the experimental data to the empirical formula in Eq. (10)

$$\Delta H = \Delta H_0 \left( 1 - \left( \frac{\tau^*}{\tau_0} \right)^p \right)^q \quad (10)$$

where  $\tau_0$  is a parameter corresponding to the extrapolation of  $\tau^*$  at the absolute zero temperature,  $\Delta H_0$  is the total activation energy necessary to overcome the lattice resistance without the help of external forces.  $p$  and  $q$  are fitting parameters. The purpose of the thermodynamically analysis is to identify the rate-controlling deformation mechanisms amongst several possible processes, which in the case of bcc metals means finding what is responsible for the strong temperature dependence of the yield and flow stresses at low temperatures. The above paragraphs emphasized some recent developments in the understanding of the slip system activity of bcc crystals and the connections between the core structure and the intrinsic properties. These theories will be taken into account for discussing the present results, and are of highly interest in order to create a wider understanding for the deformation mechanisms in bcc metals at lower temperatures.

## 2.2. Nanomechanical testing

A significantly part of this thesis are based on nanomechanical testing, thus it is natural to include this chapter concerning some of the fundamentals of nanoindentation and compression testing as well as a overview of the analysis methods related to the testing methods.

### 2.2.1. Nanoindentation

Nanoindentation instruments provide a valid approach to investigate the mechanical characterizations of materials, such as hardness and Young's modulus. A correct and accurate exploitation of experimental data from nanoindentation tests necessitates a full understanding of the nanoindentation principle. In the following paragraphs, the basics of nanoindentation will be presented.

The method nanoindentation was developed to measure the hardness and elastic modulus of a material from indentation load-displacement data, obtained during one cycle of loading and unloading. Although the most widely used probe for nanoindentation is the three sided Berkovich indenter, the system applies to a variety of axisymmetric indenter geometries [52]. In a nanoindentation test where a sharp indenter as Berkovich indenter is used, plastic deformation occur even at very early stage of loading. The response from the indentation is usually presented in a recorded load-displacement curve, or  $P-h$  curve as illustrated in Figure 14 (b). Parameter  $P$  designates the load and the  $h$  refers to the displacement relative to the initial undeformed surface. The three important quantities that must be measured from the  $P-h$  curves is the maximum load,  $P_{max}$ , the maximum displacement,  $h_{max}$  and the elastic unloading stiffness,  $S = dP/dh$ , defined as the slope of the upper portion of the unloading curve during the initial stages of unloading (also referred to as the contact stiffness). Another important quantity is the final depth,  $h_f$ , which is the permanent depth of penetration after the indenter is fully unloaded. The analysis used to determine the hardness,  $H$  and the elastic modulus,  $E$ , is essentially an extension of the method proposed by Doerner and Nix [53].

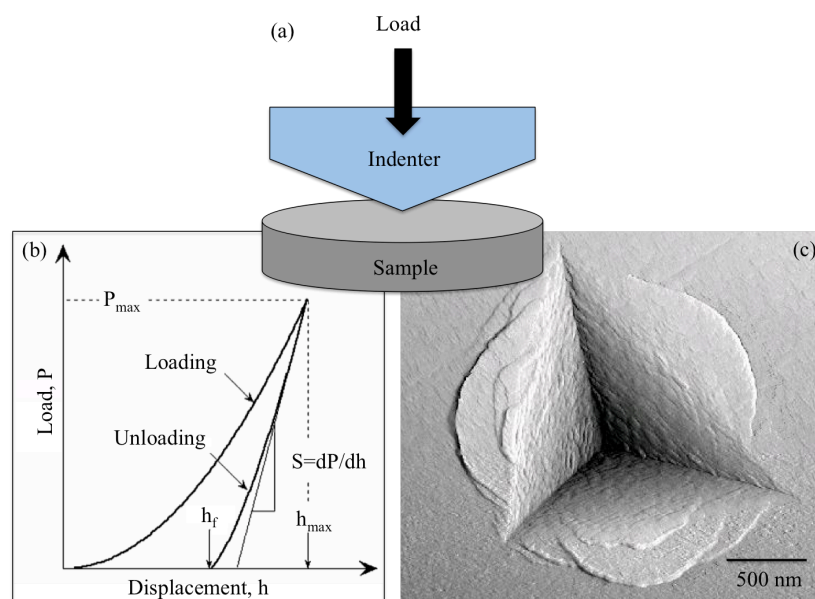


Figure 14: Illustration of the principles behind nanoindentation with (a) an indenter penetration a sample surface, (b) the corresponding P-h curve and (c) the residual imprint in the sample surface.

The procedure used to measure  $H$  and  $E$  is based on the unloading process shown schematically in Figure 15, in which it is assumed that the behavior of the Berkovich indenter can be modeled by a conical indenter with a half-Included angle, that gives the same depth-to-area relationship,  $\phi=70,3^\circ$ . The basic assumption is that the contact periphery sinks in, in a manner that can be described by models for indentation of a flat elastic half space by rigid punches of simple geometry. The amount of sink-in,  $h_s$ , is given by:

$$h_s = \epsilon \frac{P_{max}}{S} \quad (11)$$

where  $\epsilon$  is a constant depending on the geometry of the indenter and  $S$  is the stiffness. Using this equation to approximate the vertical displacement of the contact periphery, it follows from the geometry of the Figure 15, that the depth along which contact is made between the indenter and the specimen,  $h_c = h_{max} - h_s$ , is:

$$H_c = h_{max} - \epsilon \frac{P_{max}}{S} \quad (12)$$

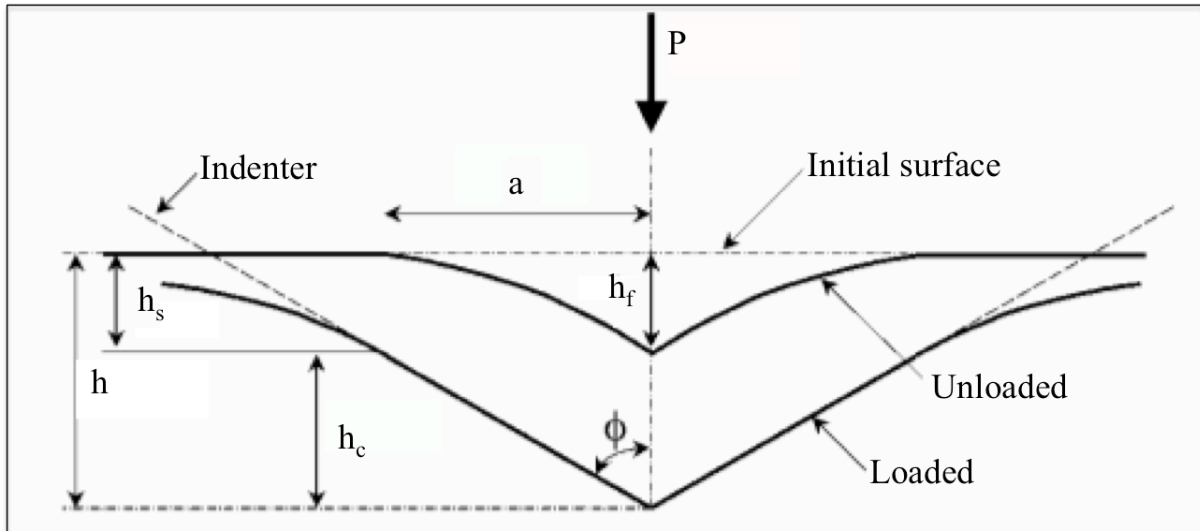


Figure 15: Schematic illustration of the indentation geometry with the parameters characterizing the process. Figure adapted from [52].

By considering  $F(d)$  as an “area function” that describes the projected (or cross sectional) area of the indenter at a distance  $d$ , back from its tip, the contact area  $A$  is then:

$$A = F(h_c) \quad (13)$$

After determining the contact area, the hardness can be estimated from the maximum load,  $P_{max}$ , divided by the contact area:

$$H = \frac{P_{max}}{A} \quad (14)$$

Measurement of the elastic modulus follows from its relationship to contact area and the measured unloading stiffness ( $S$ ), through the relation:

$$S = \beta \frac{2}{\sqrt{\pi}} E_{eff} \sqrt{A} \quad (15)$$

where  $E_{eff}$  is the effective elastic modulus and  $\beta$  is a dimensionless parameter used to account for deviations in stiffness caused by lack of asymmetry for pyramidal indenters. The indenter is usually made of diamond, which is strongly resistant to deformations but cannot be treated ultimately as rigid. In general it is known from contact mechanics (Johnson 1985) that when an indenter is deformable, the effective elastic modulus  $E_{eff}$  should be defined by

$$\frac{1}{E_{eff}} = \frac{1 - \nu^2}{E} + \frac{1 - \nu_i^2}{E_i} \quad (16)$$

The effective elastic modulus takes into account the fact that elastic displacements occur in both the specimen, with Young's modulus  $E$  and Poisson's ratio  $\nu$ , and the indenter with elastic constants  $E_i$  and  $\nu_i$ . When the tip of an indenter consists of diamond, the values of  $E_i = 1141$  GPa and  $\nu_i = 0,07$  are commonly adopted.

To keep the chapter to a reasonable length related to the present work, the focus in this chapter has been limited to the behavior of monolithic materials that can be described as elastic-plastic half spaces. There are, of course, other important issues related to nanoindentation that must be considered when applying the methods to e.g. thin films. The application of nanoindentation has in the recent years been developed into wider specters, whereas loading and compression of nanostructures have been an important topic in many fields. The following chapter will give an introduction to the fundamentals underlying pillar compression, which is also the main testing method used in this thesis.

### 2.2.2. Pillar compression testing

The principle behind pillar compression and some concerns related to pillar geometry and testing will be presented in the following paragraphs. Compression pillar experiments are a popular technique to investigate small scale behavior of single crystalline metals. The technique developed by Uchic et al. [54], consist of focused ion beam (FIB) that is used to mill a cylindrical sample that can be compressed using a flat punch in a nanoindenter device. In this manner, stress-strain curves from pillars with diameters down to 1  $\mu\text{m}$  or smaller, can be obtained from the plastic deformation induced under a more uniaxial stress state.

The technique offers very interesting prospects for the study of slip systems and plasticity. The absence of constraining material around the pillar allows slip systems to be activated by controlling the crystallographic orientation of the pillar with respect to the loading axis, hence the critical resolved shear stresses on individual systems may be measured. These features, coupled with analysis techniques such as electron backscatter diffraction and in-situ techniques, makes it possible to correlate individual slip event of dislocations to the formation of slip traces on the pillars surface.

Despite the popularity of micro and-nano compression tests, it still has some intrinsic shortcomings. The main problem is that indentation involves a complex stress-strain field underneath the indenter depending on the specific tip geometry. There are several experimental variables that may affect the accurate measurements. These variables include aspect ratio  $\alpha$  (the ratio of height  $h$  and diameter  $d$  of the pillar), size of substrate below the pillar, taper angel  $\theta$  (the angel between the tangent of wall and axis of the pillar), misalignment between the pillar axis and the compression direction, and stiffness of the substrate [55].

As for all experimental techniques, sample geometry, control of experimental parameters and sample details is important in obtaining accurate and repeatable measurements. Recent investigations have shown that factors like aspect ratio of the pillar ( $H/D$ ) and tapering angel of the pillar are a few among several factors that influence the test results from the experiment [9, 56]. Additionally, it was proven by using a finite element modeling that pillars with an aspect ratio between 2 and 3 obtain most accurate results [56]. Likewise, the optimal pillar shape has a taper angel as small as possible and a top-pillar radius to base-pillar radius ratio between 0.2 and 0.5. The more tapered the pillar is, the further up the pillar reaches the influence of the base and the less uniaxial is the stress state in the pillar. If the top-diameter is too small, the pillar results in a sink-in into the sample surface, hence the measured displacement does not accurately reflect the deformation applied to the pillar [56]. The pillar tapering angel can be determined by a simplified consideration using the pillar height  $h$ , the pillar base diameter  $D_b$  and the pillar top diameter,  $D_t$  as schematically illustrated in Figure 16 [5].

Pillars are usually fabricated by focused ion beam preparation, which can become a significant issue for pillars in small scale ( $<300\text{nm}$ ), since the volume affected by FIB-induced damage (e.g. Ga implanation) increasingly impair the probed volume. As a consequence, it is impossible to accurately study defect-free, FIB-fabricated pillars with smallest diameters [57]. However, in this investigation, pillars are fabricated with a diameter of approximately  $1\mu\text{m}$ , hence it is assumed that this effect would not influence the results.

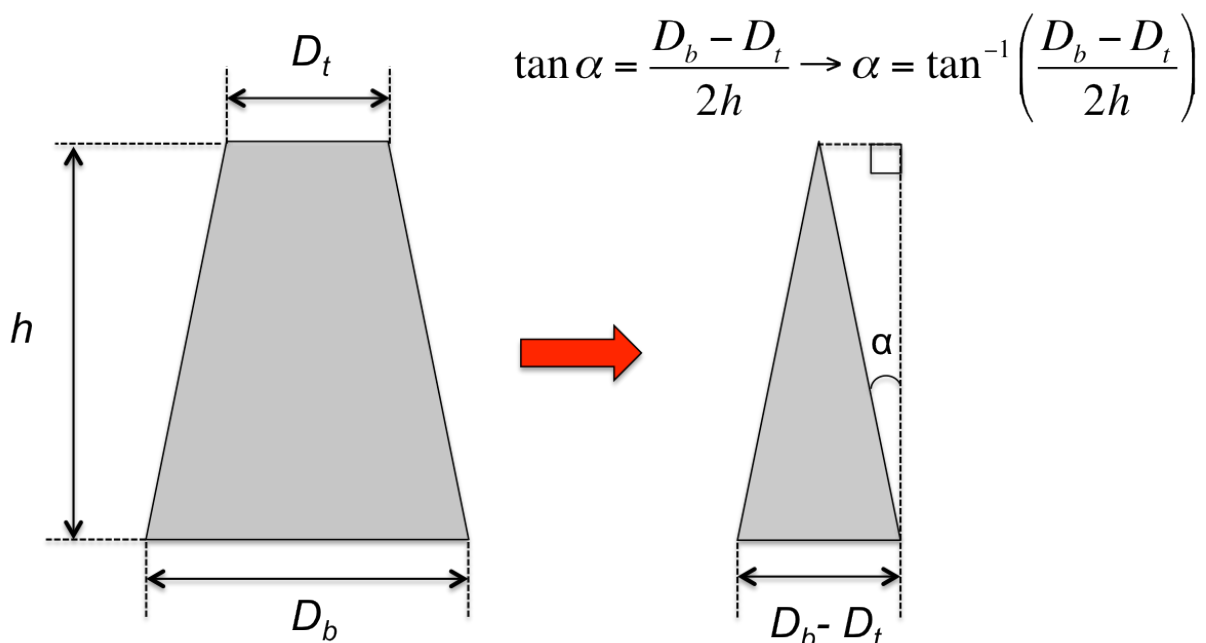


Figure 16: Tapered angel determination. Sketch adapted from [5].



### 2.2.3. Determining mechanical properties

The micro pillar compression test is very similar to its macro scale counterpart except for the specimen size, its fabrication process and its boundary conditions. The rigid punch is impressed on a micro pillar, and the load and the displacement are measured simultaneously. The load-displacement data recorded from micro-pillar compression test can be converted to the engineering stress and engineering strain data using the following equations:

$$\sigma = \frac{4F}{\pi d_t^2} \quad (17)$$

$$\varepsilon = \frac{\Delta}{H_0} \quad (18)$$

where  $\sigma$  is the stress,  $\varepsilon$  is the strain,  $F$  is the applied force on the pillar,  $\Delta$  the displacement,  $d_t$  the diameter of the pillar, and  $H$  is the height of the pillar. During the pillar compression there will be deformation inside the pillar and elastic deformation in the indenter and under the pillar as schematically illustrated in Figure 17. The displacement in the indenter and pillar base can be estimated and removed from the measured displacement. The result is a more accurate value of the displacement inside the pillar.

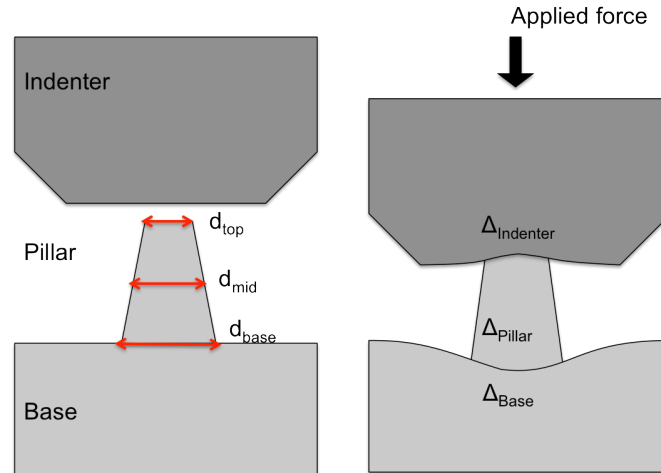


Figure 17: Schematic illustration of a pillar deformation, and the displacement in the indenter, pillar and the base (substrate) as a result of the compression.

One of the models widely used in the literature for pillar compression, are the one for the Sneddons compliance. The deformation of the pillar into the substrate can be described by Sneddons solution [58], where he considered the sinking effect of a cylindrical punch indenting into an elastic half space, where the half space compliance can be calculated by the following equation

$$C_{Sneddon} = \frac{(1 - \nu^2)\sqrt{\pi}}{2E\sqrt{A_p}} \quad (18)$$

where  $C_{Sneddon}$  is the half-space compliance,  $E$  is the Young's modulus,  $\nu$  is the Poisson's ratio and  $A_p$  is the contact area between the punch and the half-space material. Equation (18) can be applied to the micro compression test by assuming the punch to be the pillar and the half-space material to be either the indenter and/or substrate. Thus, the deformation of indenter and

substrate are given in terms of their compliance by considering the system as series springs consisting of the indenter, pillar and substrate [55].

$$\Delta_{Indenter} = C_{Indenter}f, \Delta_{Base} = C_{Base}f \quad (19)$$

where  $f = \pi r^2_{indenter}P$ , is the applied force on top of indenter and  $p$  is the pressure. The pillar deformation then can be given by the three following equations, (20)-(22) [5, 18].

$$\Delta_{Indenter} = \frac{1 - \nu_{Indenter}^2}{E_{Indenter}} \left( \frac{F}{d_{top}} \right) \quad (20)$$

$$\Delta_{Base} = \frac{1 - \nu_{Base}^2}{E_{Base}} \left( \frac{F}{d_{Base}} \right) \quad (21)$$

$$\Delta_{Pillar} = \Delta_{Measured} - \Delta_{Indenter} - \Delta_{Base} \quad (22)$$

Where  $d_{top}$  and  $d_{base}$  are the diameter of the top and base surface of the pillar, respectively and  $\Delta_{pillar}$  and  $\Delta_{measured}$  are the pillar displacement and measured displacement respectively.

### 2.3. Slip mechanisms in bcc pillars

The study of bcc pillars may represent a challenge for the researchers because of the materials intrinsic properties, which can lead to unpredictable results. Moreover, to validate an experimental result, it is necessary to reproduce many experiments to obtain comparability. With the same procedure of the experimental work, analytical theory, geometry and testing parameters, a greater fundamental understanding for the intrinsic phenomena during pillar compression might be established. In this chapter it is focused to present a review of some recently conducted work of bcc pillars. Two of the articles presented in this section, are work to be published soon [2, 24]. The results are highly interesting, since the experiments are considering the same material and loading directions considered in this thesis. A comprehensive study of the results obtained in Rogne and Thaulow's work, might contribute to predict some deformation behavior in the present work. However, the experiments in this thesis are performed at low temperature, which will be considered during analysis of the latter experiments performed at room temperature. Probably the feature that most distinguishes bcc pure metals from their fcc and hcp counterparts, is the strong temperature dependence of the yield and flow stresses at low temperatures and its concomitant effect on slip geometry. The chapter shall therefore further concentrate on the aspects around pillar deformation conducted at lower temperature. Moreover, it is also used other research articles in the literature to supplement the content of various topics discussed in this chapter.

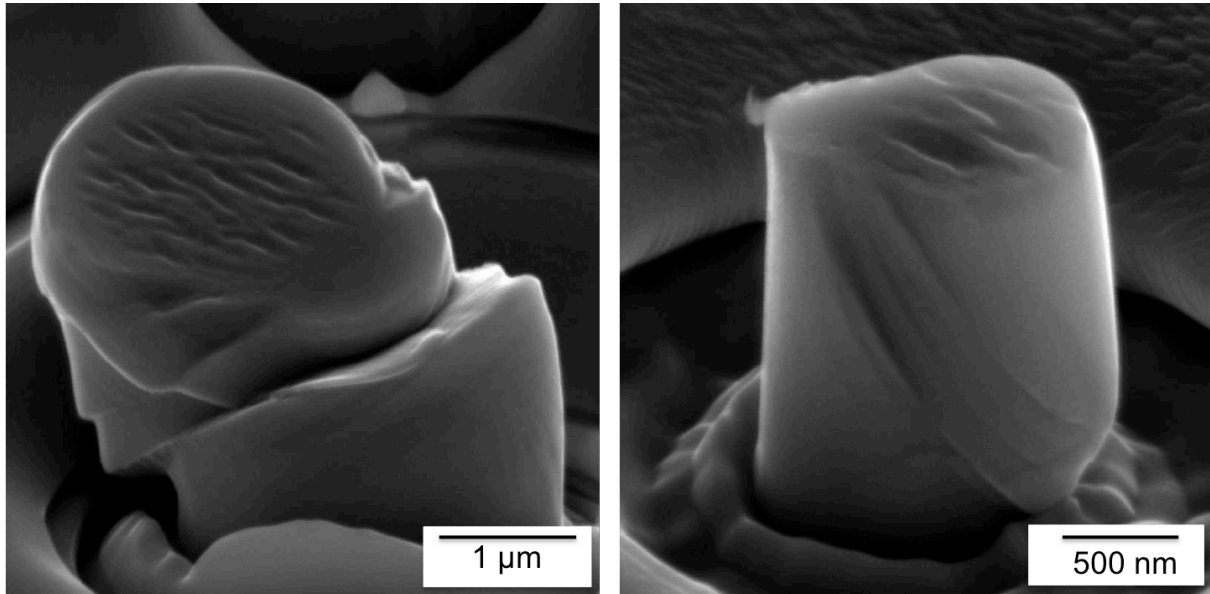
### 2.3.1. Slip system analysis

Activation of slip planes is complicated. It generally strongly depends on impurity content, temperature, on the loading axis and the sense of shearing in the crystallographic plane. In this context, impurity content will not be considered since it has not been in focus in this thesis. Analysis of slip traces has been used for many decades to directly observe slip. Deformation experiments as tension, compression, bending and orientation, results in the extrusion of slip planes onto the free surfaces. These slip traces can be imaged in several ways, including scanning electron microscopy (SEM), optical microscopy, transmission electron microscopy (TEM), X-ray diffraction analysis and atomic force microscopy. A great part of the studies of pillar deformation focus on size effects [12, 13, 18, 59, 60], and less attention has been devoted to direct observation of the slip planes.

Kim et al. [61] studied slip traces in niobium pillars using SEM and found the planes to generally agree with  $\{110\}$  slip for their (001) oriented pillars in both tension and compression. Han et al. [62] arrived at the same conclusion from his study of vanadium nanopillars, i.e. that slip likely occurs on  $\{110\}$  planes. Additionally, slip has been reported in pure bcc metals to occur along the same close packed directions on other less densely packed planes, after slip begins on the  $\{110\}$  family of planes [2, 24, 63]. These second set of planes are termed secondary slip planes and requires more energy compared to the primary planes. It is suggested in the literature that the primary slip system is the one with the largest resolved shear stress and the activation of other slip systems also follows the Schmid law [51]. In the following paragraphs, the experimental results analyzed in Rogne and Thaulow's work [2, 24], that is applicable to the present work, will be presented.

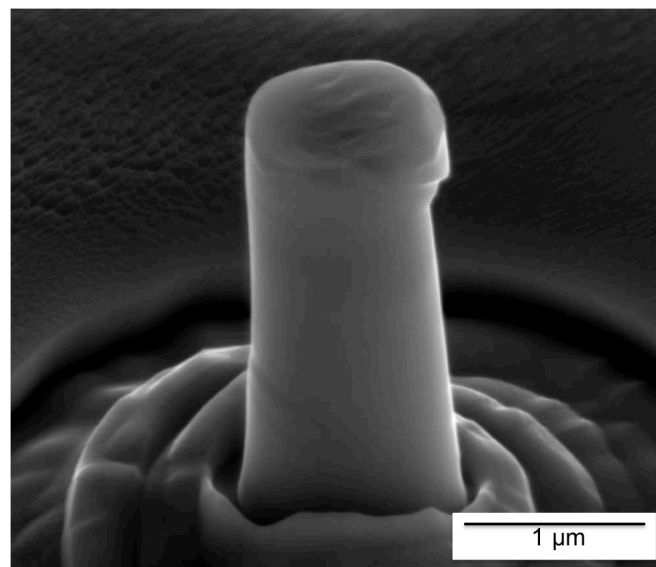
In their experiments, Fe pillars were compressed on  $\langle 149 \rangle$ ,  $\langle 235 \rangle$ ,  $\langle 011 \rangle$  and  $\langle 111 \rangle$  orientations, in order to determine whether the favored slip system was of type  $\{110\}\langle 111 \rangle$  or  $\{112\}\langle 111 \rangle$ . From pillars loaded on the  $\langle 149 \rangle$  orientation, both primary and secondary slip systems were observed as the only operation slip system. The authors suggest that the evidence of secondary slip system instead of primary in  $\langle 149 \rangle$  orientation could be caused by two reasons; After the sample preparation, roughness on the pillar top-surface were observed. This small-ripple like roughness can cause a stress distribution that is beneficial for the secondary slip systems. It is further suggested that the pillars with the smallest diameter are more exposed to this effect since the roughness become large compared to the diameter and the local stress concentrations can become high enough to trigger deformation on a secondary slip systems. For the largest pillars, this stress distribution caused during loading can easily be redistributed early under the top-surface. The other suggestion is that large pillars include several dislocations on each available plane. Hence the highest stressed plane will determine where the deformation starts. As the pillar size is reduced it become less likely to find a favorable dislocation segment on the highest stressed plane. Consequently a secondary plane with a more preferred dislocation segment might initiate the deformation.

Figure 18 shows the deformation behavior of two pillars loaded in  $\langle 149 \rangle$  orientation, with slip identified along the  $\{110\}$  primary plane for the largest pillar ( $d= 2,1\mu\text{m}$ ) and a  $\{110\}$  secondary plane for the smaller pillar ( $d= 880\text{nm}$ ). The primary slip system  $\{110\}\langle 111 \rangle$  had the highest stressed plane, with an Schmid factor of 0.50, followed by the  $\{110\}$  secondary plane with a Schmid factor of 0.47, corresponding to Figure 18 (a) and (b) respectively. It was observed that the secondary slip system were dominating the deformation in a fraction of the samples, as the pillar diameter were decreased below  $1\mu\text{m}$ , and secondary slip activation were most frequently seen at diameters of about 800nm, also seen in Figure 18 (b).



**Figure 18: SEM micrograph of iron pillars loaded along the  $\langle 149 \rangle$  direction, with activated slip planes illustrated by the stippled line [2].**

Also for the  $\langle 235 \rangle$  oriented pillars, it was evident that the primary  $\{110\}$  plane was carrying out the major part of the deformation, in combination with other unidentified planes with a lower Schmid factor, shown in Figure 19. It was found from slip trace analyses based on EBSD scans, that orientation  $\langle 235 \rangle$  have one plane for both the  $\{110\}\langle 111 \rangle$  and  $\{112\}\langle 111 \rangle$  system, with an equal Schmid factor of 0.45.



**Figure 19: SEM micrograph of iron pillar loaded along the  $\langle 235 \rangle$  direction, with a activated  $\{110\}$  primary plane [2].**

According to Rogne and Thaulow [2], slip mechanisms from orientation  $\langle 111 \rangle$ , were rather complicated to define, since the slip traces were distributed over the surface in a chaotic way. However, considering the observed slip traces from this orientation and other orientations, it is speculated that the slip occurs along two non parallel  $\{110\}$  planes for each of the three symmetrical  $\langle 111 \rangle$  directions. The deformation on  $\langle 011 \rangle$  orientated pillars, happened along two slip directions with two non parallel  $\{110\}$  planes, as seen in Figure 20. The dashed lines illustrate where the slip events are activated.

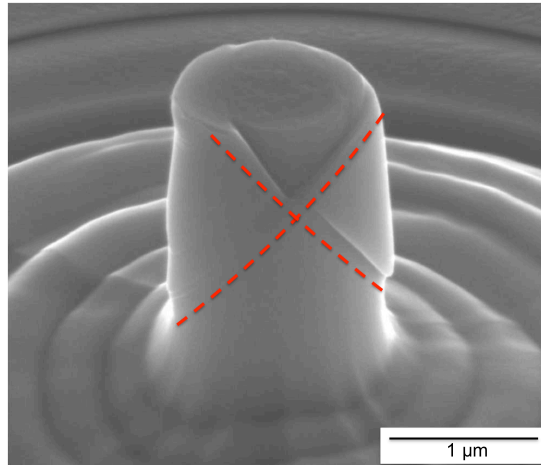


Figure 20: SEM micrograph of iron pillar loaded along the  $\langle 011 \rangle$  direction, with deformation activated along two non parallel  $\{110\}$  planes, illustrated by dashed lines [2].

For the  $\langle 001 \rangle$  oriented pillars there are four symmetric  $\langle 111 \rangle$  glide directions and along each direction, there are two equivalent  $\{110\}$  planes and one  $\{112\}$  plane. Loading on this orientation, multiple slip were expected along one or both of the slip systems of type  $\{110\}\langle 111 \rangle$  or  $\{112\}\langle 111 \rangle$ . Study of the slip traces revealed that the dominating slip system was  $\{110\}\langle 111 \rangle$ , where the slip happened in two non parallel slip planes of type  $\{110\}$  along each slip direction [2, 24]. During these investigations, traces of crystallographic slip on the pillar surface were compared with slip traces that were calculated based on EBSD scan, where the slip traces corresponded very well with the calculations. Also here, it was observed that slip were activated on the two non parallel slip planes of type  $\{110\}$ , marked by the green and blue lines in Figure 21(c). Furthermore it was revealed that if the slip direction were taken to be the  $[11\bar{1}]$  direction, the slip traces corresponded to glide partly on  $(101)$  and  $(011)$ . Slip traces corresponding to the  $\{112\}$  plane were also observed, as illustrated with the dashed line in Figure 21 (a). The pillar in Figure 21 is viewed from three positions with a  $90^\circ$  stage rotation between each picture. As a result of the four symmetrical slip directions for this orientation, the same slip traces is observed in all three pictures, as seen from the upper part of the pillar.

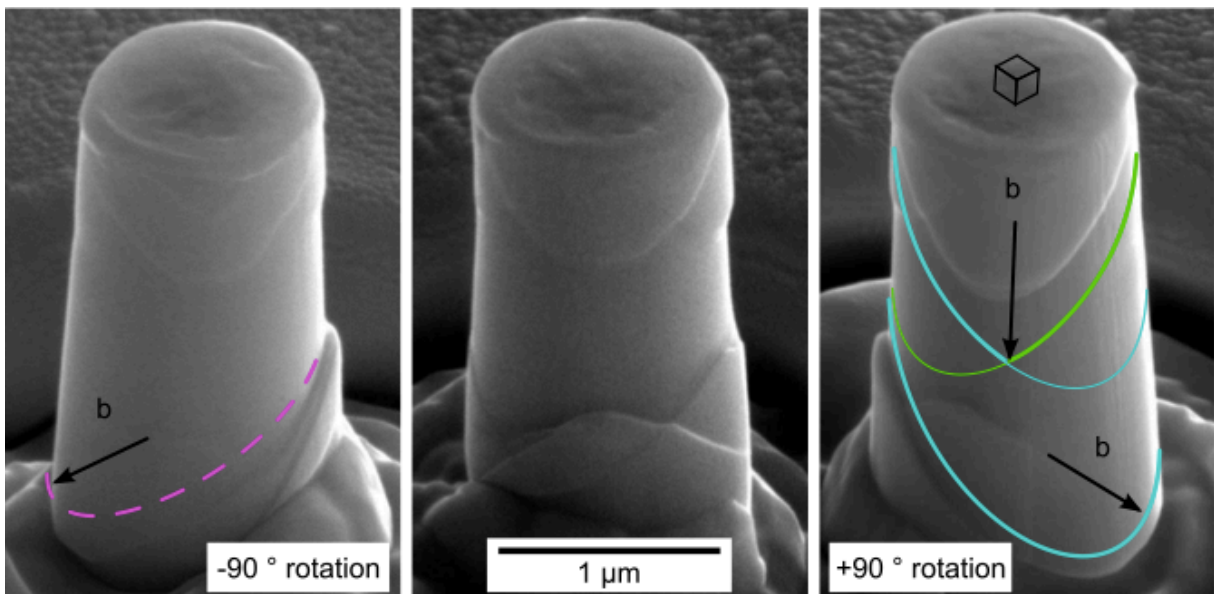
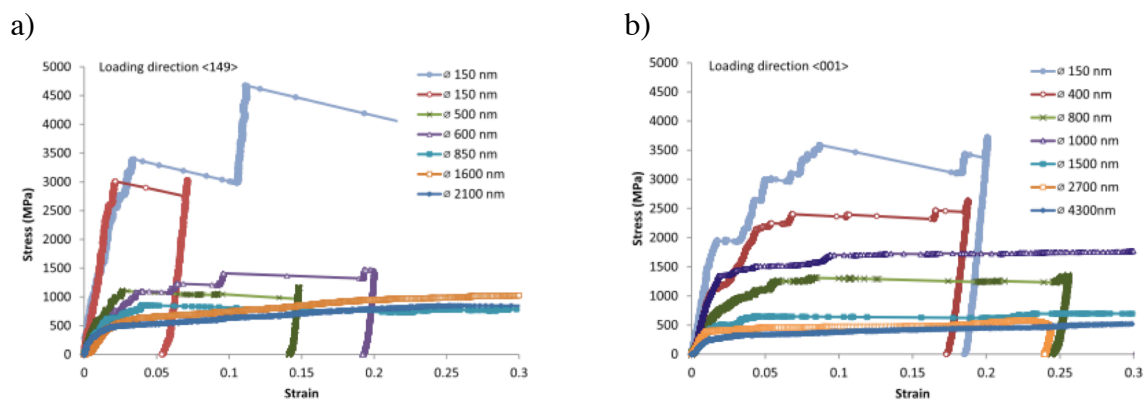


Figure 21:  $\langle 001 \rangle$  oriented iron pillar after deformation with the activated slip system  $\{110\}\langle 111 \rangle$  observed [24].

From the representative stress-strain curves it is observed for all orientations that the yield stress increase with decreasing diameter and the curves undergo a transition from smooth to a staircase like deformation, as the pillar diameter is reduced [2, 24]. The pillars with diameter above  $1\mu\text{m}$  exhibit relatively continuous stress-strain curves, whereas for smaller pillars strain bursts separated by nearly elastic loading segments appear. It is suggested that these characteristics reflects that local shear stresses must exceed a threshold before the dislocation source is activated and start to operate until it is exhausted and stops [64]. The stress-strain curves displays key features that are frequently observed in both fcc and bcc materials [11, 60, 63, 65]. Additionally, it was seen that the stress-strain curves for the smallest pillars behave different depending on slip orientation. For the single slip orientations  $\langle 149 \rangle$  and  $\langle 235 \rangle$ , the strain bursts are larger and starts at less strains than the multi slip orientations  $\langle 001 \rangle$ ,  $\langle 011 \rangle$  and  $\langle 111 \rangle$  as shown in Figure 22 (a) and (b) where the stress-strain data from single slip orientation  $\langle 149 \rangle$  and multi slip orientation  $\langle 001 \rangle$  are presented.



**Figure 22:** Stress strain curves from pillars with different diameters loaded along (a)  $\langle 149 \rangle$  and (b)  $\langle 001 \rangle$  direction [2].

The yield stress data of Fe pillars obtained from [24], have been compared with other results obtained on single-crystal iron samples of various types as seen in Figure 23 (Figure 23 is adapted from [2] with permission). Previous calculations of the theoretical strength [66] were used to consider the upper strength limit for loading along  $[001]$  and  $[111]$ , which were 12.7 GPa and 27.3 GPa respectively.

As seen from Figure 23, there is observed some deviation between calculated data [66], atomistic simulations [10] and some of the experimental results. E.g. atomistic simulations of single-crystal iron nano pillars are performed at conditions that are rather different from the experimental world, since the simulations are based on defect free crystals that are deformed at strain rates of  $5 \times 10^7$  and with a temperature of 0K. Under these conditions it is seen that the plasticity starts at the base with surface nucleation that moves upwards through the crystal. In this case, the simulation results were considered as an upper limit to the micropillar compression experiments. Furthermore, it is seen from Figure 23 that the MD simulations were lower than the density functional theory calculations. However, Brenner [67] obtained results that approached the theoretical value, by measuring the fracture stress of iron whiskers of single crystals close to defect free and deformation were expected to nucleate from the surface. The yield stresses obtained from the micro pillar compression experiments [24], were in the same range as for the iron whiskers, but for samples that were at least one order of magnitude smaller. It is suggested that the differences in the obtained data could be caused by the following reasons; The micro pillars are not defect free and the plasticity can start as soon

as the stress is high enough for moving an existing dislocation, additionally FIB milling introduces additional defects into the pillar [57].

The green dashed lines in Figure 23, represents Fukamachi's [68] results from his investigation on the effect of surface orientation on tensile testing of thin iron plates loaded in the [110] direction. At room temperature it was observed a strengthening effect, as the plate thickness became less than about 30 $\mu\text{m}$ . It was also seen that the strength was depending on surface orientation, when the plate thickness was less than 30 $\mu\text{m}$ . E.g. in plates thinner than 30 $\mu\text{m}$ , (001) plates were stronger than (1-10) plates. Additionally, the dependence of the strength on the surface orientation also became more pronounced with decreasing temperature. Finally, the source truncation theory by Parthasarathy et al. [69] were used and compared with the measured pillar compression data points, and the resulting prediction from the model failed within the same range as the micropillar results, seen from Figure 23.

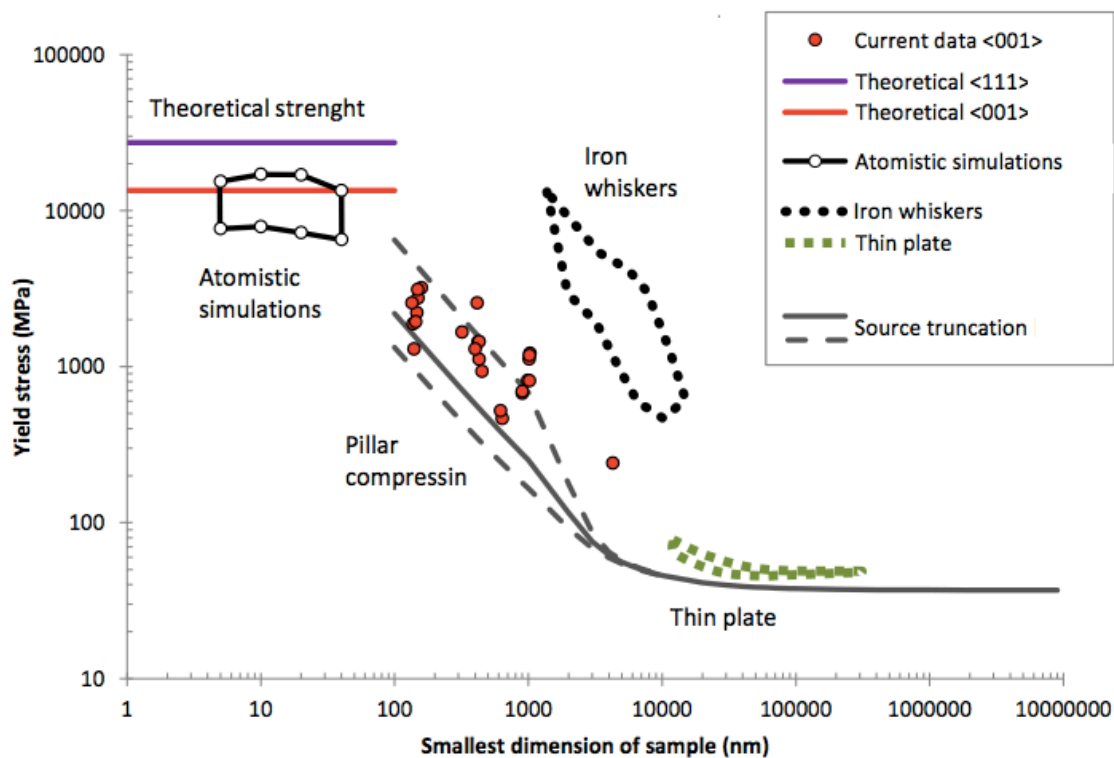


Figure 23: Comparison of yield stress from calculated theoretical strength [66], atomistic simulations [10], thin plate tensile test [68], iron whiskers [67] and source truncation [69].

The micropillar experiments presented in [24] revealed from the analyzed slip traces that the preferred slip system was of type  $\{110\}$ . The slip traces appeared as well defined and not wavy, hence it was concluded that contribution from cross slip was not a dominant part of the deformation under these experimental conditions. The waviness of slip steps has been observed in bulk single crystal studies where the wavy slip behavior is attributed to cross slip of  $a/2 \langle 111 \rangle$  screw dislocations [70, 71]. This deformation behavior is also seen in [001] oriented bcc pillars (W and Mo) [72]. In contrast, glide steps in deformed Nb pillars have been seen as well resolved on single crystallographic planes. Schneider *et al.* [63] observed this behavior even at high magnification pictures of the deformed pillar as shown in Figure 24 (b) and (d), in contrast to a deformed W pillar with wavy slip steps. In general, the deformation of bcc materials is controlled by the motion of long and straight screw dislocations. Their ability to cross slip between crystallographic planes which intersect along

the  $\langle 111 \rangle$  direction leads to wavy slip steps [72]. The cross-slip of screw dislocation may account for the deformation morphology of the large W pillars seen in Figure 24 (c). The well-resolved slip steps of Nb indicate that less cross slip occurred during plastic deformation. Additionally, in Nb pillars deformed to larger strains, contribution of secondary slip system was detected [63].

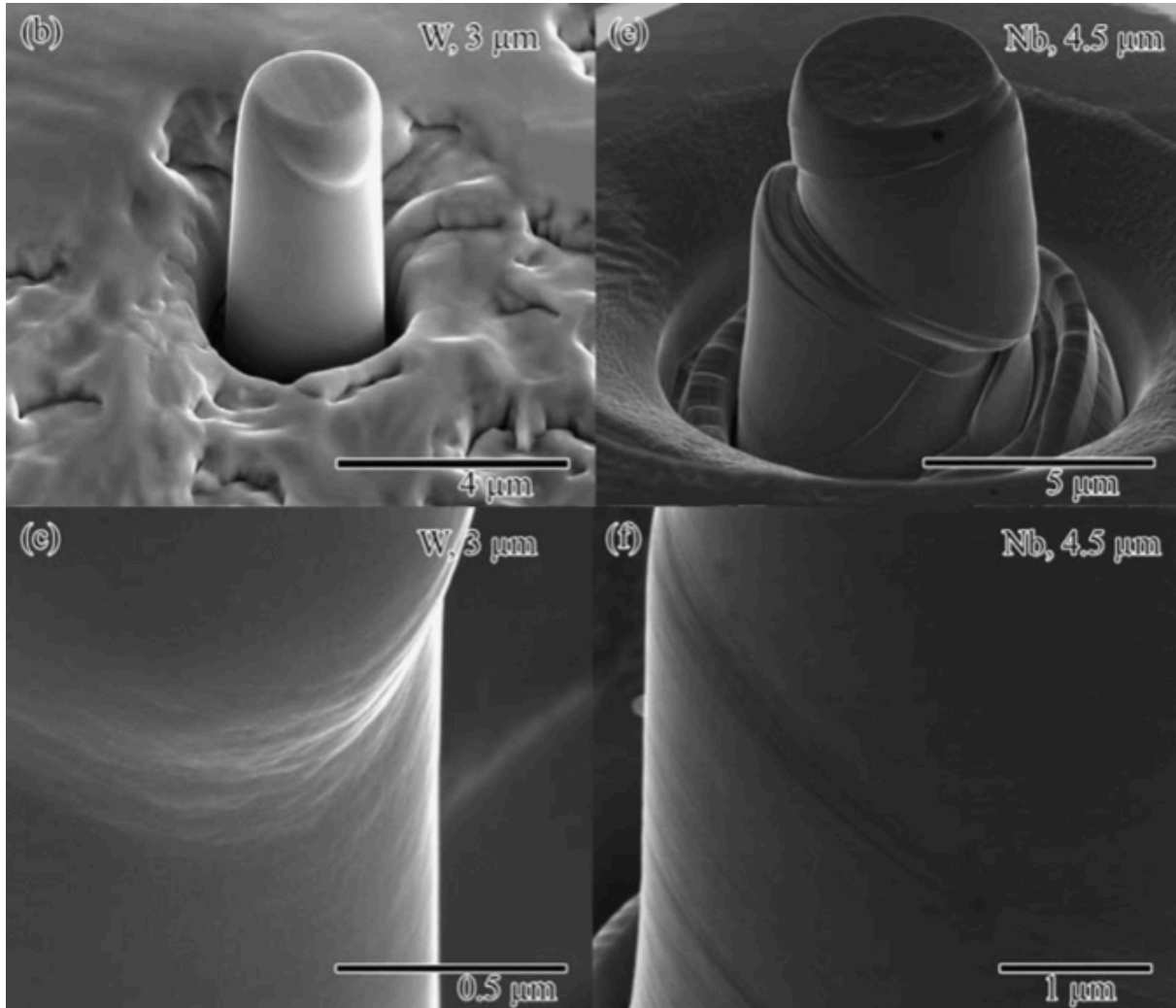


Figure 24: Post- compression SEM images of [235] oriented (a) 3 μm W and (b) 4.5 μm Nb pillars. (c) and (d) highlight differences in slip trace morphologies between W and Nb respectively [63].

Recent experiments involving compression of small scale pillars formed by focused ion beam (FIB) fabrication have shown that various factors influence the deformation. Dislocation motion occurs on various slip systems with screw dislocation being slower than edge dislocations, due to their non planar core structure and the associated need to overcome the Peierl's potential by thermal activation. However, the crystallographic slip in bcc metals is known to be complex and several possible mechanisms can influence the deformation behavior as well as size and temperature.



### 2.3.2. Low temperature deformation of bcc pillars

So far, most of small-scale mechanical tests have been done at room temperature [2, 24, 54, 59, 73], since it does not require the special modification of equipment. However, engineering materials are often used at lower temperatures than room temperature. Particularly, arctic environments as well as space- and marine applications, requires materials to serve at different thermal environments. Due to the increased use and interest of nanomaterials under different thermal environments [74], development of experimental techniques that reveals mechanical properties on small scale materials at different temperatures is necessary.

From the extensive literature of tensile and compression testing of single crystal bcc transition metals, several typical slip trace features emerge. At very low temperatures, slip appears to be planar. In this regime, the slip planes are often observed to be  $\{110\}$ , although for certain orientations and loading conditions,  $\{112\}$  slip is sometimes observed. At higher temperatures, the slip traces appear to become more wavy, diffuse and branched. These characteristics can arise even when the fundamental slip plane is  $\{110\}$ - type, since there are three  $\{110\}$ -type planes that intersect any  $[111]$  slip direction. (slip planes in transition bcc metals).

Recently (February 2014) Lee S.W, *et al.* [75] developed an *in-situ* cryogenic nanomechanical testing system by combining a nanomechanical tester, SEM and cryogenic systems where the mechanical properties of bcc Nb and W nanopillars at low temperature were investigated. A schematic illustration of the set up is shown in Figure 25. The set up consisted of a liquid nitrogen dewar connected to a vacuum shielded coolant transfer line that is mounted to a coldfinger assembly on the SEM. The cold finger inside the vacuum chamber, were connected to radiation shielded oxygen- free high thermal conductivity copper (OFHC) lines, in order to enhance the heat conduction between the sample stage and the coldfinger. Furthermore, the OFHC wires were mounted to the indenter tip, and the sample stage. The temperature was registered from temperature sensors (Si-diode) placed close to the sample and on the cold finger. Additionally, the sample stage consisted of titanium in order to obtain better cooling capability, because of its low thermal conductivity ( $21.9 \text{ Wm}^{-1}\text{K}^{-1}$ ). With this current set up, the experiments were successfully performed with cryogenic nanomechanical tests with the precise temperature control between 130 K and 298 K.

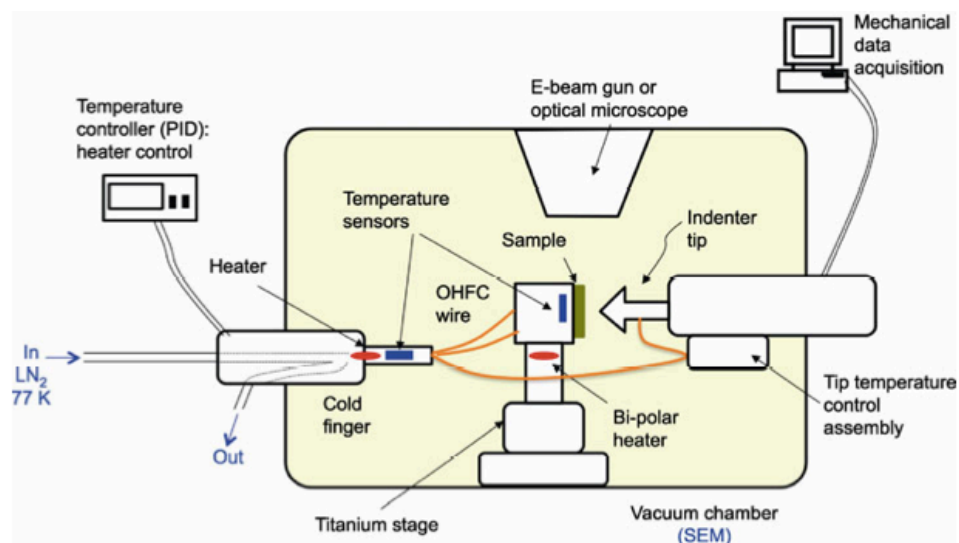


Figure 25: Schematic illustration of an *in-situ* nanomechanical tester interfaced with the cryogenic system [75].

The uniaxial compression tests were performed at  $-108,15\text{ }^{\circ}\text{C}$  (165K), with pillars in the size ranging from 400-1300 nm. Figure 26 shows snapshots from the *in-situ* compression of the Nb nanopillars with  $\langle 001 \rangle$  orientation. The SEM images reveal that the Nb pillars exhibit sharp and localized slip traces on the surface.

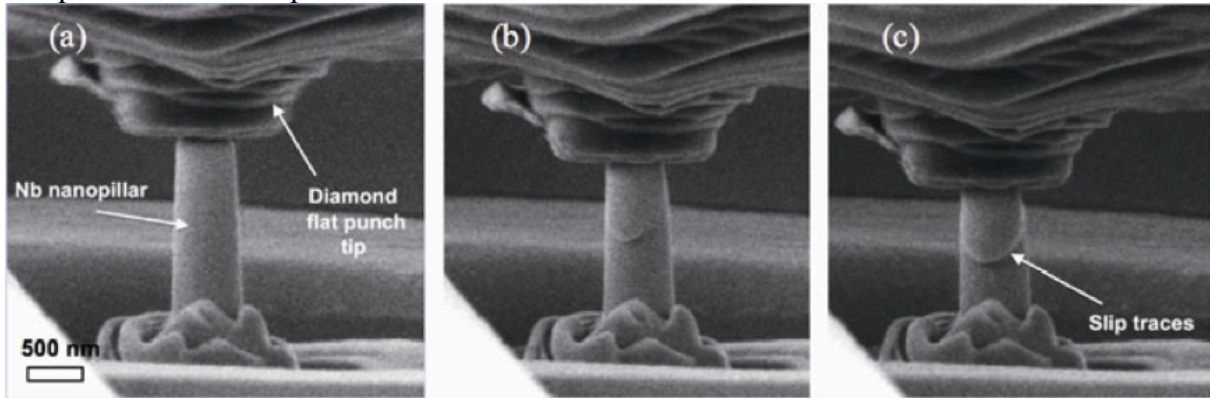


Figure 26: Snapshots from *in-situ* compression of Nb pillars with  $d=600\text{ nm}$ , showing a localized deformation during compression [75].

From the stress-strains curves presented in Figure 27, it is observed that stress-strain curves at 165 K exhibit higher yield strengths and larger strain burst sizes than those at 298 K for a given diameter. The higher yield strength makes sense because the intrinsic lattice resistance of bcc crystals is usually higher at lower temperature. At lower temperatures, the mobility of screw dislocations gets slower because the nucleation of double kink gets more difficult with the lower supplied thermal energy, resulting in the higher required stress for the operation of dislocation sources [75]. Lee, S.W *et al* also confirmed this by using a numerical calculation model (single arm source model), to calculate the intrinsic lattice resistance of Nb and W. The lattice resistance of Nb and W were 98 and 735MPa at 298 K, respectively, and 294 and 1226MPa at 165K, respectively. Hence, the intrinsic lattice resistance is obviously higher at 165K due to the low mobility of dislocations at low temperature. The larger strain burst observed at 165K, indicates that the dislocation activity for each strain burst is much more pronounced at a lower temperature, i.e. a dislocation source could generate more dislocations at lower temperatures. This effect was significantly higher for the pillars with  $d=400\text{nm}$ , compared to the pillars with  $d=1000\text{nm}$ .

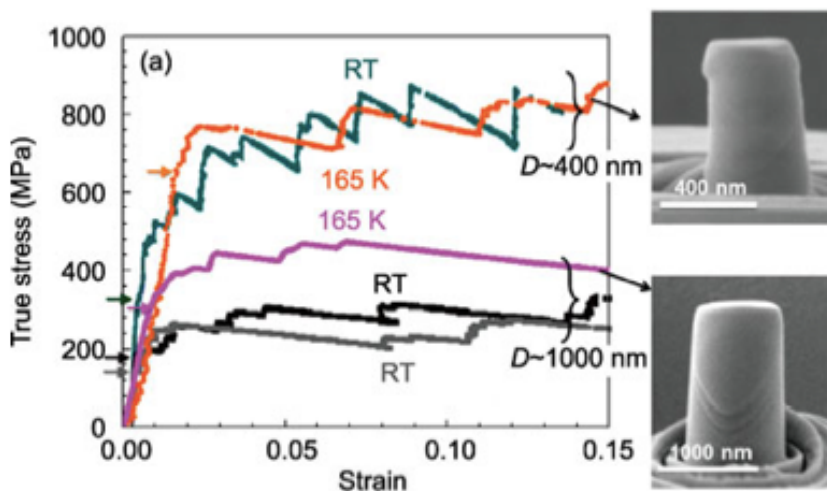


Figure 27: Stress-strain curves from compression testing of Nb pillars at room temperature and at 165 K [75].

The experimental cooling system produced by Lee S.W et al. [75] is complicated and not seen in any other pillar compression studies. Development of such experiments can shed a new light into the deformation mechanisms of several materials, and establish a fundamentally understanding of the dominating slip systems within different grain orientations, at lower temperatures. The work conducted in this thesis might be one step further in this direction, where the aim is to study the effect of orientation on the temperature dependence of bcc Fe pillars by analyzing stress-strain response as well as the deformation morphology for single slip and multiple slip configurations on the pillars. A cooling system based on liquid nitrogen and a coldfinger interfaced in a Scanning Electron Microscopy (SEM) is developed, with the purpose to cool down the sample to arctic temperatures. Micro- and nanopillars were FIB machined on the surface of Fe crystals oriented for single and multiple slip deformation and subsequently compressed in-situ with a picoindenter. Slip trace analysis was used to verify the activated slip systems. The results were compared to those of previous studies on iron pillars presented in this section. The following section will give an detailed description of the experimental work conducted in this thesis.

### 3. Experimental procedure

A clearly and chronological description of experimental procedures is important for understanding the experimental work result obtained. The following chapter will describe the sample preparation and testing methods with the corresponding operation parameters for the equipment used, in details.

#### 3.1. Sample preparation for General Metallographic, EBSD- and FIB-Analysis

When performing material testing at nanoscale, it is essential to have a sample surface as clean and plane as possible. Material characterization methods as EBSD, are very sensitive to crystalline perfection, and sample preparation is needed to remove any surface damage and impurities. A well repaired sample is a prerequisite to obtain a good diffraction pattern. Surfaces must be sufficiently smooth to avoid shadows on the diffraction pattern from other parts of the sample. The following sample preparation procedure, have been suitable and successful to obtain these requirements.

##### 3.1.1. Sample

The sample used in this study was a bcc  $\alpha$ -Fe provided by Alfa Aesar GmbH & Co KG- A Johnson Matthey company, and has a purity of 99,995% Fe. The sample is heat treated to obtain enlarged grains. The sample has a surface areal of 1 cm<sup>2</sup> and the height of the specimen was originally 5mm. However, approximately 0,1mm is removed during grinding and sample preparation.

##### 3.1.2. Grinding

The grinding was done mechanically in 3 steps, with silicon carbide (SiC) paper and performed using Struers Lectropol-5 at the Metallurgy Lab in IPM, NTNU. The grinding sequence started with coarse particle naps, and stepwise finer grained naps, as shown in Table 2. Between each grinding step, the sample was cleaned with ethanol and dried with a hairdryer, in order to leave the surface blank and clean. The backsides of the samples were also grinded with a coarse step (800 SiC paper) to ensure conductivity through the samples for further electropolishing. The sample surface was relative even and flat after grinding, which was also aimed for. To make the microstructure visible in SEM and optical microscope, electropolishing was further conducted, as explained in next section (3.1.3.).

Table 2: Grinding parameters used during mechanical surface preparations.

Step	Grinding paper	Time	Lubricant
1	P800 SiC	2 min	Water
2	P1200 SiC	5min	Water
3	P2400 SiC	5-10min	Water

##### 3.1.3. Electropolishing

The final step of the sample preparation was electropolishing, which was performed using a Struers Lectropol-5 at the Metallurgy Lab at IPM, NTNU. The electrolyte consisting of 95% methanol (CH<sub>3</sub>OH) and 5% sulfuric acid (H<sub>2</sub>SO<sub>4</sub>) was mixed. The electropolishing was performed in two steps as a result of not satisfying result after step 1, where grinding scratched were still visible on sample surface. Step 2 was performed in order to get a proper

visible microstructure in the microscope and a mirror-like surface. After completed electropolishing, the sample were quickly washed in the same manner as after the grinding steps. The satisfying procedure and the system parameters used are presented in Table 3.

**Table 3: Electropolish parameters used during step 1 and step 2.**

Step 1				Step 2		
Sample	Time [s]	Voltage [V]	Achieved current [A]	Time [s]	Voltage [V]	Achieved current [A]
FE4	40	15	1,16	60	15	0,98

### 3.2. Microindentation

Before performing EBSD analysis before nanomechanical testing, it is crucial to make a good location map on the surface, in order to locate the different areas with the crystallographic orientation of interest. The microindentations were performed at the Metallurgy Lab in IPM, NTNU where each indentation had a distance of 2 mm from each other. Applied force used was 0,3 N. The resulting location map is shown in Figure 28.

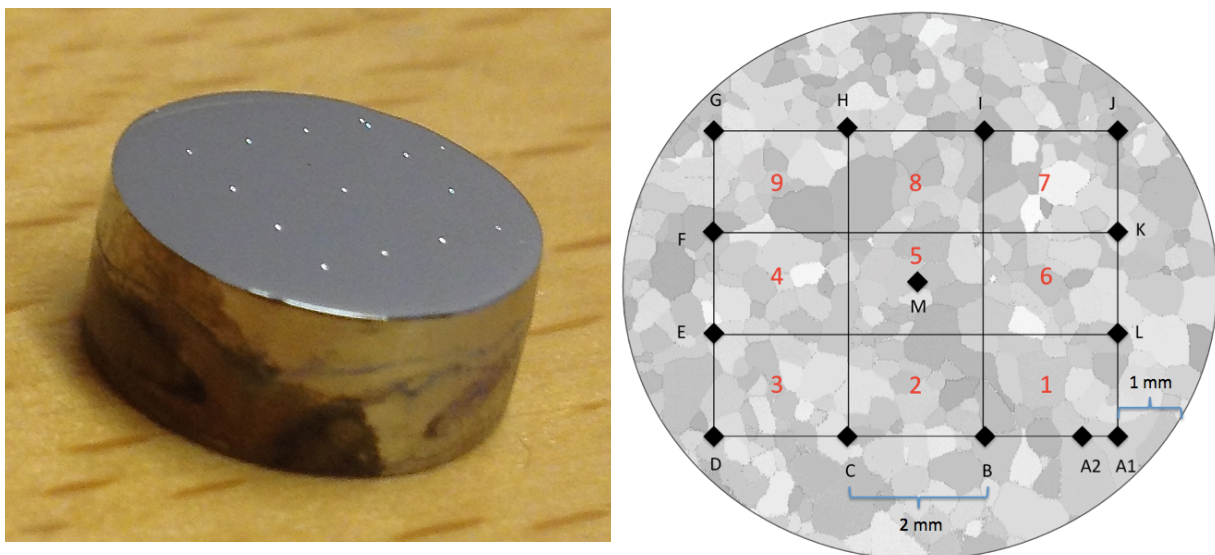


**Figure 28: Iron sample after microindentations. (b) Schematic illustration of the sample surface after locating 9 areas with microindentations.**

### 3.3. EBSD analysis

An EBSD analysis was necessary to perform in order to obtain information from the crystallographic orientations on the iron sample. The choice of which orientation the pillars are to be made on is important to ensure proper test results.

#### 3.3.1. Surface Scan

The EBSD analysis were performed after a satisfying sample preparation, in order to examining the crystallographic orientation of each grain of the nine different areas located by microindentation. This was conducted by using the SEM Hitachi SU-6600 at Materialteknisk, NTNU. The SEM used is equipped with a Nordif phosphorous screen EBSD detector coupled with a CCD camera and TSL OIM data collection software from EDAX. The SEM was first

calibrated by adjusting beam alignment, choosing an accelerating voltage and focusing on the sample surface. The sample stage was then tilted to 70 ° before the UF-1000 EBSD detector was inserted, which ensure the best backscatter diffraction towards the phosphor screen.

After the located areas were selected, five calibration points and one acquisition point were chosen before the EBSD scan was performed and mapped in a stepwise pattern. The calibration point's function is their reference for the later interpolation and indexing sequence. It is important to choose calibrations points that not contain either zone axis or overlapping patterns at grain boundaries, when such selections can impact the overall quality of the IPF-map. The EBSD data were indexed by the TSL OIM Data Collection 6 and further analyzed by using the OIM Analysis 6.0 software, which enables to create different types of maps to visualize the grains and phases present in the iron sample. Parameters used for the EBSD scans are presented in Table 4.

Table 4: EBSD parameters used with Nordif 1.4. for each scanned area on the iron sample.

Parameter	Value
Working distance	25.5 mm
Tilt angle	70°
Magnification	50X
Accelerating voltage	20 kV
Acquisition frame rate	830 fps
Acquisition resolution	96 x 96 px
Acquisition exposure time	1154 μs
Acquisition gain	7
Calibration frame rate	160 fps
Calibration resolution	240 x 240 px
Calibration exposure time	6200 μs
Calibration gain	5
Step size	5 μm
Scan time	00:04:37

### 3.3.2. Crystal Orientation Mapping

The indexed data collected from TSL OIM Data Collection 6, were used to create Orientation Imaging Micrographs (OIM) by the OIM Analysis 6.0 software, making a visual representation of the crystallographic microstructure. This section was performed in order to locate grains with the orientation of interest to fabricate pillars on. The orientations of interest were the single slip planes <235> and <149> and multiple slip system <011>, which were highlighted during the mapping section. The main features in the OIM software that were used were an IPF map and IQ map, with a corresponding pole figure. For every pixel in the IPF map, the crystallographic orientation is determined and colored according to the inverse a pole figure. Each color is representing a crystallographic orientation. For the IQ maps, only the grain orientations of interest were highlighted. The colorscale indicates that darker grains are more likely to have the exact orientation of interest. The misalignment between grain boundaries was restricted to 2°. Such mapping were performed on the nine located and scanned areas, and put together as a final map, shown in Figure 29, that could be used as a navigation reference for pillar fabrication in the focused ion beam, in order to place the pillars in the correct grains with the correct orientations. The indexed crystallographic orientations of the grains were evaluated in order to pick grains that had a detected plane  $[hkl]$ , normal to the

sample surface. In total 3 orientations with loading axis of  $\langle 149 \rangle$ ,  $\langle 235 \rangle$  and  $\langle 011 \rangle$  were selected and used for further productions and testing of the micropillars, shown in Figure 29 within the highlighted red square.

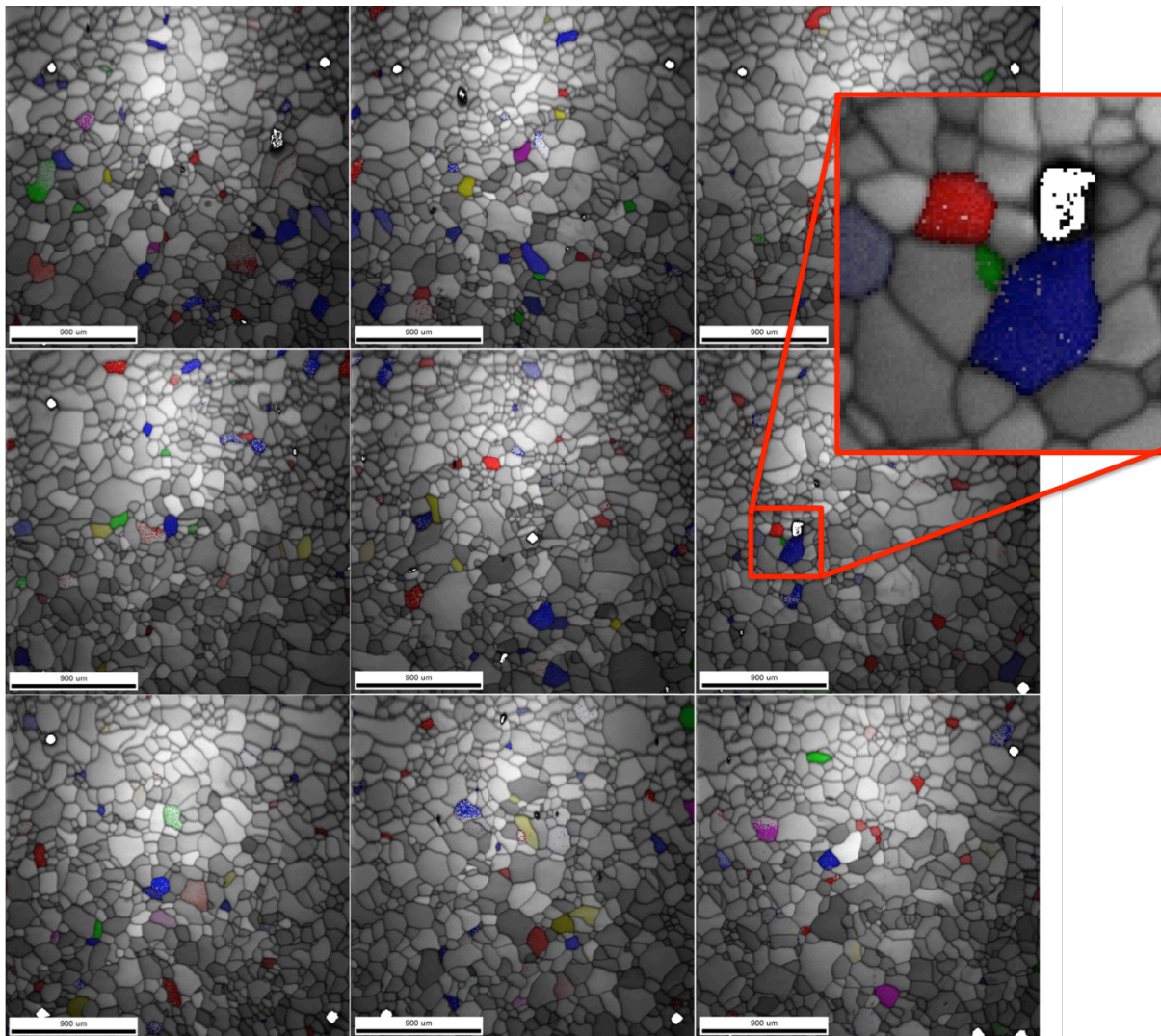


Figure 29: EBSD map with highlighted grains of interest, where the red grain represent  $\langle 235 \rangle$  orientation, green grain represent  $\langle 011 \rangle$  orientation and the blue grain represent  $\langle 149 \rangle$  orientation.

### 3.4. Cooling system set-up

Extensive work has been put into designing and constructing a cooling system in order to perform in-situ experiment with a picoindenter interfaced with a SEM, at low temperatures. The developed cooling system consists of a liquid nitrogen tank mounted on an SEM port, and further connected to the sample via a coldfinger. It is essential that the coldfinger have good thermal conductivity between all components in order to achieve temperatures relatable to arctic environments. The thermal conductivity for the materials used for the coldfinger are presented in Table 5. Another SEM port is used for temperature measurements. The port has a feedthrough so that the temperature measuring instrument is connected to the sample via thermocouples. An additional SEM port is reserved for the electrical connection from the picoindenter. The above described set-up is schematically shown in Figure 30. The available space in the SEM chamber is restricted, and consists of fragile and expensive parts. When

designing the set-up it was extremely important to consider the limited space, and to ensure safe handling of both the picoindenter and the SEM.

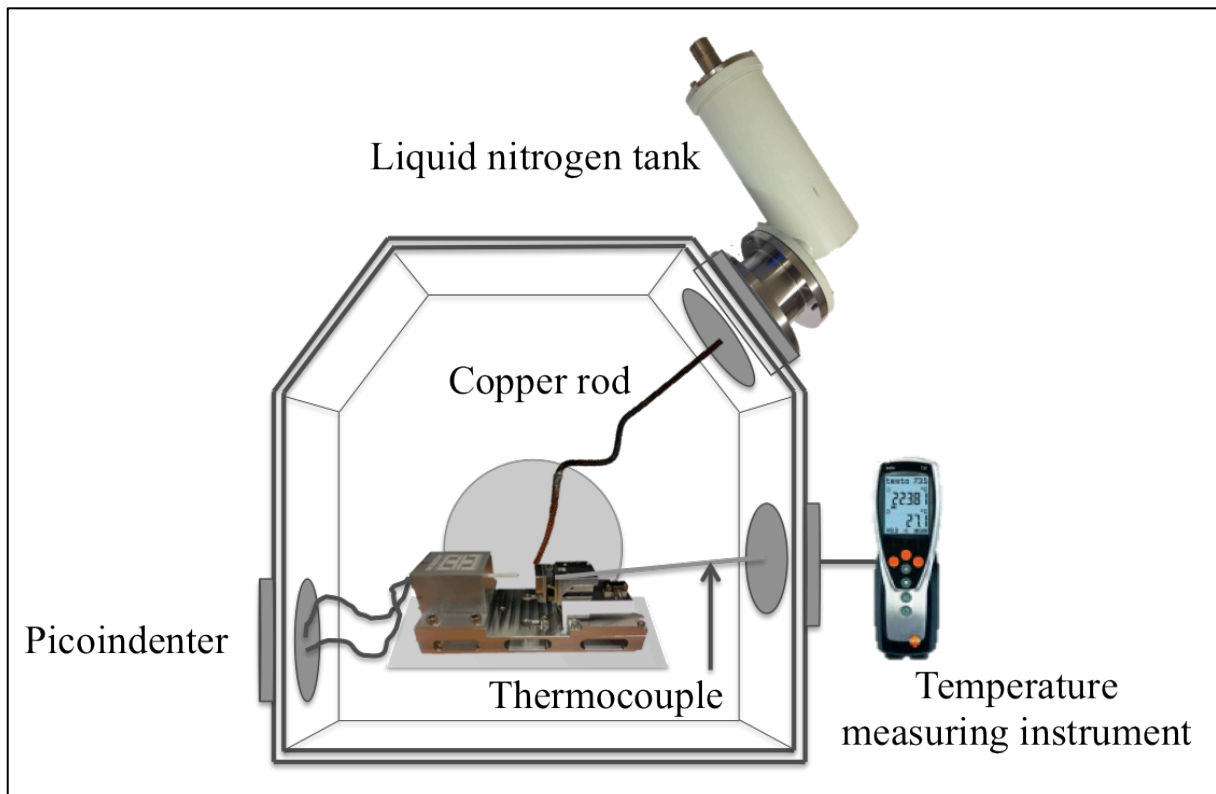


Figure 30: Schematic illustration of the cooling system.

Table 5: Thermal conductivity values for the materials used in the cooling system.

Material	Copper, Cu	Silver, Ag	Brass
Thermal conductivity [W/mK]	385	419	233* (*Depending on alloying elements)

The cooling source to the system was liquid nitrogen kept in a liquid nitrogen tank. In order to connect the tank to the SEM port, it was necessary to machine a new flange with correct dimensions relative to the nitrogen tank and the SEM port. Accurate measurements were made, and the flange was machined at the finemechanical workshop at NTNU. The resulting solution is shown in Figure 31 (a), where the liquid nitrogen tank is connected to one of the SEM ports via the new flange.

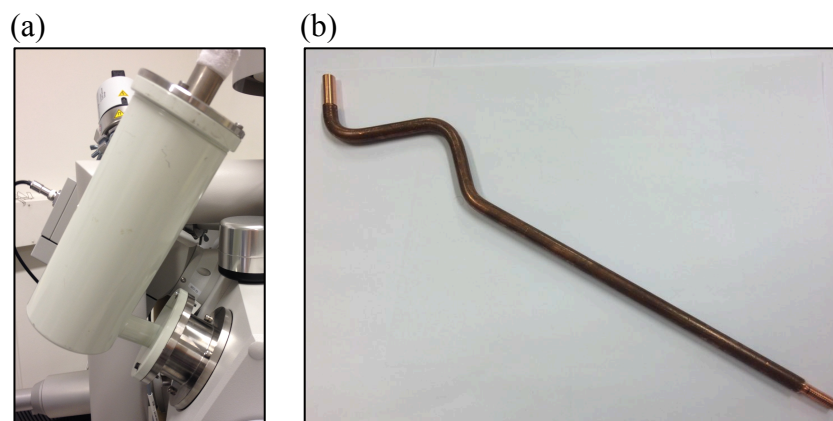


Figure 31: (a) Liquid nitrogen tank with connecting flange. (b) Copper rod with correct dimensions for SEM.



The cooling from the liquid nitrogen tank to the sample was transferred via a solid copper rod that was machined at the mechanical workshop at NTNU, and shown in Figure 31 (b). The dimensions and angles of this rod had to be precisely in order to safely operate the SEM without touching other already existing components (detectors, cables, etc.) in the limited space in the vacuum chamber. To make sure that the right dimension was obtained, a flexible steel wire was used, placed inside the vacuum chamber and bended with proper angels and lengths with respect to the components and parts inside the SEM chamber. This wire was further used as a template for the production of the final solid copper rod.

The copper rod had to be screwed in the tank prior to attaching the rod to the liquid nitrogen tank. The liquid nitrogen is not in direct contact with the copper rod, but there is a mechanical contact between the nitrogen container and the copper rod, cooling down the rod. Due to the limited space in the SEM chamber, it was not possible to screw the rod when the tank was already mounted on the SEM port hence this had to be done initially.

During the experimental testing, small movements of the SEM stage and the picoindenter stage are necessary in order to locate the sample area of interest. Hence the component connecting the stiff copper rod to the sample had to be flexible. Additionally, this flexible connection had to be sufficiently massive in order to obtain the thermal conductivity through the system. The final solution was a copper stocking, consisting of several entwined copper threads, shown in Figure 32 (b). Continuously, the copper stocking was soldered to a small copper plate, where the sample stub/holder were directly placed. This copper plate was necessary to use, in order to obtain a high contact areal between the parts, hence a better thermal conductivity through the system.

Due to the fact that the rod had to be screwed in the tank before further mounting could continue, the connection between the flexible copper stocking and the solid copper rod had to be detachable. A mechanical connection consisting of a brass clamp turned out to be a practical solution as viewed in Figure 32 (a). The brass clamp was machined with two screws used to squeeze the copper stocking and the copper rod together. The copper stocking was first thread around/over the copper rod, approximately 2mm, and the brass clamp connected over this part. Here, a strong mechanical connection was achieved, and the thermal conductivity was maintained since the copper stocking had a sufficiently contact areal with the copper rod.

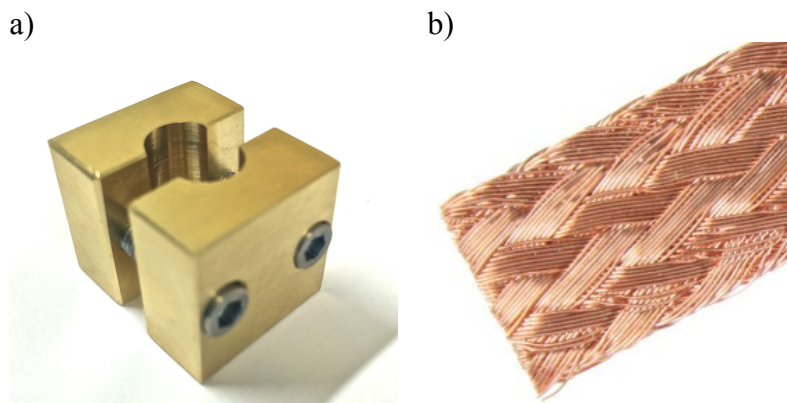


**Figure 32: (a) Brass clamp. (b) Copper stocking consisting of small copper threads entwined together.**

As mentioned above, the other end of the copper stocking was connected to a copper plate. Initially, the intention was to silver solder the copper stocking directly on the copper plate,

which turned out to be a challenge. The copper stocking is very difficult to solder due to the fact that it consists of a large number of very thin copper threads. During silver soldering the operating temperature is very high, in order to make the silver flow before the flux (which is needed to avoid copper from oxidizing at high temperatures) is burned up. Hence, at these high temperatures, the copper threads burn up before they get attached to the copper plate. This problem was solved, using a ferrule, made of brass, as a component between the copper stocking and the copper plate. The end of the copper stocking was twinned together and put inside the ferrule before it was silver soldered. The other end of the ferrule was silver soldered to the copper plate. The final solution of the coldfinger components connected together, is viewed schematically and with photos in Figure 33.

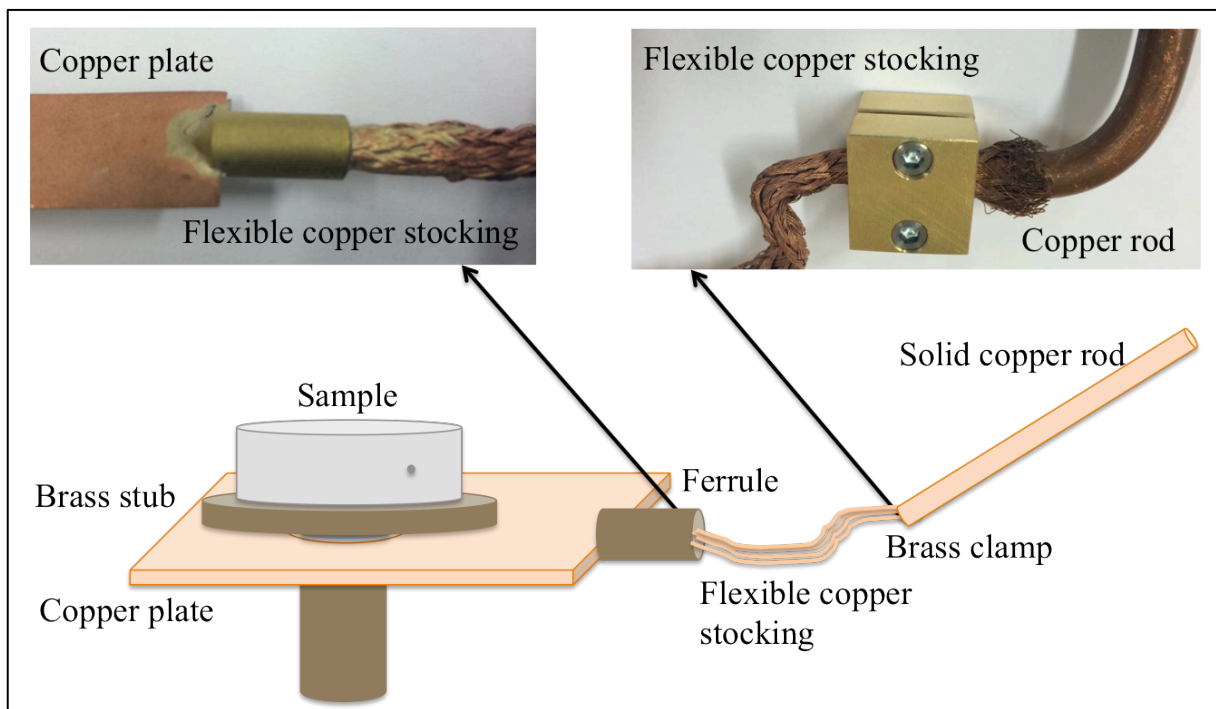


**Figure 33: Schematic illustration of coldfinger components and connections**

In order to mount a sample on the picoindenter stage, it is necessary to use compatible sample stubs, which is usually aluminum stubs. Normally, samples are attached to the stubs by a carbon tape. In this case, the thermal conductivity is essential thereby the carbon tape was replaced with a fast drying silver paint (59% silver solids). However, the connection between the sample and the stub experienced some force when the coldfinger set-up was mounted, and the sample was detached from the stub. Hence the solution was excluded due to the poor adhesion. Another option considered was a silver paste with 72% silver solids (SPI Silver Paste Plus), which is very ideal for SEM use and high conductivity at cryogenic temperatures, and was successfully used in this experiment as well. However, it should be noted that the strength of the silver paste is not the greatest, but sufficient in this case with carefully handling.

Furthermore, the sample stub had to be attached properly to the copper plate. Initially, we intended to silver solder the aluminum stub to the copper plate. However, soldering silver to aluminum turned out to be very tricky because the metals have different soldering temperatures. Additionally, during heating of aluminum, an oxide layer is formed, that has poor bonding to copper. Therefore, a new sample stub had to be made with another material

and the choice fell on brass since it proved to respond well to silver soldering. The new brass stub where machined at the fine mechanical workshop at NTNU. The shaft on the stub was machined sufficiently long so that there would be a gap of air between the copper plate and the picoindenter stage when the sample is mounted as shown in Figure 34. By doing this, the copper plate will not come in contact with the picoindenterstage, hence a smaller contact area is obtained. This will result in a reduced cold loss from the sample holder and the sample to the picoindenter stage, which is beneficial for the cooling of the sample.

Another important part of the set-up procedure is the mounting of the sample relative to the picoindenter probe. After attaching the sample to the stage, the indenter tip must be approached extremely close to the sample surface (approximately 1-2 mm). This is a sensitive approach and need to be conducted with care and accuracy; hence this must be done before the picoindenter is mounted inside the SEM vacuum chamber. If the indenter probe touches the sample surface, one can risk damaging important areas on the sample surface reserved for the experimental testing. The approached distance between the sample surface and indenter probe is illustrated in Figure 35. One last concern, related to the picoindenter, was the flange with the electrical connections for the picoindenter. The already existing flange had four screw holes, which were not compatible with the SEM port. The SEM port reserved for the picoindenter flange, consisted of three screw holes. Hence, the correct dimensions between the wholes on the SEM port were measured, and the fine mechanical workshop at NTNU machined three new holes on the flange that corresponded precisely to the ones on the port as shown in Figure.

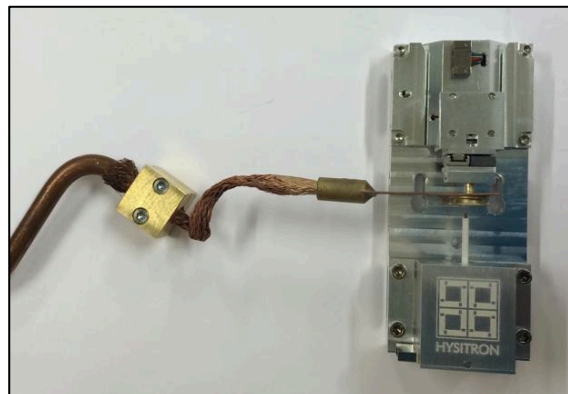


Figure 34: Sample mounted on picoindenter stage.

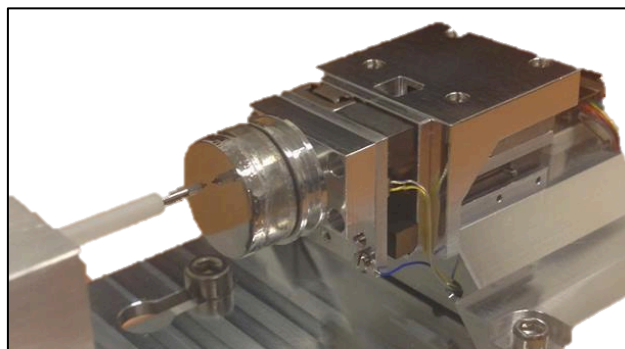


Figure 35: Tip to sample surface distance.

In order to be able to measure the sample temperature during cooling, a mantle element had to be connected to the sample in a proper way. Initially, it was decided to use silver paste to connect the thermocouple on the side of the sample. However, since the sample is curved and smooth with a diameter of 1mm, it was difficult to achieve a solid and strong connection between these parts. The optimal solution conducted was do drill a small hole the sampleside,

with a diameter of 0,6mm and a depth of approximately 3mm, that fitted well to the thermocouple (with a diameter of 0,5mm). In order to confirm that the connection between the thermocouple and the sample was tight enough and the temperature measurements were reliable, another thermocouple was silver soldered to the copper plate. The measured values were in good agreement. Furthermore, the thermocouples had to be connected to a temperature-measuring instrument via a thermocouple extension and compensation cable (TC cable), seen in Figure 37, hence a flange with a vacuum compatible feedthrough part for the TC cables, were machined at the fine mechanical workshop at NTNU and shown in Figure 36 (a). In good agreement with Max Sievert AS and the fine mechanical workshop, a Teflon plug was used for the feedthrough solution. The Teflon plug is fairly soft and when the chamber is pumped to vacuum, the vacuum will pull the plug inn and seal the output. It was important that the TC cables were round in order to obtain a maximum sealed feedthrough. To make sure the solution didn't leak and the pressure were increasing, the flange were mounted on the SEM for three days where the pressure where continuously checked. All components and flanges used for the cooling system proved to be successful, and the experiments could safely be conducted. The technical data of the temperature measuring instrument, thermocouples and the TC cables are presented in Table 6.

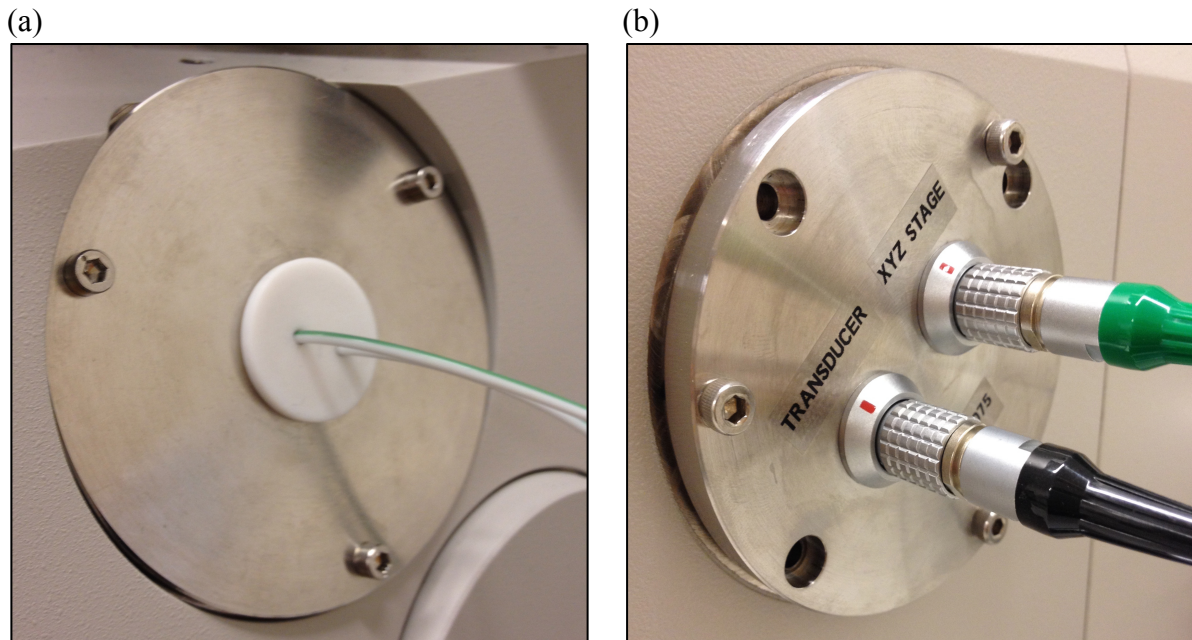


Figure 36: SEM flanges for (a) temperature measurements and (a) picoindenter electrical connections.

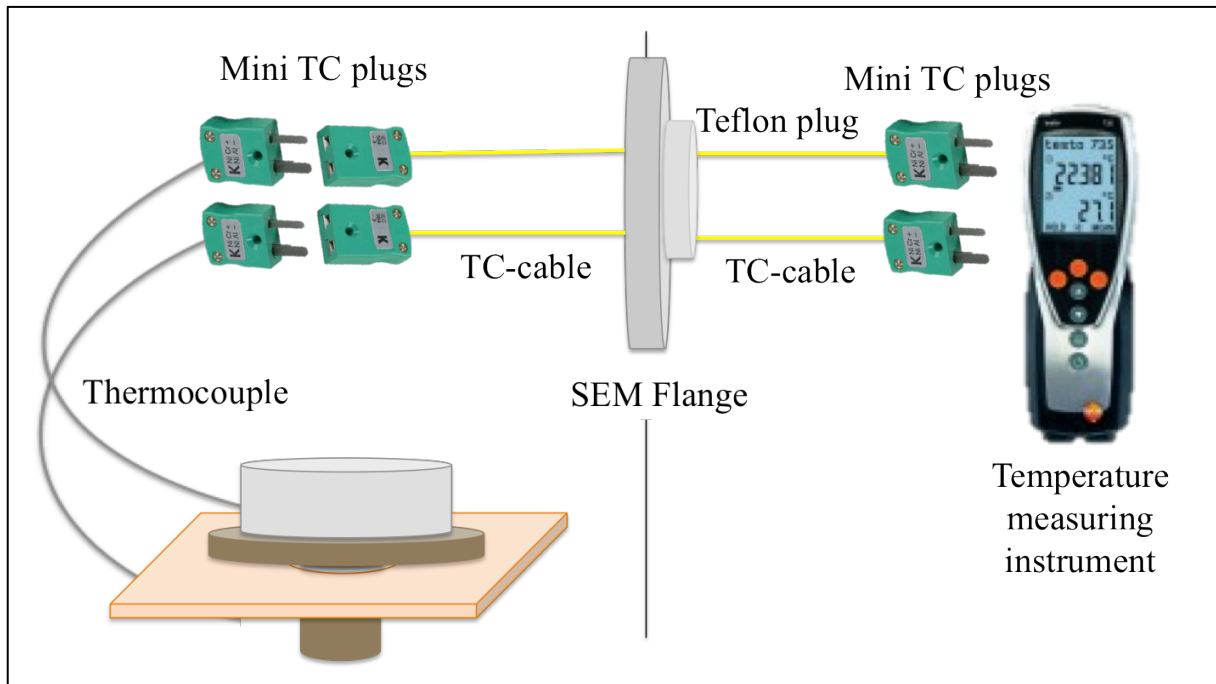


Figure 37: Schematic illustration of temperature feedthrough.

Table 6: Technical data for TC cable, temperature measuring instrument and thermocouple, provided from Max Sievert AS.

Component	Type	Diameter [mm]	Length [mm]	Measuring area [C°]	Accuracy [C°]
Thermocouple extension and compensating cable (TC cable)	B13 with Teflon insulation single pairs, round wire	2mm	500	-75→250	
Thermocouple	K-element, Cr-CrNi with miniatur tc miniplugs	0,5	500	-180→1350	
Temperature measuring instrument	Testo 735-1, with two inputs for fast thermocouple probes			-200→1370	0,05

With the current set-up it is not possible to control the temperature. The liquid nitrogen has a constant temperature (77K) and will continue to cool the sample until it stabilizes at a minimum; consequently additional heating is necessary in order to precisely control the sample temperature. The thermal conductivity of the coldfinger proved to be sufficient; after approximately 1,5h a temperature of -90C was reached. Precautions were taken during the installation and handling of the equipment, and all the experiments were safely conducted. Figure 38 images the SEM chamber with all components installed.

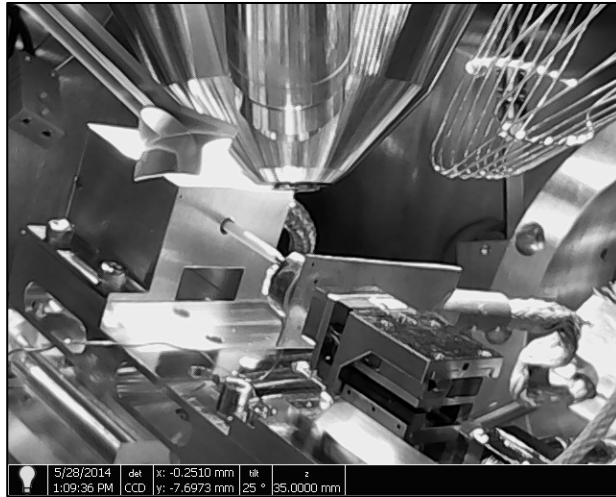


Figure 38: Image of SEM chamber with all components installed.

### 3.5. Pillar fabrication

Further experimental work continued with fabrication of pillars using the FEI Helios 600 DualBeam FIB/SEM at NTNU Nanolab shown in Figure 39 (a). The intent was to find orientations of interest as close to each other as possible. Which is an advantage when the compression testing starts. The stage movement of the picoindenter probe, have a limited movement of only 1mm in each direction after the stage is centered, which make the location of the sample relative to the probetip, very important. The Fe sample was attached on a FIB stub, using a carbon tape, which maintains the conductivity through the sample. The FIB stub with the connected sample was mounted on a standard sample holder provided by FIB, before it was inserted into the chamber. The sample holders restrict the sample to a height smaller than about 1,9 mm, but since the Fe sample was about 5 mm height, the sample holder was turned upside down, in order to lower the total height of the sample system as showed in Figure 39 (b).

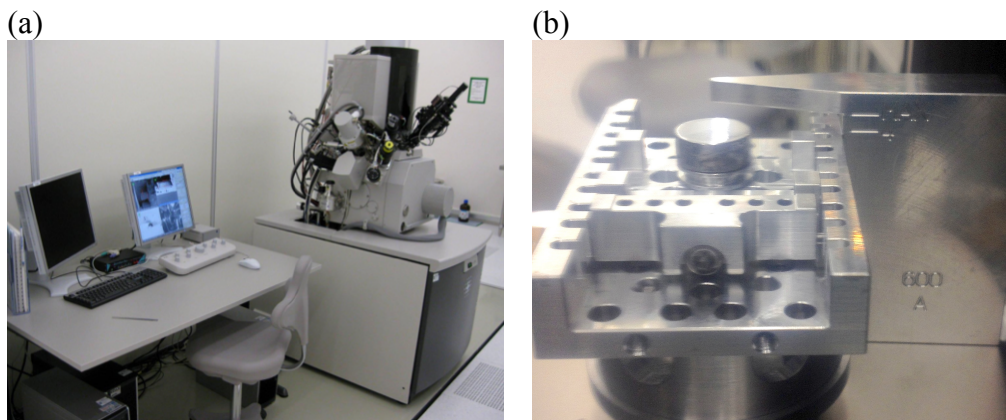


Figure 39: (a) FEI Helios 600 DualBeam FIB/SEM from NTNU Nanolab. (b) Sample mounted on the stage in the vacuum chamber.

The pillars were manufactured mainly in a two-step procedure with an acceleration voltage of 30 kV, followed by two extra milling steps in order to reduce the tapering angle ( $\alpha$ ), of the pillar. The first step uses a circular milling pattern to mill out an array of iron stumps at a high  $\text{Ga}^+$  current (approximately 6,5nA) inside the grains of interest. The second step follows the same procedure only with a reduced current (90pA), in order to reduce the material re-

deposition and surface refining so that a well-defined pillar shape is obtained. The parameters used for the chosen grain orientations  $\langle 235 \rangle$ ,  $\langle 149 \rangle$  and  $\langle 011 \rangle$  are introduced in Table 7, and resulted in pillars with a diameter of approximately  $1\mu\text{m}$ , a  $h/d_t$ -ratio (the ratio between the pillar height ( $h$ ), and the diameter at the top ( $d_t$ ) of the pillar) of 3.5 and a  $\alpha$  of approximately  $4^\circ$ . Figure 40(a-d) shows SEM micrographs of one representative pillar from the  $\langle 235 \rangle$  oriented grain, after the four milling steps. Pillars with diameter of  $1\mu\text{m}$  were desired in this investigation. At this size it is easier to identify slip traces on the pillar surface, compared to smaller pillars. Additionally, since the results obtained in this thesis were to be compared with experimental results from B.R.S. Rogne and C. Thaulows's work [2, 24], where pillars were of similar sizes, this was an important factor. In total it was produced 16 pillars distributed in three different grains with the three different grain orientations;  $\langle 235 \rangle$ ,  $\langle 110 \rangle$  and  $\langle 111 \rangle$

**Table 7: Parameters used for the different steps during FIB milling.**

	Step 1	Step 2	Step 3	Step 4
<b>Orientation <math>\langle 235 \rangle</math></b>				
Outer diameter [ $\mu\text{m}$ ]	13	6	2	1.7
Inner diameter [ $\mu\text{m}$ ]	4	1.5	1.2	1.2
z [ $\mu\text{m}$ ]	0.5	0.5	0.1	0.1
Current	2.7nA	90pA	26pA	26pA
Time per pillar	02:32	16:23	00:50	00:32
Number of pillars	31	8	8	8
<b>Orientation <math>\langle 149 \rangle</math></b>				
Outer diameter [ $\mu\text{m}$ ]	13	6	2.13	1.9
Inner diameter [ $\mu\text{m}$ ]	4	1.5	1.2	1.2
z [ $\mu\text{m}$ ]	0.5	0.5	0.1	0.1
Current	2.7nA	90pA	26pA	26pA
Time per pillar [min]	02:32	16:23	01:00	00:40
Number of pillars	6	6	6	6
<b>Orientation <math>\langle 011 \rangle</math></b>				
Outer diameter [ $\mu\text{m}$ ]	13	6	6	1.9
Inner diameter [ $\mu\text{m}$ ]	4	1.5	1.2	1.2
z [ $\mu\text{m}$ ]	0.5	1	1.5	1
Current	0.90nA	0.44nA	0.44nA	26pA
Time per pillar [min]	51:53	07:00	13:00	05:00
Number of pillars	7	2	2	2

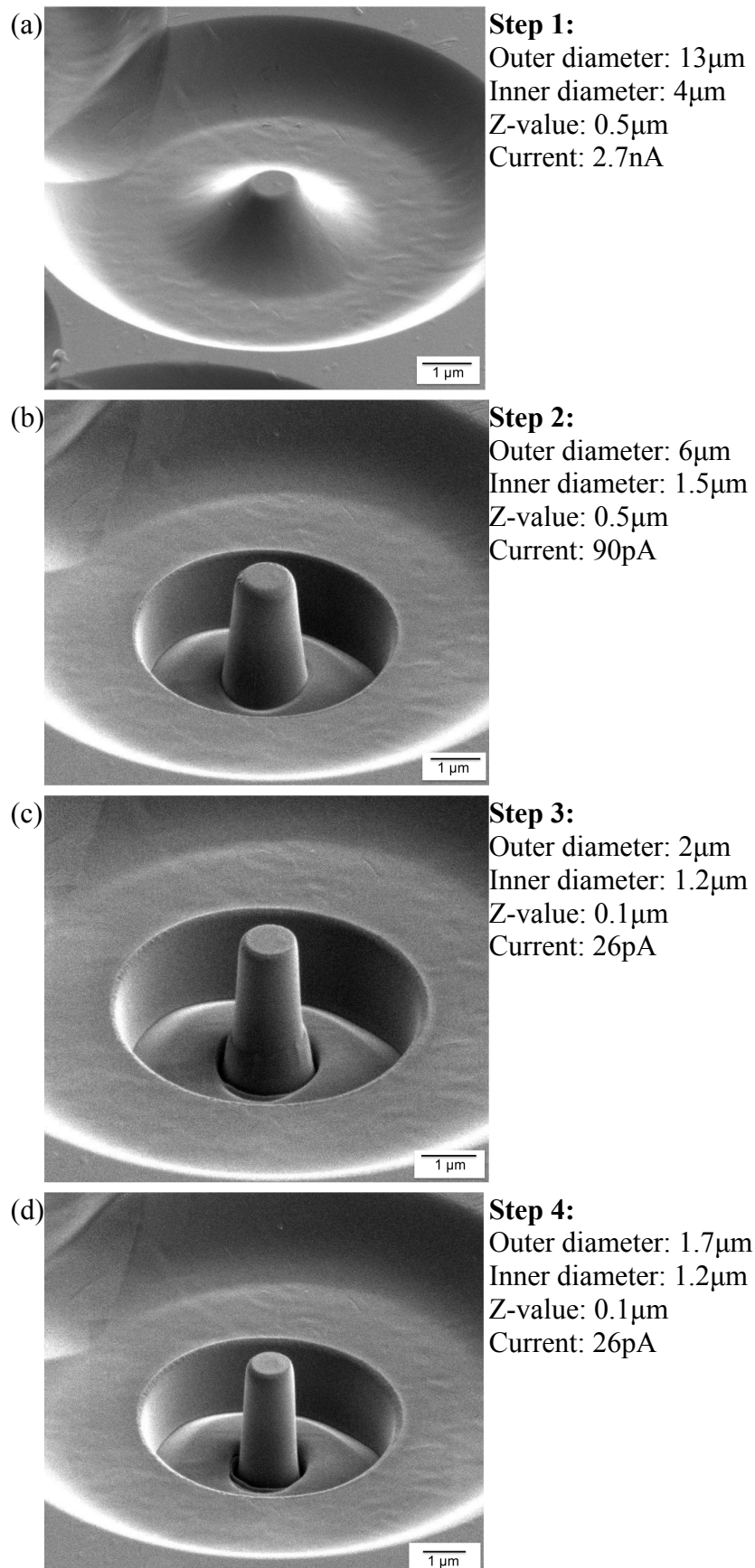


Figure 40: SEM micrographs of pillar fabrication, showing the resulting geometry after (a) step one, (b) step two, (c) step three and (d) step four, with the corresponding parameters used.



### 3.6. In-situ pillar compression

After pillar fabrication, the Fe sample was transferred to a Hysitron PI 85 PicoIndenter supplied with a TriboScan software, in the Nanomechanical Lab at IPM NTNU. The picoindenter was connected to the coldfinger set-up inside the SEM vacuum chamber. Before loading, the SEM chamber was pumped to vacuum, and liquid nitrogen was poured into the liquid nitrogen tank that was connected to the coldfinger inside the vacuum chamber. The sample was cooled down continuously until the temperature stabilized at  $-90^{\circ}\text{C}$ , after approximately 90 minutes. As mentioned, the picoindenter probe has a limited movement in x/y- direction, which is approximately mm in each direction, hence the picoindenter stage where the sample is mounted on, were manually moved in order to locate the grains of interest as close to the tip as possible.

As a result of large temperature differences between the indenter tip and the sample, it was suspected that this could cause unstable results in terms of drift. Hence, several single indentations were performed, with and without drift corrections in order to consider the influence of temperature on the drift rates. A more detailed description of this procedure is presented in section 4.2. under Results and Discussion. Since the single indentation tests revealed some drift at low temperature, it was performed a single indent with an extended loading segment, in order to cool down the tip, before compression of each pillar. The pillars were compressed with a cube corner probe with a diameter of  $40\mu\text{m}$  and a cone angle of  $60^{\circ}$ . The experiments were performed in an open-loop load control mode while simultaneously acquiring a SEM video and the load-displacement curves.

Approaching the indenter probe to the pillar surface was a challenge, considering that the tilt mode makes it difficult to define visually the location of the probe tip relative to the pillar top-surface. Additionally, as a result of the large size differences between the probe and the pillars with a diameter of  $1\mu\text{m}$ , some misalignment can occur, illustrated in Figure 41. Approaching the pillar surface where proceeded as follows; the probe was moved stepwise towards the pillar crater until the shadow of the tip was visible at the crater edge, followed by an automated approach with the parameters presented Table 8. Since the diameter of the craters was  $13\mu\text{m}$ , the tip was moved  $7.5\mu\text{m}$  from the edge of the crater, towards the pillar axis in the center of the crater. By conducting these simple estimations, the tip should be centered above the pillar. An additionally approach were conducted at the pillar top-surface, before loading. The important loading parameters used for pillar compression are presented in Table 9. One pillar was used as a test pillar to observe degree the deformation to different peak loads and loading rates. In this experiment, large geometrical changes of the pillar was not desirable, since the slip traces on the pillar surface were to be analyzed after compression.

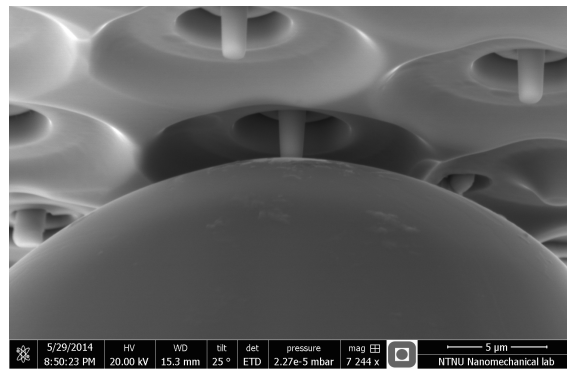


Figure 41: SEM micrograph showing the large size difference between the cube corner probe ( $d=40\mu\text{m}$ ) and the pillars ( $d=1\mu\text{m}$ ).

**Table 8: Parameters used during tip to sample surface approach.**

Approach step size [nm]	25
Approach velocity [nm/s]	50
Approach Threshold [ $\mu\text{N}$ ]	100
Backoff distance [nm]	50

**Table 9: Important parameters used during pillar compression.**

Q-gain	Peak force [ $\mu\text{N}$ ]	Loading rate [ $\mu\text{N/s}$ ]
0,08	5000	250

### 3.7. Slip trace analysis

The slip traces of crystallographic slip on the pillar surface were compared with slip traces that were calculated based on the EBSD scans. The calculations were performed in a MatLab script developed by PhD candidate Bjørn Rune Sørås Rogne. The slip systems considered in the analysis were  $\{110\}\langle 111\rangle$  and  $\{112\}\langle 111\rangle$ , with the selected grain orientations  $\langle 235\rangle$  and  $\langle 149\rangle$ . As initial conditions the slip plane normal for the two families of planes are defined together with the unit cube and transformed into the grain orientations. The rotation transformation matrix uses the Euler angles, of type Bunge from the grain orientations to rotate the vectors. These Euler angles were registered from the EBSD scan with the grains of interest. The z-coordinate of the transformed planes were calculated by sweeping along a circle in the z-plane, or the cylinder surface, to form an elliptic intersection.

The stage rotation and the tilting registered from the EBSD scan were used as a reference position. During SEM imaging of the compressed pillars, the stage rotation and tilting from the reference position were used. The pillars were imaged from four angles with  $90^\circ$  between each angle. Each angle were registered with respect to the reference angle and used to define the camera view of the 3D plot. The resulting plot is viewed in Figure 42 and includes the most favorable, in terms of Schmid factor, slip traces for one particular direction. After the plot is obtained, it is fitted to the pillar diameter on a SEM image of a representative pillar. Slip traces observed on the pillar surfaces are approached to the calculated slip systems to see if there is a match in some of the slip systems. Since the pillars in this experiment were deformed to only a few percent strains, it was possible to identify some of the slip traces on the pillar surface.

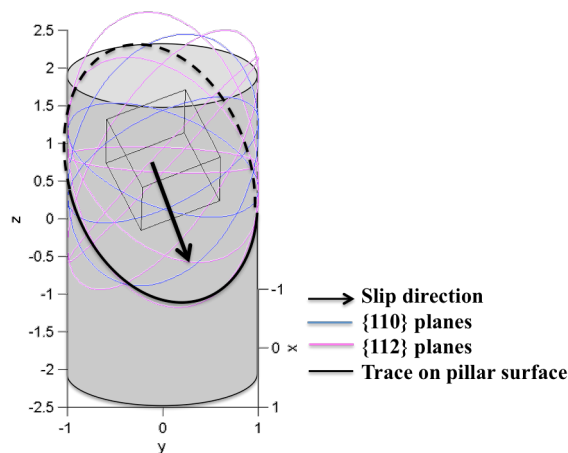


**Figure 42: Illustration of calculated slip traces along one direction on the surface of a cylindrical pillar.**

## 4. Results and discussion

The results obtained in this thesis are presented together with discussion related to theoretical aspects from the literature and the Theoretical Background. Figures and necessary data are given to increase the understanding and the scope of the evaluated results.

### 4.1. Pillar Fabrication

The pillars fabricated in this investigation obtained a top diameter of approximately  $1\mu\text{m}$ , an  $h/d_t$ - ratio of 3.5 and a tapering angle of  $4^\circ$ . The resulting dimensions of all FIB fabricated pillars are introduced in Appendix A. Figure 43 gives an overview of the pillar distributed in the  $\langle 149 \rangle$  oriented grain. In total, 16 pillars were produced within the three different orientations;  $\langle 235 \rangle$ ,  $\langle 149 \rangle$  and  $\langle 011 \rangle$ . Figure 44 (a-c) shows one pillar representing each orientation.

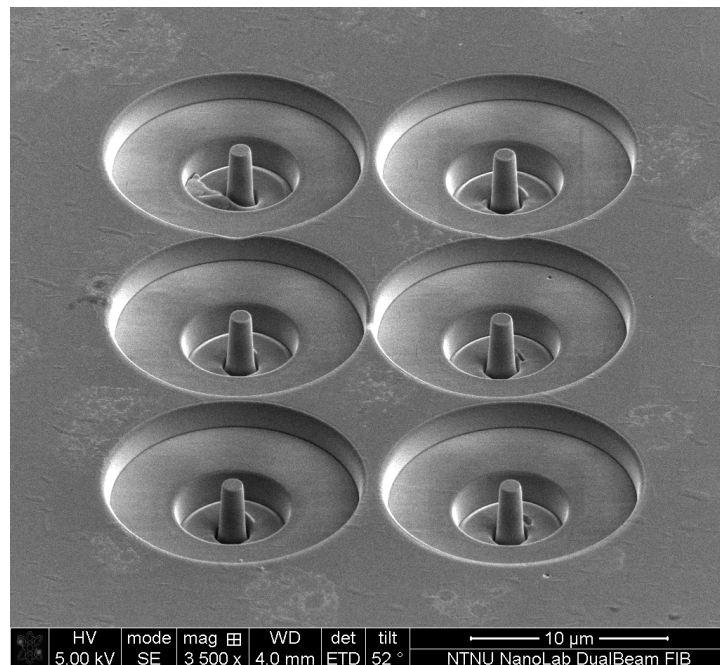


Figure 43: SEM micrograph of pillars fabricated from the  $\langle 149 \rangle$  oriented grain.

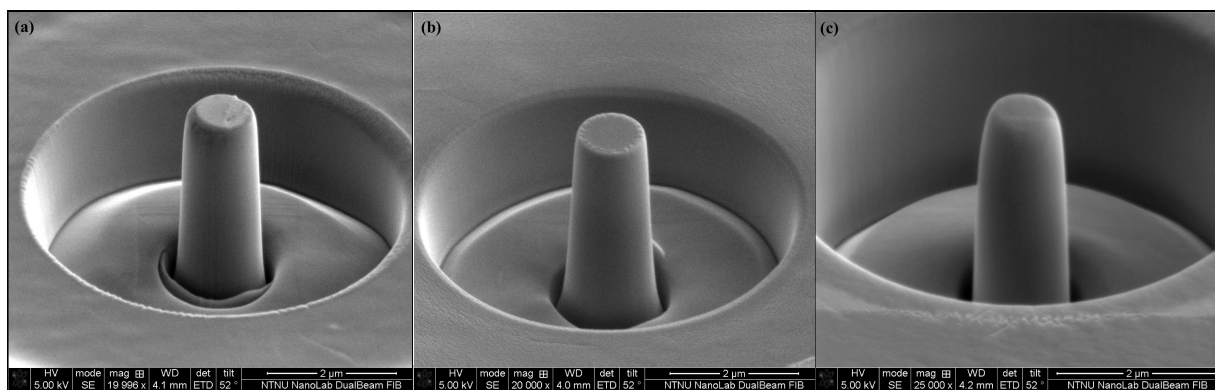


Figure 44: SEM micrographs of FIB fabricated pillars ( $d=1\mu\text{m}$ ) with orientations (a)  $\langle 235 \rangle$ , (b)  $\langle 149 \rangle$  and (c)  $\langle 110 \rangle$ .

Pillars fabricated in the two single slip orientations  $\langle 235 \rangle$  and  $\langle 149 \rangle$ , were produced with similar milling parameters, and approximately equivalent dimensions were obtained. For the multiple-slip orientation  $\langle 011 \rangle$ , a lower sputtering yield was experienced during milling,

hence, the parameters needed to be adjusted to obtain desired dimensions. However, the resulting pillars in this orientation differed from the other ones. As a result of lowering sputtering yield, the pillar stub produced after the first milling step, was significantly lower than in the other orientations. Hence, during the following milling steps, it was used a higher z-value, in order to obtain a similar height as the other pillars. This resulted in a significantly higher depth of the crater surrounding the pillar, also seen in Figure 44 (c).

## 4.2. Drift analysis

The drift correction performed automatically by the picoindenter system includes a lift height parameter. The tip approaches the surface and the lift height withdraws the probe (10 nm - 2  $\mu\text{m}$ ) from the sample surface, then a drift correction is performed before the test begins. Figure 45 represent the load-displacement curve with the automatic drift control. The red curves are for the indents performed at room temperature, while the blue curves represent indents performed at low temperature (-88°C). During the holding segment the force is constant, ideally if there is no drift present, there should not be any displacement during this time. For the indents performed at room temperature, minor drift values are displayed, as expected. This is seen from the short horizontal displacement at the constant force around 3600mN. However, the indentations performed at low temperature display significantly larger drift values, as seen by the long horizontal displacement at the constant force around 3600mN.

In order to confirm that the automated drift correction is reliable, the force-displacement curves without drift correction was plotted. Figure 46 indicates that the automated drift correction for the indentation performed at room temperature was applicable. The displacement during the holding segment is smaller for the curves with automated drift corrections, indicating that the influence of drift is reduced. In contrast the indents performed at low temperatures shows a significantly larger drift with automated drift corrections compared to the curves without drift correction. This indicates that the automated drift corrections at low temperatures are incorrect. Furthermore, a manual drift correction was performed. This was done in order to evaluate why the system calibrates for a wrong drift. The plot is shown in Figure 47, and will be further discussed in the following section.

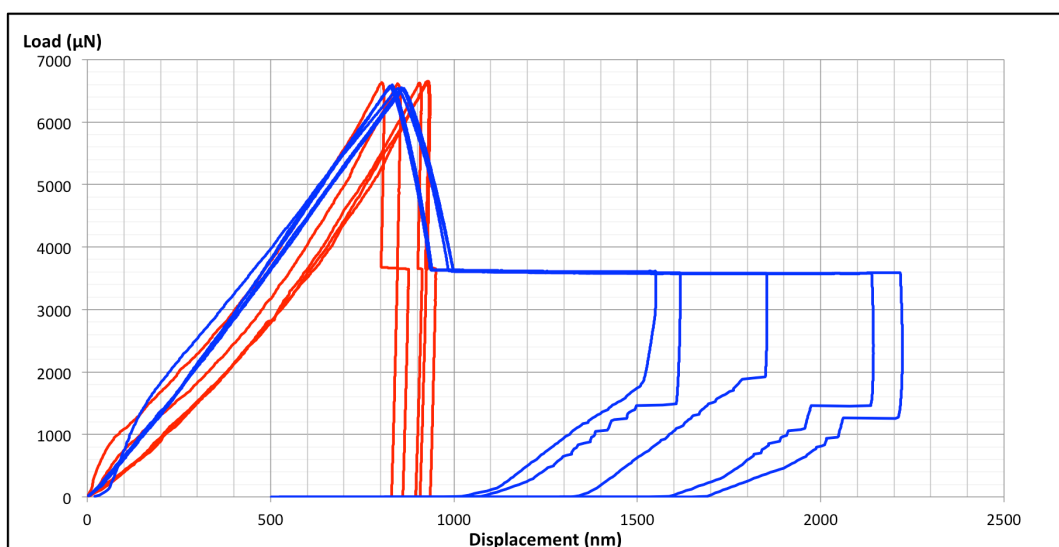


Figure 45: Single indent with holding segment - Automated drift correction.

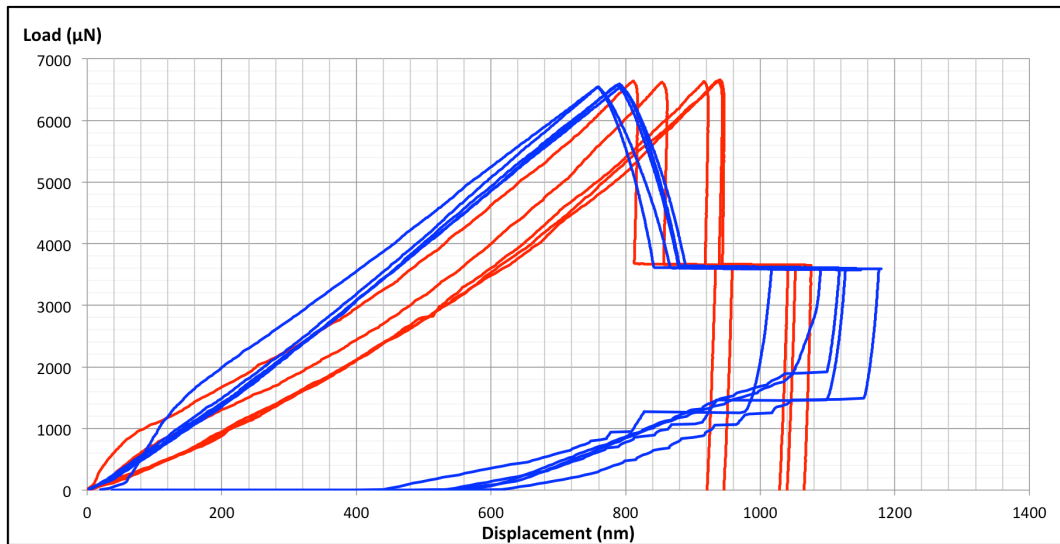


Figure 46: Single indent with holding segment - No drift correction

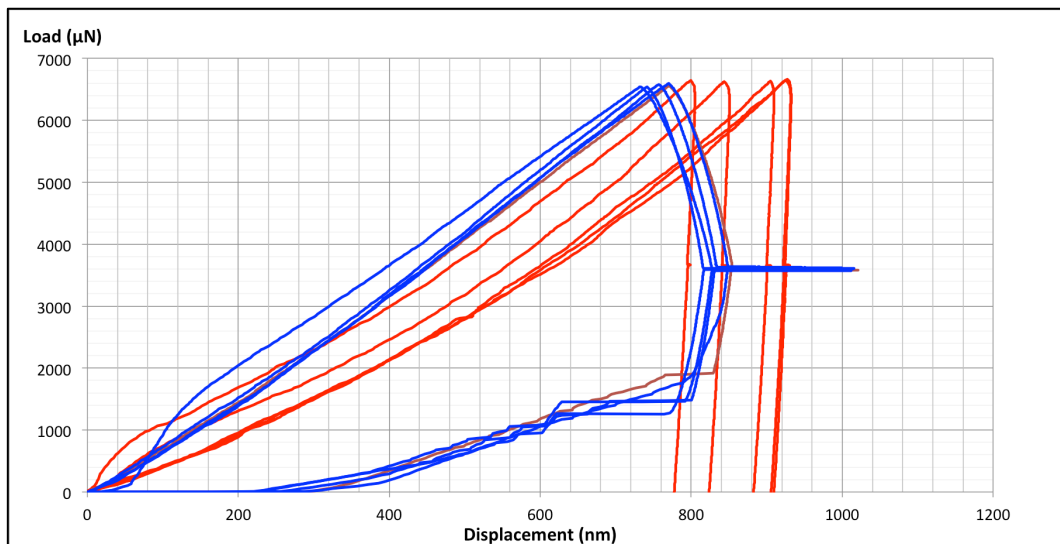


Figure 47: Single indent with holding segment - Manual drift correction

In order to illustrate the effect of the different drift correction, one indentation at room temperature were chosen and the three different drift corrections are displayed in Figure 48. The same was done for one indentation at low temperature, displayed Figure 49. The red curve represents manual drift correction, the blue curve represents no drift correction and the green curve represents automated drift correction. From Figure 48 it is seen that the automated drift correction adjusts the curve correctly, however the manual drift correction is more accurate. From Figure 49, it is seen that the automated drift correction adjusts the curve incorrectly; the drift increases. The drift correction data are presented in Table 10. The values for automated room temperature corrections are roughly similar to the values achieved with manual drift corrections. However, the values for automated low temperature corrections differs from the ones obtained by manual drift correction. The values are negative, while for manual drift correction the values are positive. This explains the increased drift seen in the automated drift correction curve.

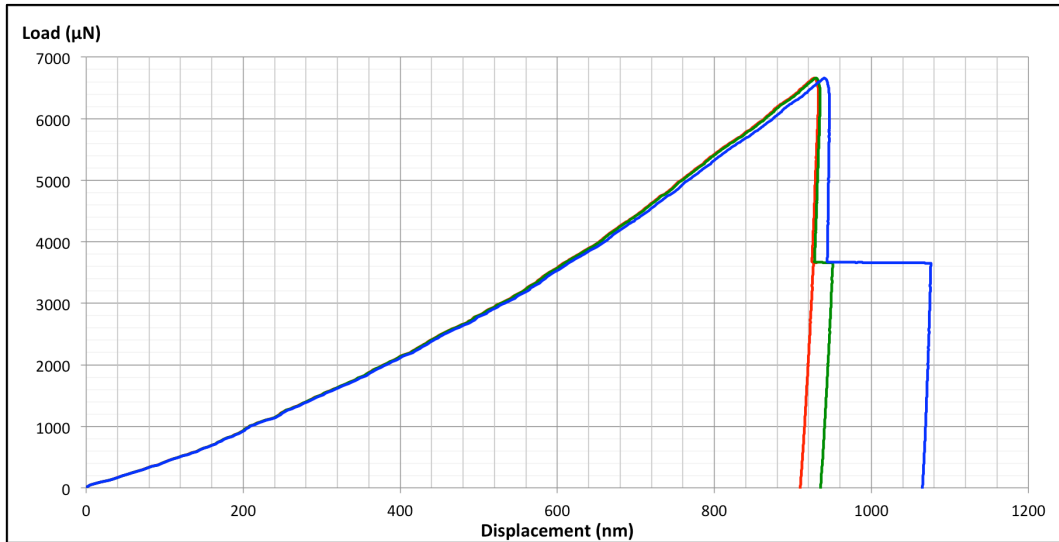


Figure 48: Single indent with holding segment - difference between no drift correction, automated drift correction and manual drift correction - Room temperature

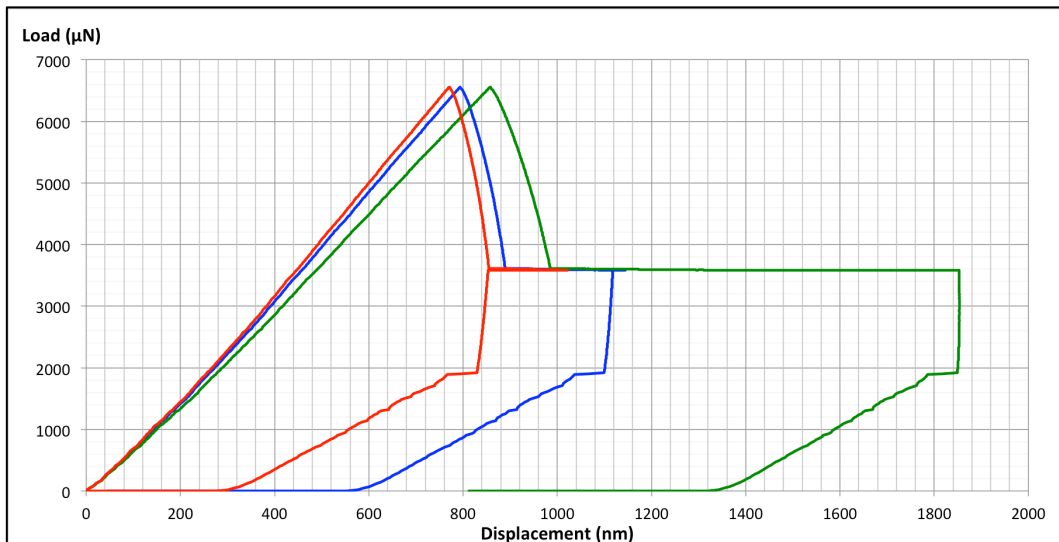


Figure 49: Single indent with holding segment - difference between no drift correction, automated drift correction and manual drift correction - Low temperature

Table 10: Drift correction data.

		Automated drift Correction [nm/s]	No drift Correction [nm/s]	Manual drift Correction [nm/s]
T = 29°C	1	0,5422	0	0,65
	2	0,3811	0	0,6
	3	0,5557	0	0,61
	4	0,5533	0	0,56
	5	0,3563	0	0,51
T = 90°C	1	-3,1923	0	1,15
	2	-5,2144	0	0,87
	3	-4,3992	0	1,3
	4	-1,9156	0	1,5
	5	-2,0035	0	1,05

In order to evaluate why the system automatically corrected with conflicting drift values, the displacement versus time with no drift correction, for the holding segment with constant force, were plotted. Figure 50 shows red curves for room temperature indentations and blue curves for low temperature indentations. At room temperature the figure shows a constant drift for all indentations. At low temperatures, on the other hand, the drift is initially very high and subsequently stabilizes over time. The drift during low temperature indentation is time dependent. It is assumed that this is due to the different temperature gradients experienced by the tip. The curve reaches maximum plateau, followed by drop in drift after some time. The temperature gradient will differ as a result of an initially high temperature difference between the tip and the sample surface; the tip approaching the low sample temperature probably causes the drop in the curves. The trendline estimated for the drift at room temperature, shows that the drift is approximately 0,6nm/s. The low temperature drift trendline was limited to the initially high drift data. This was done in order to evaluate a worst-case scenario for drift effect on bending experiments performed in a short time interval. The drift at the beginning of the indentations at low temperature is approximately 5,2nm/s. All correlating drift evaluations are presented in Appendix E.

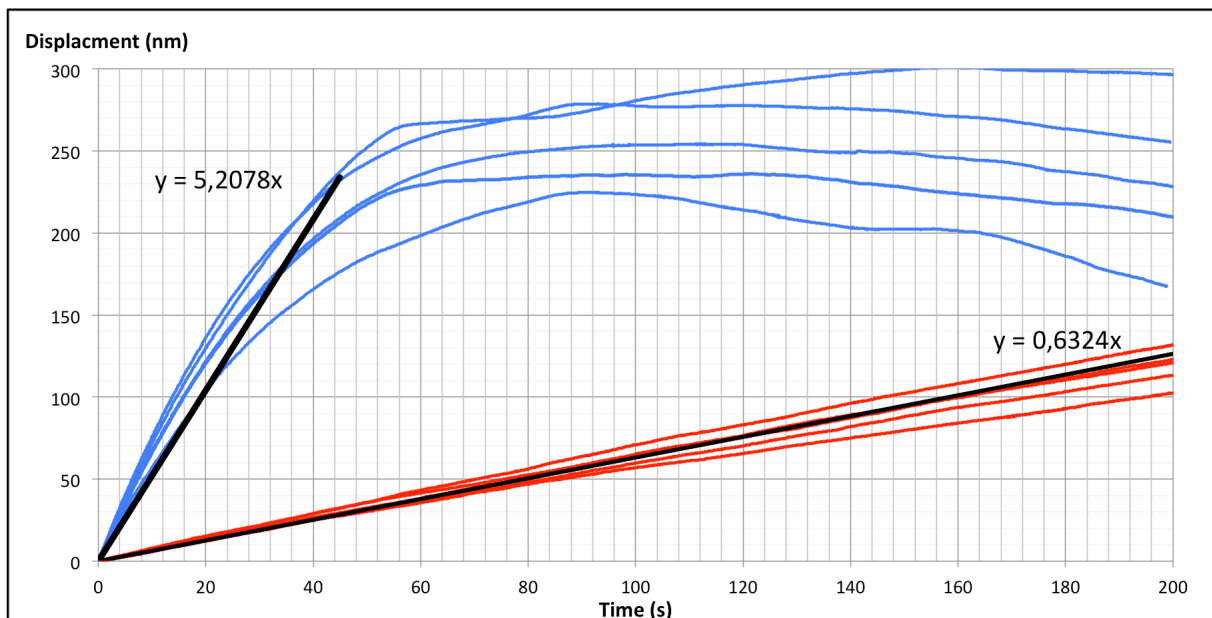


Figure 50 Drift as a function of time for the holding segment with constant force.

### 4.3. Nanocompression in-situ

The pillar compression where performed with a cube corner picoindenter probe, with a radius of 40 $\mu$ m as schematically shown in Figure 51. Before pillar compression it is crucial to accurately position the probe in the center above the pillar, in order to ensure axial loading. Taken into account that the average diameter of the pillars produced in this study were 1 $\mu$ m, the size differences between the probe and the pillars were significantly large. This resulted in challenges in locating the large probe exactly in the center above the pillar. Additionally, the sample stage was tilted to 25°, which made it difficult to visually see the tip of the probe. An illustration of this is shown in Figure 52. A single indent where performed on the sample surface, followed by a sample approach, with a back-off distance of 10nm. After the indentation, the tip was moved in lateral direction until the indent was visible. It was revealed

that the location of the visible indent was approximately  $1,5\mu\text{m}$  from the indenter top visually seen from the current tilt angle of  $25^\circ$ . These considerations, were beneficial when approaching the probe to the pillar surface; when the visually seen top of the probe was located on top of the pillar, the tip needed to be moved further  $1,5\mu\text{m}$  over the pillar, in order to center the probe precisely above the pillar.

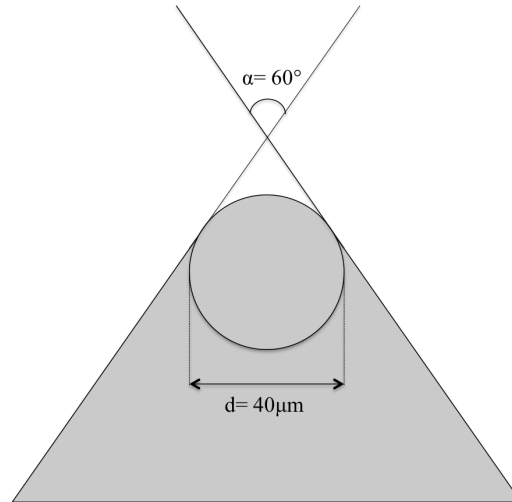


Figure 51: Schematic illustration of the cube corner.

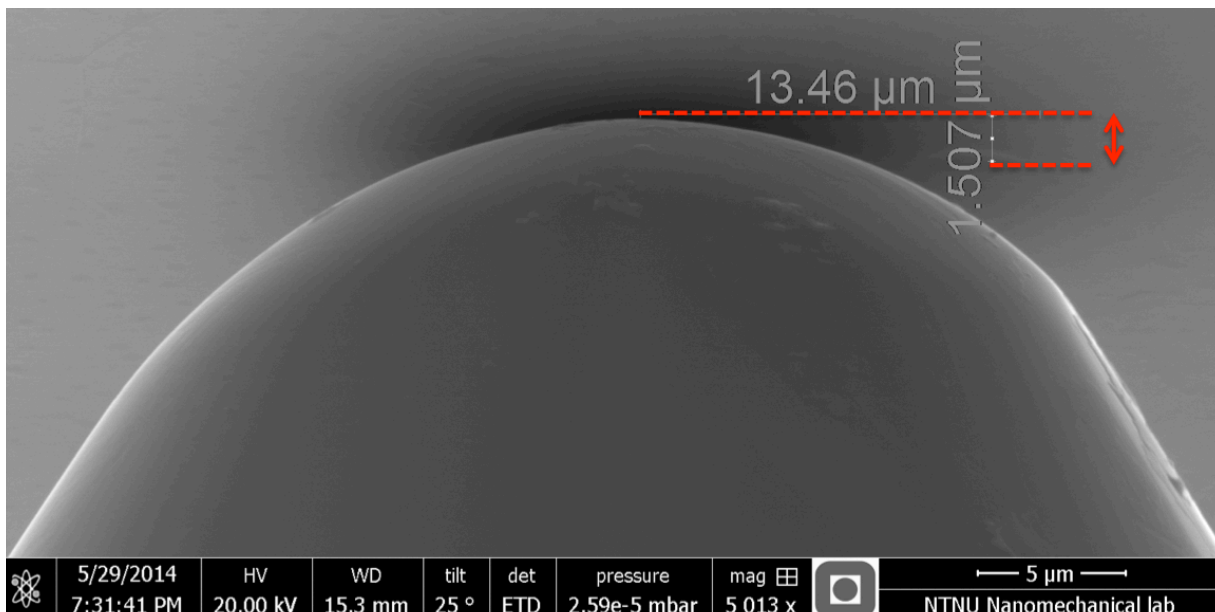


Figure 52: SEM micrograph of the cube corner probe, where the red dashed lines illustrates the distance between the indent (lower dashed line) and the top of the probe (upper dashed) visually seen with a tilt angle of  $25^\circ$ .

The load- displacement curves recorded during the pillar compression tests are shown in Figure 53 (a) and (b) for the loading directions  $\langle 235 \rangle$  and  $\langle 149 \rangle$  respectively. All displacement curves are presented individually in Appendix B. Most of the curves contain a sharp linear increase in force after yielding, at different displacements. As a result of a large difference between the dimension of the pillar and the probe, it is suspected that these linear segments are caused by contact between the probe and the crater edge, during the compression. In order to confirm these suspicions, a simple estimation relating the crater and pillar dimensions to the probe dimension, were performed. Figure 54 (a-d) shows the different scenarios considered, and the following was revealed; when the probe approaches the pillar



surface with an accurate position relative to the pillar axis, it should not hit the edge of the crater, as seen in Figure 54 (a). The probe needs to be displaced with approximately  $1,1 \mu\text{m}$  downwards the pillar central axis in order to hit the crater edge, illustrated with the red circles in Figure 54 (b). By studying the recorded load-displacement curves from the compression tests, it was evidenced that the largest displacement obtained from all the pillars were about  $600\text{nm}$ . At this displacement value, the probe should not hit the crater edge if it is located in the pillar axis. However, if the probe is located inaccurate relative to the pillar axis, contact with the crater edge is likely to happen. If the probe is approached to the pillar surface and located to the pillar axis, a lateral displacement of  $2,5\mu\text{m}$  is acceptable before the probe hit the crater edge, as shown in Figure 54(d). However, with a displacement of  $600\text{nm}$  downwards the pillar axis, the probe can only be dislocated with a distance of  $200\text{nm}$  (from the pillar axis), before the probe will hit one of the crater edges, illustrated in Figure 54 (e).

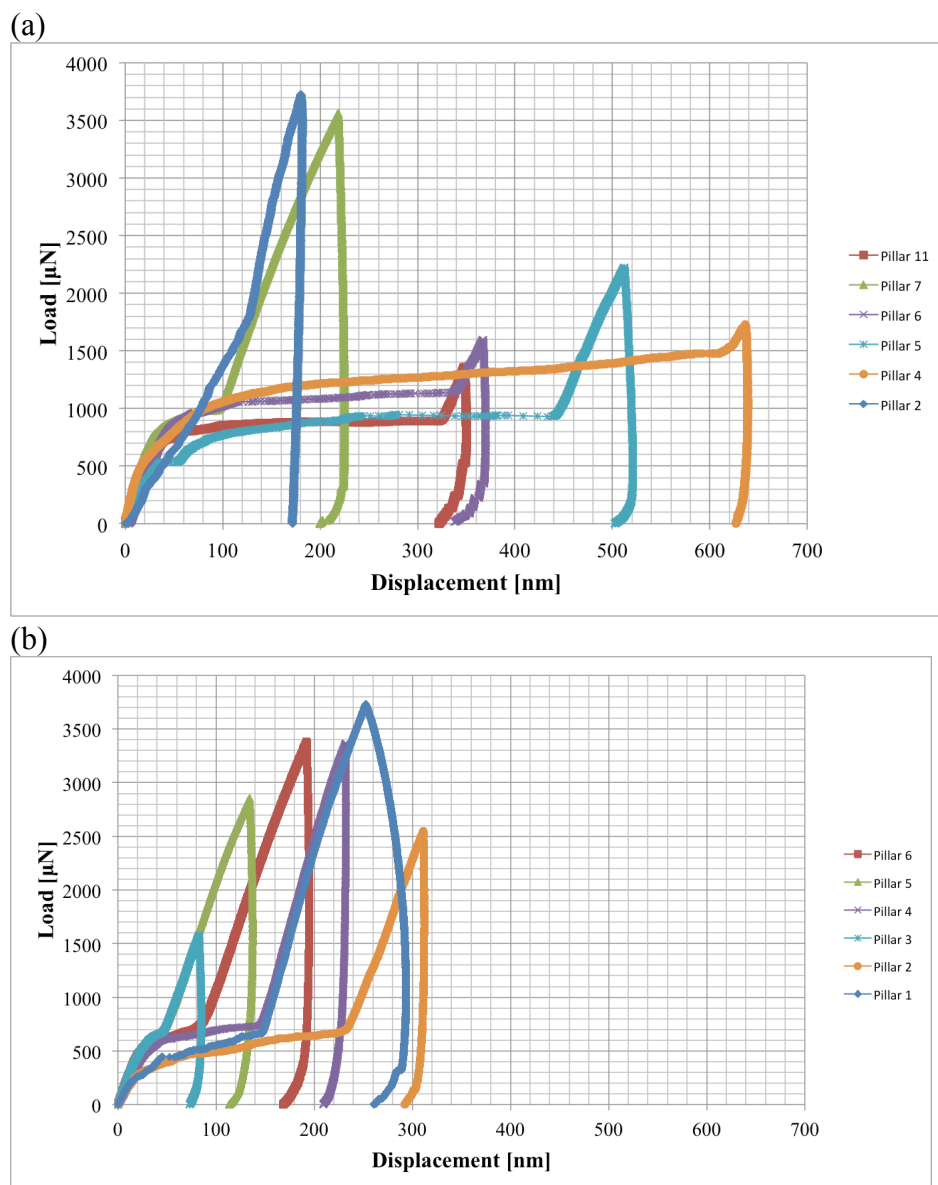
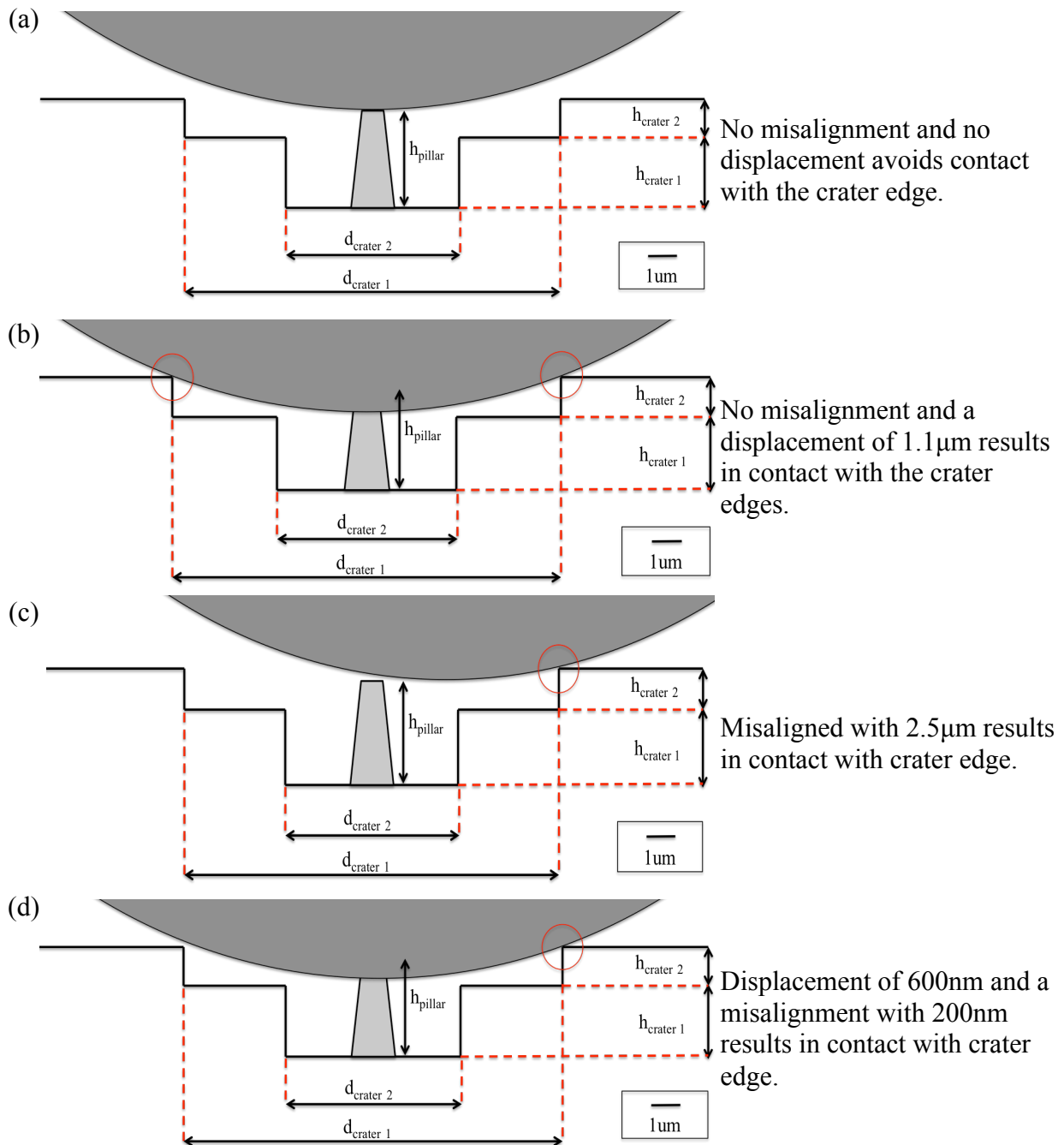


Figure 53: Load- displacement curves for the loading directions (a)  $\langle 235 \rangle$  and (b)  $\langle 149 \rangle$ .



**Figure 54: Schematic illustration of different scenarios considering location of indenter probe relative to the pillar.**

Another important factor that might have caused inaccurate approaching to the pillar axis is related to the mechanical set up of the sample. The copper stocking connecting the copper plate to the coldfinger might contain some tension in the current set-up as shown in Figure 55. In principle, the sample surface should be placed  $90^\circ$  relative to the indenter tip. However, as a result of the tension in the copper stocking, it is not excluded that the sample surface is misaligned relative to the indenter tip. Hence, it is more likely that the large probe tip will obtain contact with the crater edge in a particular displacement during compression. Initially, the intension was to perform the tests with a flat-ended probe, with a diameter of  $5\mu\text{m}$ , which is commonly used for pillar compression tests. The tip was ordered in good time. However, as

a result of a delay in the delivering, the experiments had to be conducted with the current cube corner.

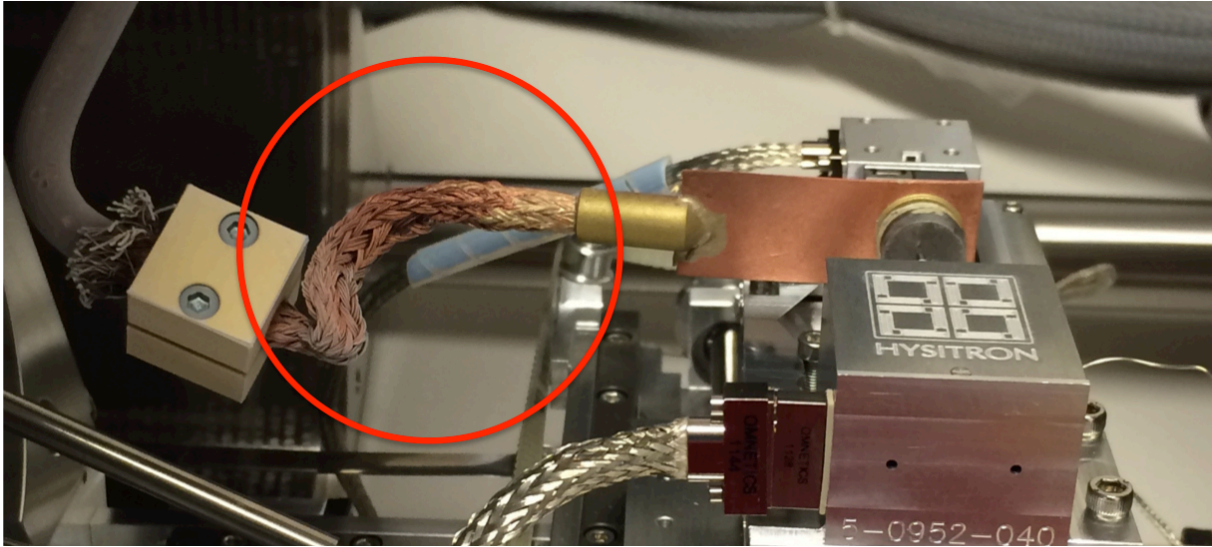


Figure 55: Image of coldfinger connected to the sample via the copper stocking. The red circle shows the twisted part of the copper stocking.

#### 4.4. Crystallographic slip

Post compression pillars were investigated to determine whether the favored slip system was of type  $\{110\}\langle 111\rangle$  or  $\{112\}\langle 111\rangle$ . The uniaxial compression tests were performed at  $-90^\circ\text{C}$  with pillars in the size of approximately  $1\mu\text{m}$  in diameter that were deformed to only a few percent strain. The limited amount of plastic deformation minimizes geometrical changes that happens during loading, hence, slip traces on the pillars surface are easier to characterize.

Study of post compression SEM images, presented in Appendix C, reveals that the Fe pillars exhibit sharp and localized slip traces on the pillar surface. The slip traces on the pillars were examined from four positions with a relative stage rotation of  $90^\circ$  between the images. One representative pillar from each orientation is shown in Figure 56 and Figure 57, viewed from the four positions. These pillars were chosen to represent the deformation morphology of the pillars tested in this study. The slip traces at the pillar surface were compared with slip trace locations calculated from the known crystal orientation and identified, as described in section 3.7. Slip traces that could be identified, are highlighted with blue and red lines for the  $\{110\}$  and  $\{112\}$  planes, respectively.

From pillars with orientation  $\langle 149\rangle$ , slip was identified both along the  $\{110\}$  and  $\{112\}$  planes. From the slip trace analysis it was confirmed that the slip system  $(101)[11\bar{1}]$  was most highly stressed, and also activated during the compression tests. The slip system had a Schmid factor ( $S$ ) of  $S=0.4986$ , and are shown in Figure 56 (d). Moreover, in the slip system  $(211)[\bar{1}11]$ , presented in Figure 56 (b), was identified with a Schmid factor of  $S=0.4320$ . However, it was revealed from the slip trace analysis that there exists another plane in a different gliding direction, with a higher Schmid factor, which was not prominent at the pillar surface.

Figure 56 (b) and (c) shows that there are tendencies of slip activation, but the slip systems were difficult to identify due to less prominent slip traces on the pillar surface. However, for

the  $\langle 149 \rangle$  oriented pillars, the primary slip system  $(101)[\bar{1}1\bar{1}]$  seemed to carry out most of the deformation, followed by secondary slip systems with lower Schmid factors.

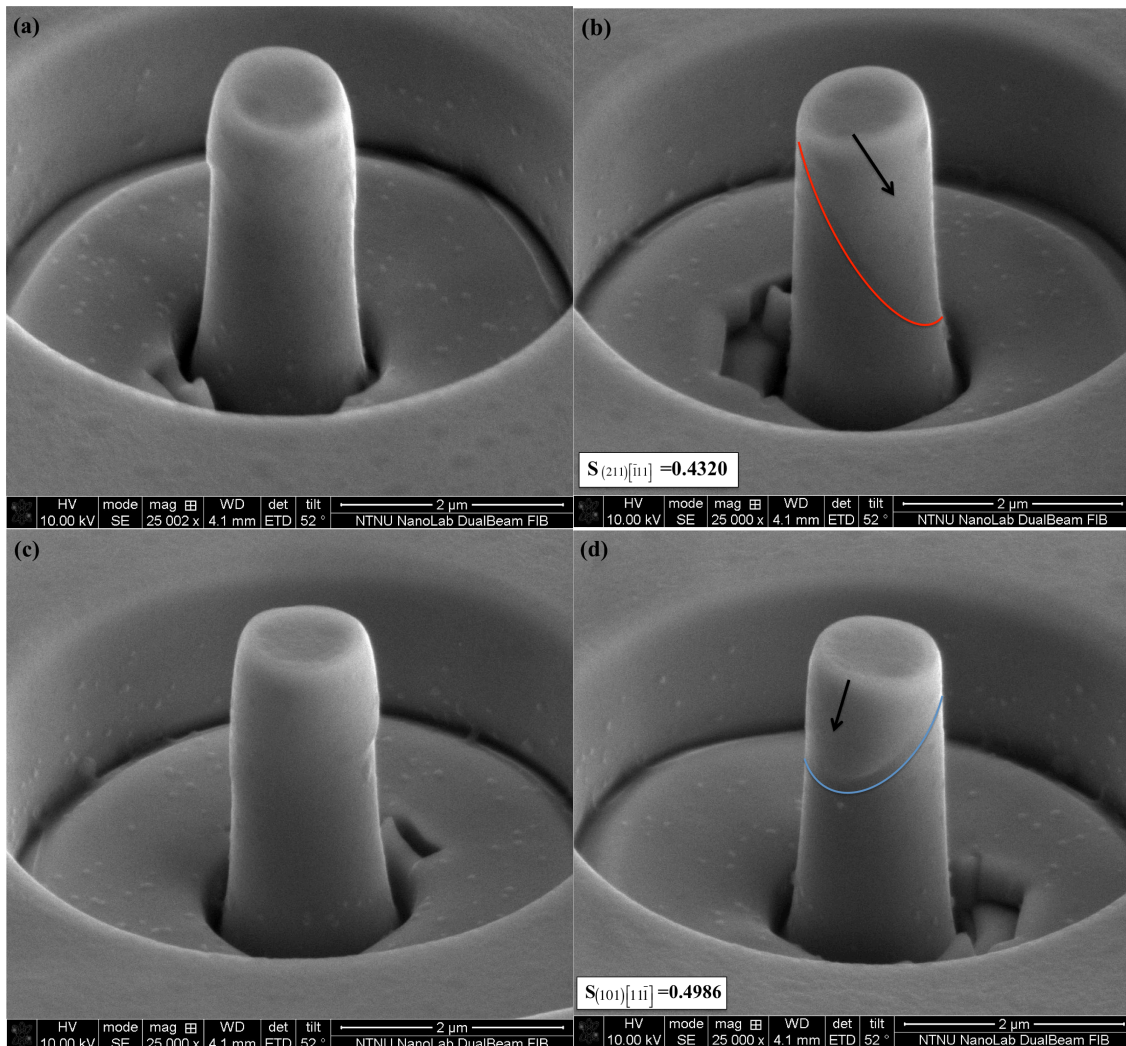


Figure 56: Loading direction  $\langle 149 \rangle$ , pillar 5 from (a)  $-90^\circ$ , (b)  $0^\circ$ , (c)  $+90^\circ$  and (d)  $+180^\circ$ .

For pillars loaded in the  $\langle 235 \rangle$  orientation, deformation in both the  $\{110\}\langle 111 \rangle$  and  $\{112\}\langle 111 \rangle$  slip systems were observed. Figure 57 (a) shows two identified slip systems of type  $(1\bar{1}2)[\bar{1}1\bar{1}]$ , with  $S = 0.4451$  and  $(101)[\bar{1}1\bar{1}]$  with  $S = 0.3134$ . From the slip trace analysis it was revealed that there was another  $\{110\}$  plane in similar direction ( $(01\bar{1})[\bar{1}1\bar{1}]$ ), with a higher Schmid factor ( $S = 0.4576$ ). This plane could not be identified on the pillar surface. Figure 57 (b) and (c) shows both slip traces on the pillar surface that could not be identified. Furthermore, examination of slip traces presented in Figure 57 (d) reveals that a slip happens on the two non parallel slip systems  $(12\bar{1})[\bar{1}1\bar{1}]$  with  $S = 0.3474$  and  $(1\bar{1}2)[\bar{1}1\bar{1}]$  with  $S = 0.4451$ , where the latter one is the similar slip system seen in Figure 57 (a).

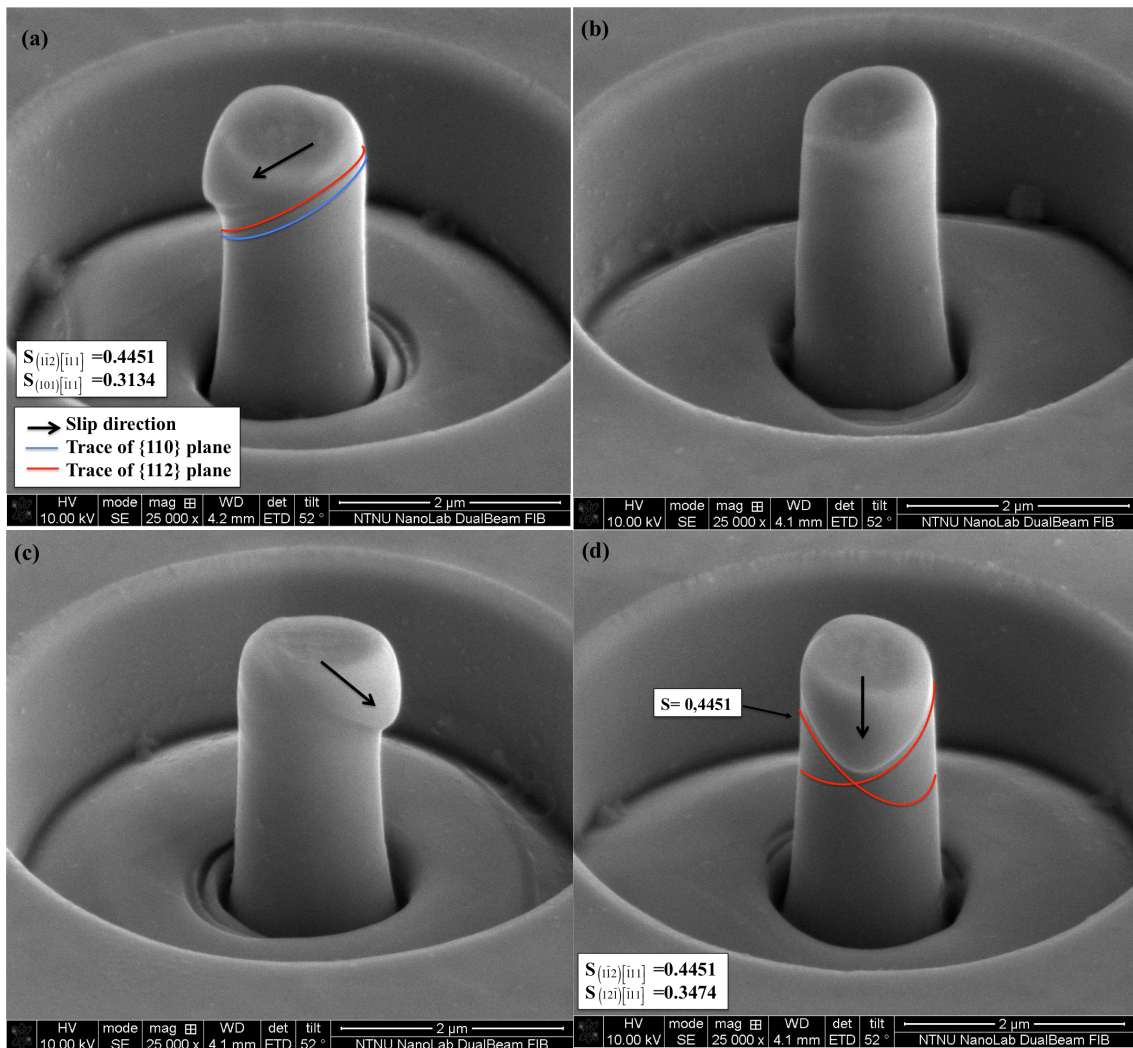


Figure 57: Loading direction  $\langle 235 \rangle$ , pillar 7 from (a)  $-90^\circ$ , (b)  $0^\circ$ , (c)  $+90^\circ$  and (d)  $+180^\circ$ .

An overview of the different slip systems identified during the slip trace analysis, are presented in Table 11. In pillars with orientation  $\langle 149 \rangle$ , the slip system  $\{110\}\langle 111 \rangle$  were observed to carrying out the major part of the deformation with the primary slip system  $(101)[\bar{1}1\bar{1}]$ . From Rogne and Thaulow's work [2], the most dominating slip for  $\langle 149 \rangle$  oriented pillars were most frequently seen in the  $(\bar{1}01)[\bar{1}11]$  primary slip system, followed by secondary slip systems. This highest stressed slip system, were also dominating the deformation of the  $\langle 235 \rangle$  oriented pillars, as showed in Figure 19 (section 2.3.1.). However, during the slip trace analysis, it was revealed that an additional slip system of type  $(\bar{2}11)[\bar{1}11]$ , with similar a Schmid factor, was present in the  $\langle 235 \rangle$  orientated pillar but not preferred during deformation. This slip mechanisms observed at room temperature for  $\langle 235 \rangle$  oriented pillars, are not consistent with the results obtained in the present work. The deformation of the  $\langle 235 \rangle$  oriented pillars at  $-90^\circ\text{C}$ , were identified to be dominated by the slip system  $\{112\}\langle 111 \rangle$ . The most prominent deformation are shown in Figure 57 (d), where the slip is carried out by the two slip systems and  $(12\bar{1})[\bar{1}11]$  and  $(1\bar{1}2)[\bar{1}11]$ . Examination of these slip traces reveals the slip happen on two non parallel slip planes. This slip mechanism was also observed in Rogne and Thaulow's work for  $\langle 001 \rangle$  oriented pillars at room temperature [24], shown in Figure 21. However, these slip traces were identified to be of the  $\{110\}$  planes.

**Table 11: Slip systems observed after compression of pillars.**

Orientation	Slip systems observed	Schmid factor, $S$	Other slip systems with higher $S^*$	Family of planes
[149]	(101)[ $\bar{1}\bar{1}\bar{1}$ ]	0.4986	No	{110}
	(211)[ $\bar{1}\bar{1}\bar{1}$ ]	0.4320	Yes (different direction)	{112}
[235]	( $\bar{1}\bar{1}\bar{2}$ )[ $\bar{1}\bar{1}\bar{1}$ ]	0.4451	(01 $\bar{1}$ )[ $\bar{1}\bar{1}\bar{1}$ ] (0.4576)	{112}
	(12 $\bar{1}$ )[ $\bar{1}\bar{1}\bar{1}$ ]	0.3474	no	{112}
	(101)[ $\bar{1}\bar{1}\bar{1}$ ]	0.3134	no	{110}

\*Referring to the slip system(s) that was calculated from the slip trace analyses, but observed/identified on the pillar surface.

By comparing the slip trace analysis performed at room temperature versus the ones conducted at  $-90^{\circ}\text{C}$ , it is concluded that for <149> oriented pillars, slip are preferred in the {110}<111> slip system for both temperatures. In contrast, the <235> oriented pillars, exhibit slip in the {112}<111> slip system at low temperatures versus {110}<111> at room temperature. Furthermore, as mentioned above, <235> oriented pillars in the present work exhibited slip on secondary slip planes and not on the primary slip plane (01 $\bar{1}$ )[ $\bar{1}\bar{1}\bar{1}$ ], that were discovered in the slip trace analysis.

In the Theoretical Background, it is well mentioned that slip occurs mostly on {110} planes at lower temperatures, which is in line with the results obtained for <149> oriented pillars. However crystallographic slip in bcc metals is known to be complex and several possible mechanisms can influence the deformation behavior [1, 63, 68]. Bcc crystals are known to deform in one or in a combination of the {110}, {112} and {123} families of planes, in the most closely packed direction <111>. The large number of possible slip systems, in total 48, complicates the slip trace analysis and identification of slip traces contains an uncertainty. Furthermore, the results presented above, shows that several slip systems can carry out the deformation of one pillar. Taking into account the complexity of the bcc structure, there could be several reasons for this. However, in this experimental work, is it assumed that, the small misalignment between the indenter tip and pillar top-surface during compression, might cause a stress distribution that could be beneficial for deformation of secondary slip systems. Large pillars include several dislocations on each available plane and consequently the highest stressed plane will determine where the deformation starts [2]. Another important factor that should not be excluded from this consideration is the violation of Schmid's law for bcc metals [16, 39], also explained in detail in section 2.1.4. in the Theoretical Background. The presence of anomalous slip behavior in bcc metals is attributed to the twinning-antitwinning asymmetry of shearing of slip direction <111> along {112} planes. The source of this asymmetry is related to the threefold symmetry in the structure of the cores of screw dislocations [16]. In the <235> oriented pillars, it was revealed that secondary slip system of {112} planes were dominating the deformation, hence it is reasonable to believe that this anomalous slip behavior could be related to asymmetry in the bcc structure. By this assumption, it can be stated that the violation of Schmid's law, is more prominent at lower temperatures, taken into

account that anomalous slip behavior was not evidenced for  $\langle 235 \rangle$  oriented pillars at room temperature in Rogne and Thaulow's work [2], whereas the primary slip system was dominating the deformation. Overall, in order to confirm such statements, it requires a more detailed study of several grains and a larger amount of pillars in order to obtain a fully understanding. Additionally, deformation dominated by anomalous slip, were not observed for  $\langle 149 \rangle$  oriented pillars at  $-90^\circ\text{C}$ .

As mentioned, the pillars were deformed to only a few percent strains to be able to perform the slip trace analysis with as little uncertainty as possible. However, one of the pillars was compressed with higher loads, in order to observe how the deformation developed, as shown in Figure 58 (a). High magnification images of the slip steps, as shown in Figure 58 (b) demonstrate that several crystallographic glide planes contributed to the deformation. The glide steps in the iron pillars appears to be well resolved on single crystallographic planes, and not wavy slip behavior, that is attributed to cross-slip of  $a/2 \langle 111 \rangle$  screw dislocations [63]. This is consistent with the observations in the previous study of Fe pillars [24]. For this purpose it can be assumed that cross-slip is dominating the deformation mechanisms. However, it should also be considered that the well resolved crystallographic slips, could be an effect of the lower temperature in these experiments.

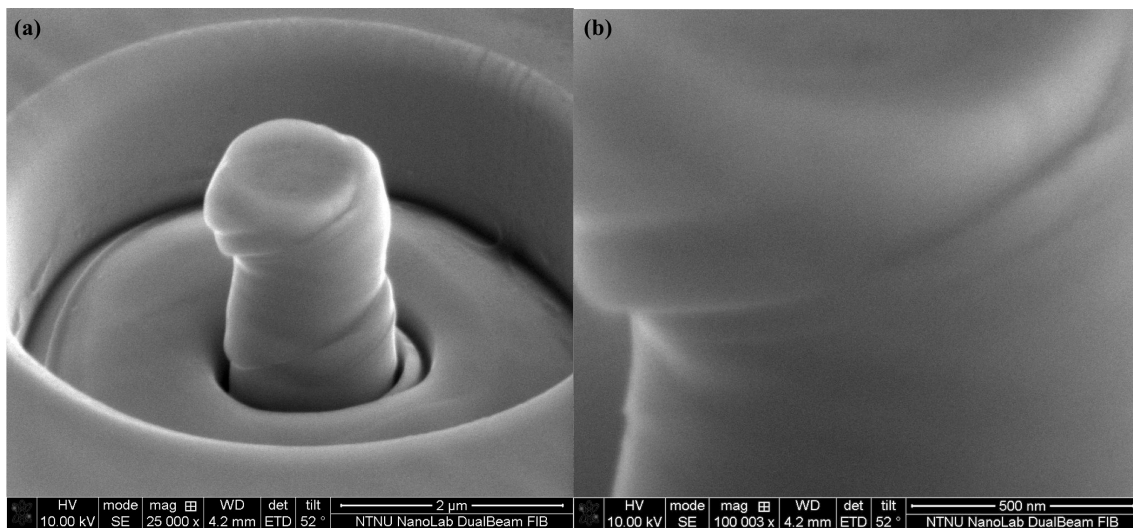


**Figure 58:** Post compression SEM images of  $\langle 235 \rangle$  oriented Fe pillar. Higher magnification image highlight the slip trace morphology.

#### 4.5. Mechanical behavior and the influence on flow curves

Figure 59 (a) and (b) shows the stress-strain curves of Fe-pillars obtained at  $-90^\circ\text{C}$ , for the two orientations  $\langle 235 \rangle$  and  $\langle 149 \rangle$  respectively. All stress-strain curves obtained are presented individually in Appendix D. As discussed in section 4.3., it is suspected that the indenter probe are in contact with the crater edge during loading as a result of misalignment between the indenter tip and pillar axis. This is clearly reflected in the stress-strain curves (some more than others), from the sharp increase in force appearing after a particular displacement. As a result of this, only the stress-strain response before the force increase appears, will be considered in the following paragraphs.

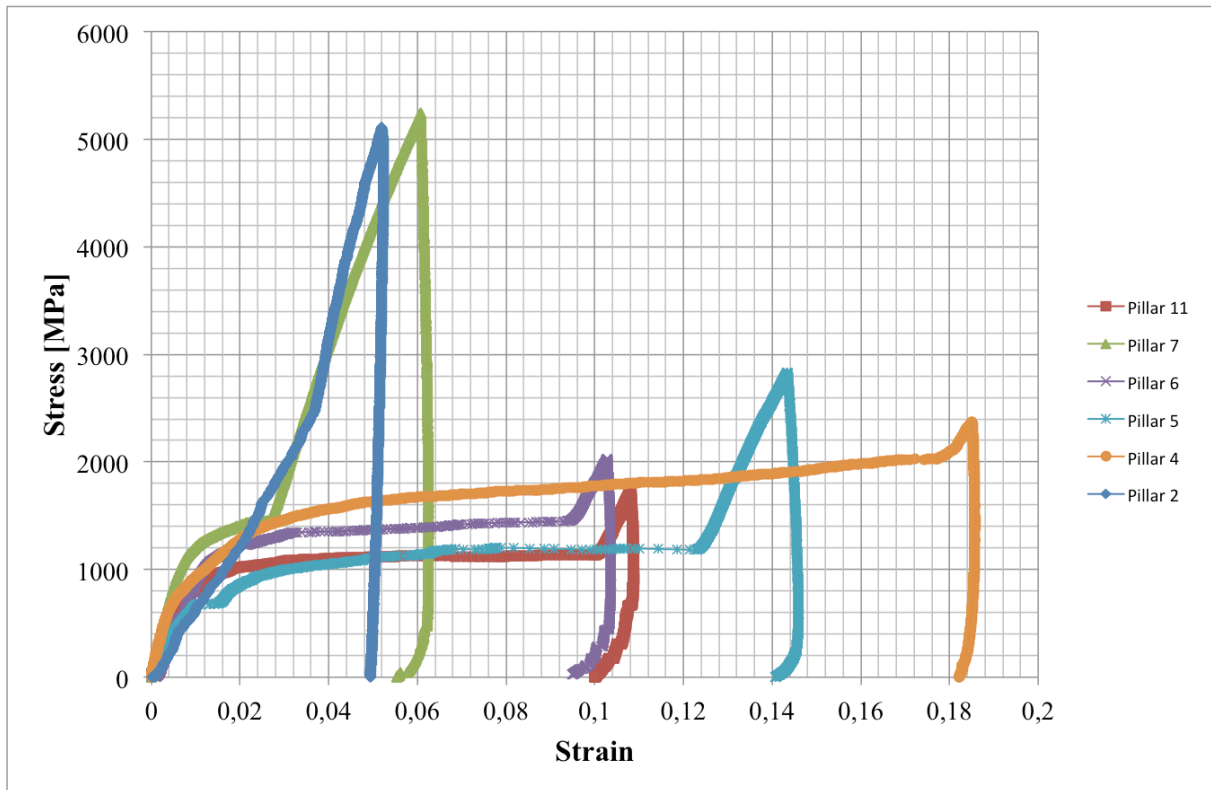


Figure 59: Stress-strain curves of <235> oriented Fe pillars with diameters about 1  $\mu\text{m}$ .

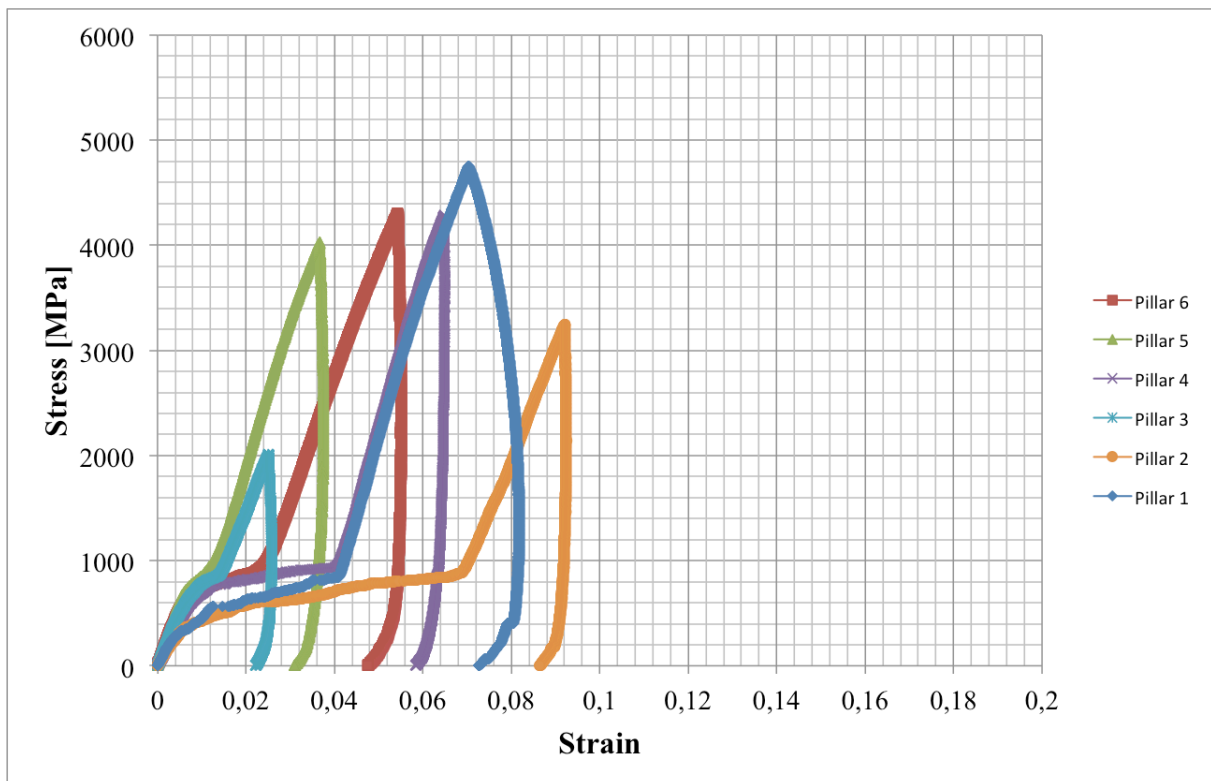


Figure 60: Stress-strain curves of <149> oriented Fe pillars with diameters about 1  $\mu\text{m}$ .

For both orientations the pillars exhibit relatively continuous and smooth stress-strain curves, which is commonly seen for pillars at this size range ( $d_i \geq 1 \mu\text{m}$ ) [2, 24, 63]. The use of the 0,2% offset method for determining the yield stress was not possible due to the low initial



stiffness caused by slight indenter-pillar misalignment and pillar surface roughness. Therefore, stress at an axial strain of 2.5% was chosen as a representation of yield strength because it is high enough to ensure that plastic deformation had occurred. This approach is consistent with the majority of pillar compression studies. The stress values obtained at 2.5% and 5% strain for both orientations were compared to experimental results from B. R. S. Rogne, that were analyzed in “B. R. S. Rogne and C. Thaulow, submitted to Materials Science and Engineering A”, and presented in Figure 61 and Figure 62. The Fe pillars tested by B.R.S. Rogne, had similar pillar diameter as in the present work, i.e. about  $1\mu\text{m}$ , and loaded at room temperature (about  $29\text{ }^\circ\text{C}$ ). Figure 61 and Figure 62 shows that the strength values for the pillars loaded at low temperatures are significantly higher than the ones loaded at room temperature.

For orientation  $\langle 235 \rangle$ , the average stress value at 2.5% strain is 1070MPa at  $-90^\circ\text{C}$ , but 644MPa at room temperature, which is a reduction of 39.8%. For orientation  $\langle 149 \rangle$  the average stress value at 2.5% strain is 710MPa at  $-90^\circ\text{C}$ , and 637MPa at room temperature, which is 10.3% reduction. Similar temperature dependence were also seen for orientation  $\langle 235 \rangle$  at 5% strain where an average stress value of 1286MPa was obtained at  $-90^\circ\text{C}$ , but 753MPa at room temperature, which is a reduction of 41,5%. From all the stress-strain curves obtained from  $\langle 149 \rangle$  oriented pillars at  $-90^\circ\text{C}$ , there was only one curve that could give a stress value at 5% strain before the sharp force increase appeared, which was 788MPa. The average stress value at 5% strain from the experiments performed by B.R.S. Rogne, was 776 MPa for  $\langle 149 \rangle$  oriented pillars at room temperature. Hence, comparison between one pillar at low temperature versus several at room temperature will not give reliable results. It should be noted that it was not possible to measure these stress values for all pillars, since the linear segment of the stress-strain curve initiated in some cases at strain values lower than 2,5% or 5%. Hence, these pillars were excluded from this consideration. There is a noteworthy scatter in some of the presented stress-strain data obtained at lower temperatures, however, it is overall observed at prominent temperature dependence on the yield strength, in terms of higher strength at lower temperatures. This observation is more prominent  $\langle 235 \rangle$  oriented pillars, than for  $\langle 149 \rangle$  oriented pillars

The temperature dependency make sense since the intrinsic lattice resistance of bcc crystals is usually higher at lower temperature, resulting in the higher required stress for the motion of dislocations, i.e. the operation of dislocation sources [75]. The temperature dependence of yield stress of pure bcc metals is associated with the core structure of screw dislocations where the glide resistance is the highest, as a result of rotational asymmetry around the  $\langle 111 \rangle$  densest direction of slip. The core structure of screw dislocations is not planar, but spreads spatially and causes the high lattice friction, i.e. Peierl’s stress, which is considered to control the low temperature deformation of bcc metals [15, 29, 42].

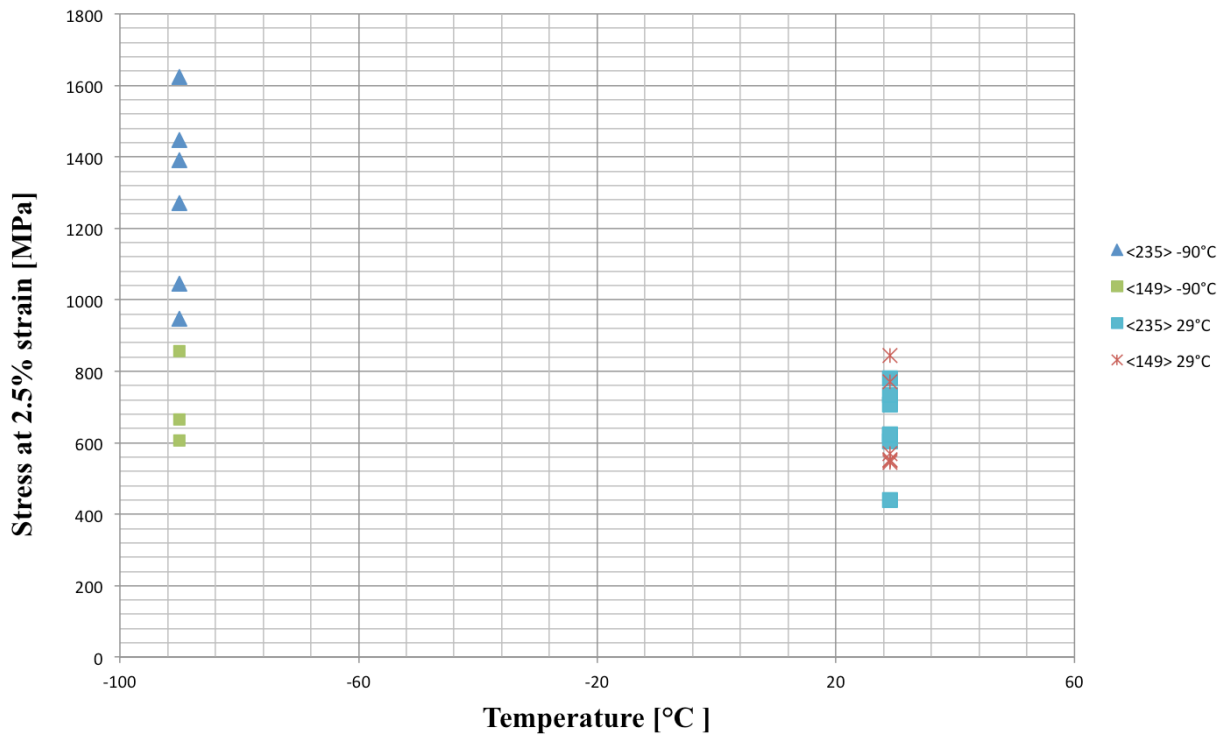


Figure 61: Plot of stress at 2.5% strain ( $\sigma_{2.5\%}$ ) as a function of operating temperature for two orientations. Data representing experiments at 29°C are obtained from B.R.S. Rogne.

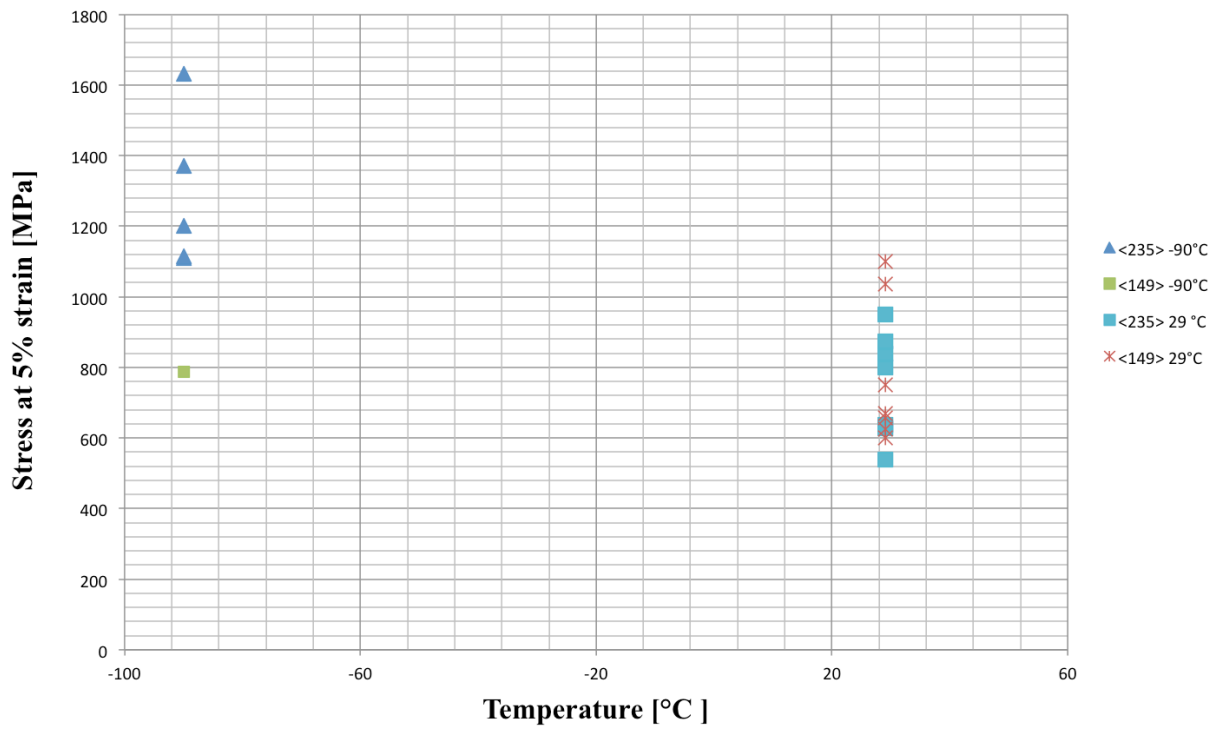


Figure 62: Plot of stress at 5% strain ( $\sigma_{5\%}$ ) as a function of operating temperature for two orientations. Data representing experiments at 29 °C are obtained from B.R.S. Rogne.

## 5. Conclusion

A cooling system interfaced with a Scanning Electron Microscopy (SEM), have been constructed in order to study the low temperature deformation mechanisms of bcc  $\alpha$ -Fe. Focused Ion beam (FIB) machined pillars with a diameter of 1  $\mu\text{m}$ , were subjected to nanocompression in-situ, at  $-90^\circ\text{C}$  within the two different grain orientations  $\langle 149 \rangle$  and  $\langle 235 \rangle$ . Based on the nanomechanical testing methods conducted, slip trace analysis and the stress-strain curves with the corresponding inspection of the recorded in-situ compression, the following conclusions were made:

- The developed in-situ cooling system for nanomechanical testing, has the capability to reduce the sample temperature down to  $-90^\circ\text{C}$ . The simultaneous cooling of the sample ensures reliable mechanical tests. Thermal drift rates of 5.2 nm/s were found at  $-90^\circ\text{C}$ , and a drift rate of 0.6nm/s were seen at room temperature. Considering each compression test lasts for approximately 15 seconds, it is not assumed that the drift have influenced the present experiments in a high degree. With a testing time longer than 15 seconds, drift would probably have affected the obtained results.
- Slip trace analysis were performed to determine the whether the operating slip system where of  $\{110\}\langle 111 \rangle$  or  $\{112\}\langle 111 \rangle$ . Based on slip trace analysis, it was revealed that deformation on  $\langle 235 \rangle$  oriented pillars are dominated by secondary slip systems in  $\{112\}$  planes, whereas deformation on  $\langle 149 \rangle$  oriented pillars are dominated by the primary slip system  $(101)[11\bar{1}]$ . It is assumed that the subsequent deformation mechanisms are affected and dependent of the relative intrinsic properties and microstructural features of the bcc structure at lower temperatures. Furthermore, it is suspected that slip activation observed on secondary slip systems for  $\langle 235 \rangle$  oriented pillars, could be a result of the breakdown of Schmid's law, stating that anomalous slip are more preferred, as well as influence of misalignment between the indenter tip and pillar top-surface.
- The Stress-strain data at obtained at  $-90^\circ\text{C}$  where compared to those obtained at room temperature in Rogne and Thalow's work [2], for the orientations  $\langle 235 \rangle$  and  $\langle 149 \rangle$ .  $\langle 235 \rangle$  oriented pillars exhibits 39.8% higher stress at 2.5% strain at  $-90^\circ\text{C}$ , than  $\langle 235 \rangle$  oriented pillars obtain at room temperature (1070MPa vs. 644MPa). At 5% strain, similar tendencies are seen; 41.5% higher stress are obtained at  $-90^\circ\text{C}$ , than at room temperature (1286MPa vs. 753MPa). For  $\langle 149 \rangle$  oriented pillars 10.3% higher stress is obtained at 2.5% strain at  $-90^\circ\text{C}$ , than for  $\langle 149 \rangle$  oriented pillars obtain at room temperature (710 vs. 637MPa). Here, average stress values from several pillars are used. This comparison indicate that the flow curve is significantly affected by the temperature decrease, where it is concluded that the strength of  $\alpha$ -Fe pillars, increases with decreasing temperature.
- Nanocompression testing in-situ is a powerful method, suitable for analyzing the subsequent deformation behavior of pillars of micro-and nanosize. However the large size difference between the indenter probe (diameter of 40 $\mu\text{m}$ ) probe, and pillars ( $d=1\mu\text{m}$ ), contribute to challenges in locating the probe tip precisely above the center of the pillar, hence contact with the crater edge during compression is likely. In this experience, it is assumed contact with the crater edge after a particular displacement. However, in order to analyze the compression test results, the data obtained before crater contact are used.

## 6. Further work

The work carried out in this Master thesis has revealed many promising areas of further research in the nanomechanical testing field. A few of these areas worthy for further investigations can briefly be summarized as follows.

The cooling system developed in this work was able to cool down the sample to  $-90^{\circ}\text{C}$ . However, it is not possible to control the temperature during cooling. For that purpose, heating is necessary to precisely control the temperature. By this an additional heating component connected to the cooling system, has to be developed. Hence, the operating temperature can be controlled from  $29^{\circ}\text{C}$  to  $-90^{\circ}\text{C}$ .

A thermal drift rate of  $5.2\text{ nm/s}$  was registered during the current experiments, as a result of large temperature differences between the sample and the indenter probe. In order to avoid drift effects during compression and indentation tests at lower temperatures, a constant temperature of the probe (equal to the sample temperature) is needed. By developing the cooling system with an additional cooling component connected to the indenter tip, more equivalent temperatures on the sample and indenter probe might be obtained.

During ventilation of the SEM chamber after compression experiments at low temperatures, the copper rod is covered by ice. Since it takes a couple of minutes to ventilate the SEM chamber, the copper rod can't be dismantled immediately, hence there is a risk that the ice from the copper rod might cause contamination of the SEM chamber. A development of the current system is important here, in order to perform safely experiment with the cooling system.

In the current experiments it was used a cube corner indenter probe with a diameter of  $40\mu\text{m}$ . Considering the large size differences between the indenter probe and pillars with a diameter of  $1\mu\text{m}$ , challenges with misalignments were experienced. For compression tests on pillars at this size, it is preferable to use a flat-ended indenter probe with a diameter of approximately  $5\mu\text{m}$ . This type of probe was initially intended to use in the present work. The tip was ordered in good time, however, due to delay in the delivering, the experiments had to continue with the indenter probe available, i.e. the cube corner probe.

Even though the results obtained in this experiment were reliable, it is still necessary to perform additionally similar experiments, in order to obtain an extended understanding for the deformation mechanisms observed at low temperatures, thus a higher validation of the results is obtained. Furthermore, a larger amount of pillars tested, would have given a stronger confirmation of the obtained results.

While much has been learnt from the current nanomechanical testing studies of bcc Fe at low temperatures, the literature research should be expanded to include deformation behavior at lower temperatures for materials related to the project "Arctic Materials".

## 7. Acknowledgements

Sincere thanks goes to the persons who have been of great help at during of this work. They have really balanced their job elegantly between providing the right information, challenging me, and showing interest for my opinions and work. First, I would like to thank my supervisor Prof. Christian Thaulow for excellent advices and for being helpful throughout the entire duration of this work. His encouragement and enthusiasm has strongly motivated me to put a lot of effort in this work. I am amazed by his positive attitude and his ability to find solutions and new ideas.

PhD candidate Bjørn Rune Sørås Rogne stands out as one of the people that have truly helped me reaching my goals. I thank him for all the support and assistance during both the experimental and analytical work throughout the semester. I value the generosity of his time and for sharing his insights and experiences related to this work. He has been able to implement everything I have asked about.

Grateful thanks also go to Prof. Afrooz Barnoush (NTNU) and Senior Engineer Nousha Kheradmand (NTNU) for good help with management of the laboratory equipment and for sharing their knowledge related to testing procedures and experimental solutions.

I would like to thank Prof. Jarle Hjelen (NTNU) for helpful inputs and suggestions related to the construction of the cooling system.

Sincerely thanks goes to Dr. Yingda Yu (NTNU) for always being available every time I asked for help, even if it was during his lunchbreak or in a middle of a meeting. I also thank him for good training and assistance with SEM, EBSD, and the indexing softwares.

Most of the components and parts related to the cooling system constructed in this thesis were fabricated at the Finemechanical workshop (NTNU) and the Workshop at the Department of Engineering Design and Materials (NTNU). I really appreciate the professional work they have done, and thank them for always being accommodating when I needed their assistance.

I acknowledge SINTEF (“Arctic Materials”), for supporting my attendance at the Nanomechanical testing conference, “Nanobrücken” in Saarbrücken. The conference was of great inspiration for my master thesis and contributed to give me an extended knowledge within the nanomechanical testing field.

Finally, I would like to thank all my colleagues at The Department of Engineering Design and Materials (NTNU) for creating a friendly atmosphere during my year at this department. Especially thanks goes to my better half, Kristine Greina for being an outstanding teammate during this journey.



## Bibliography

1. Marichal, C., *{110} Slip with {112} slip traces in bcc Tungsten*. Scientific Reports, 2013.
2. Sørås Rogne, B.R. and C. Thaulow, *Effect of Crystal Orientation on the Strengthening of Iron Pillars*. Materials Science and Engineering: A, 2014.
3. IRIS, L. *Arctic materials technology development*. Available from: <http://iris.lut.fi/academic-network/projects/arctic-materials-technologies-development>.
4. SINTEF. *Arctic Materials*. Available from: <http://www.sintef.no/Projectweb/Arctic-Materials/>.
5. Rogne, B.R.S., *Application of Focused Ion Beam (FIB) on Arctic Steels*, in *Department of Product Development and Materials* 2012, Norwegian University of science and Technology: Trondheim.
6. Thaulow, C., J. Ødegård, and E. Østby, *Arctic Steels - Criteria for safe materials utilisation*.
7. Yao, N., *Focused Ion Beam Systems- Basics and Applications* . 2007: Cambridge University Press.
8. environment, a.; Available from: <http://www.neb-one.gc.ca/clf-nsi/rpblctn/spchsndprsnntn/2012/cntrbtnsstnblnrgftr/cntrbtnsstnblnrgftr-eng.html>.
9. Raabe, D., D. Ma, and F. Roters, *Effects of initial orientation, sample geometry and friction on anisotropy and crystallographic orientation changes in single crystal microcompression deformation: A crystal plasticity finite element study*. Acta Materialia, 2007. **55**(13): p. 4567-4583.
10. Ersland, C.H. and C.Thaulow, *Modeling of size and strain rate effects in compression tests of iron nanopillars*. Elsevier, 2012.
11. Greer, J.R. and W.D. Nix, *Nanoscale gold pillars strengthened through dislocation starvation*. Physical Review B, 2006. **73**(24): p. 245410.
12. Min Han, S., et al., *Critical-temperature/Peierls-stress dependent size effects in body centered cubic nanopillars*. Applied Physics Letters, 2013. **102**(4): p. -.
13. Schneider, A.S., et al., *Influence of test temperature on the size effect in molybdenum small-scale compression pillars*. Philosophical Magazine Letters, 2013. **93**(6): p. 331-338.
14. Seeger, A., *Why anomalous slip in body-centred cubic metals?* Materials Science and Engineering: A, 2001. **319-321**(0): p. 254-260.
15. Caillard, D., *Kinetics of dislocations in pure Fe. Part II. In situ straining experiments at low temperature*. Acta Materialia, 2010. **58**(9): p. 3504-3515.
16. Gröger, R. and V. Vitek, *Breakdown of the Schmid law in bcc molybdenum related to the effect of shear stress perpendicular to the slip direction*. Materials Science and Engineering, 2005.
17. Kim, J.-Y., D. Jang, and J.R. Greer, *Tensile and compressive behavior of tungsten, molybdenum, tantalum and niobium at the nanoscale*. Acta Materialia, 2010. **58**(7): p. 2355-2363.
18. Frick, C.P., et al., *Size effect on strength and strain hardening of small-scale [111] nickel compression pillars*. Elsevier, 2007.
19. Kheradmand, N., H. Vehoff, and A. Barnoush, *An insight into the role of the grain boundary in plastic deformation by means of a bicrystalline pillar compression test and atomistic simulation*. Acta Materialia, 2013. **61**(19): p. 7454-7465.
20. A.M. Minor, J.Y.a.R.K.M., *In situ TEM nanocompression testing*. 2008.

21. Kuramoto, E., Y. Aono, and K. Kitajima, *Thermally activated slip deformation of high purity iron single crystals between 4.2 K and 300 K*. Scripta Metallurgica, 1979. **13**(11): p. 1039-1042.
22. Taylor, G., *Thermally-activated deformation of BCC metals and alloys*. Progress in Materials Science, 1992. **36**(0): p. 29-61.
23. Wu, S.Z., et al., *Deformation twinning in submicron and micron pillars of twinning-induced plasticity steel*. Scripta Materialia, 2012. **67**(7-8): p. 641-644.
24. Sørås Rogne, B.R. and C. Thaulow, *Strengthening Mechanisms of Iron Pillars*. Philosophical Magazine 2014.
25. Argon, A.S., *Strengthening Mechanisms in Crystal Plasticity*. 2008: Oxford University Press.
26. Shetty, M.N., *Dislocations and Mechanical Behaviour of Materials*. 2013.
27. Frenkel, J., *Zur Theorie der Elastizitätsgrenze und der Festigkeit kristallinischer Körper*. Zeitschrift für Physik, 1926. **37**(7-8): p. 572-609.
28. Hull, D. and D.J. Bacon, *Chapter 1 - Defects in Crystals*, in *Introduction to Dislocations (Fifth Edition)*, D. Hull and D.J. Bacon, Editors. 2011, Butterworth-Heinemann: Oxford. p. 1-20.
29. Dieter, G.E., *Mechanical Metallurgy*. 1988, UK: McGraw-Hill Book Company.
30. Haugen, V.G., *Nanomechanical testing of Steel*, in *Department of Engineering Design and Materials 2012*, Norwegian University of Science and Technology: Trondheim, Norway.
31. Caillard, D., *Kinetics of dislocations in pure Fe. Part I. In situ straining experiments at room temperature*. Acta Materialia, 2010. **58**(9): p. 3493-3503.
32. Ogata, S., J. Li, and S. Yip, *Energy landscape of deformation twinning in bcc and fcc metals*. Physical Review B, 2005. **71**(22): p. 224102.
33. D.Hull and D.J. Bacon, *Introduction to Dislocations*. Butterworth Heinemann.
34. Wong, S.L., *Deformation Twinning: Mechanisms and Their Role in Crystal Plasticity Models*.
35. Ersland, C.H., *Atomistic modeling of failure in iron*, 2012.
36. Peileg, J., *Mechanical Properties of Materials*, 2013. p. 152-153
37. Vitek †, V., *Core structure of screw dislocations in body-centred cubic metals: relation to symmetry and interatomic bonding*. Philosophical Magazine, 2004. **84**(3-5): p. 415-428.
38. Spitzig, W.A. and A.S. Keh, *Orientation and temperature dependence of slip in iron single crystals*. Metallurgical Transactions, 1970. **1**(10): p. 2751-2757.
39. Ito, K. and V. Vitek, *Atomistic study of non-Schmid effects in the plastic yielding of bcc metals*. Philosophical Magazine A, 2001. **81**(5): p. 1387-1407.
40. Kang, K., V.V. Bulatov, and W. Cai, *Singular orientations and faceted motion of dislocations in body-centered cubic crystals*. Proceedings of the National Academy of Sciences, 2012. **109**(38): p. 15174-15178.
41. Argon, A.S., *Strengthening Mechanisms in Crystal Plasticity*. 2008: p. 78-84.
42. Caillard, D., *On the stress discrepancy at low-temperatures in pure iron*. Acta Materialia, 2014. **62**(0): p. 267-275.
43. Monnet, G., L. Vincent, and B. Devincre, *Dislocation-dynamics based crystal plasticity law for the low- and high-temperature deformation regimes of bcc crystal*. Acta Materialia, 2013. **61**(16): p. 6178-6190.

44. Naamane, S., G. Monnet, and B. Devincre, *Low temperature deformation in iron studied with dislocation dynamics simulations*. International Journal of Plasticity, 2010. **26**(1): p. 84-92.
45. Brunner, D. and J. Diehl, *Temperature and Strain-Rate Dependence of the Tensile Flow Stress of High-Purity  $\alpha$ -Iron below 250 K. I. Stress/Temperature Regime III*. Physica Status Solidi a-Applied Research, 2006. **124**(2): p. 455-464.
46. Brunner, D. and J. Diehl, *phys.stat.sol. (a)*, 1991. **124**: p. 155-170.
47. Brunner, D. and J. Diehl, *phys. Status Solidi (a)*, 1991. **124**: p. 455-464.
48. Brunner, D. and J. Diehl, *Phys. Status Solidi*, 1991. **124**: p. 203-216.
49. Caillard, D., *TEM in situ straining experiments in Fe at low temperature*. Journal of Physics: Conference Series, 2010. **240**(1): p. 012011.
50. Yalcinkaya, T., *Microstructure evolution in crystal plasticity: strain path effects and dislocation slip patterning*, in *Technische Universiteit Eindhoven* 2011.
51. Tang, M., L.P. Kubin, and G.R. Canova, *Dislocation mobility and the mechanical response of b.c.c. single crystals: A mesoscopic approach*. Acta Materialia, 1998. **46**(9): p. 3221-3235.
52. Oliver, W.C. and G.M. Pharr, *Measurement of hardness and elastic modulus by instrumented indentation: Advances in understanding and refinements to methodology*. Journal of Materials Research, 2004. **19**(01): p. 3-20.
53. Doerner, M.F. and W.D. Nix, *A method for interpreting the data from depth-sensing indentation instruments*. Journal of Materials Research, 1986. **1**(04): p. 601-609.
54. Uchic, M.D., et al., *Exploring specimen size effects in plastic deformation of Ni3(Al, Ta)*. Mater. Res. Soc. Proc, 2003. **753**.
55. Fei, H., et al., *Evaluation of Micro-Pillar Compression Tests for Accurate Determination of Elastic-Plastic Constitutive Relations*, Arizona State University.
56. Zhang, H., et al., *The design of accurate micro-compression experiments*. Scripta Materialia, 2006. **54**(2): p. 181-186.
57. Lohmiller, J.A., *Investigation of deformation mechanisms in nanocrystalline metals and alloys by in situ synchrotron X-ray diffraction* 2012: Scientific Publishing.
58. Sneddon, I.N., *The Relation Between Load and Penetration in The axisymmetric Boussinesq Problem for a Punch of Arbitrary Profile*. International Journal of Engineering Science, 1965. **3**: p. 47-57.
59. Schneider, A.S., et al., *Effect of pre-straining on size effect in molybden pillars*. Philosophical Magazine Letters, 2010.
60. Volkert, C.A. and E.T. Lilleodden, *Size effects in the deformation of sub-micron Au columns*. Philosophical Magazine, 2006. **86**(33-35): p. 5567-5579.
61. Kim, J.-Y., D. Jang, and J.R. Greer, *Insight into the deformation behavior of niobium single crystals under uniaxial compression and tension at the nanoscale*. Scripta Materialia, 2009. **61**(3): p. 300-303.
62. Han, S.M., et al., *Size effects on strength and plasticity of vanadium nanopillars*. Scripta Materialia, 2010. **63**(12): p. 1153-1156.
63. Schneider, A.S., et al., *Influence of orientation on the size effect in bcc pillars with different critical temperatures*. Materials Science and Engineering: A, 2011. **528**(3): p. 1540-1547.
64. Ng, K.S. and A.H.W. Ngan, *Stochastic theory for jerky deformation in small crystal volumes with pre-existing dislocations*. Philosophical Magazine, 2008. **88**(5): p. 677-688.



65. Greer, J.R., C.R. Weinberger, and W. Cai, *Comparing the strength of f.c.c. and b.c.c. sub-micrometer pillars: Compression experiments and dislocation dynamics simulations*. *Materials Science and Engineering: A*, 2008. **493**(1-2): p. 21-25.
66. Friák, M., M. Šob, and V. Vitek, *Ab initio study of the ideal tensile strength and mechanical stability of transition-metal disilicides*. *Physical Review B*, 2003. **68**(18): p. 184101.
67. Brenner, S.S., *Tensile Strength of Whiskers*. *Journal of Applied Physics*, 1956. **27**(12): p. 1484-1491.
68. Fukamachi, M., *Surface Orientation Dependence of the Tensile Strength of Plates of Iron Single Crystal*. *Japanese Journal of Applied Physics*, 1972. **11**(9): p. 1259.
69. Parthasarathy, T.A., et al., *Contribution to size effect of yield strength from the stochastics of dislocation source lengths in finite samples*. *Scripta Materialia*, 2007. **56**(4): p. 313-316.
70. Christian, J.W., *Some surprising features of the plastic deformation of body-centered cubic metals and alloys*. *Metallurgical Transactions A*, 1983. **14**(7): p. 1237-1256.
71. Sestak, B. and A. Seeger, *Slip and Work Hardening in bcc Metals and Alloys - 2. GLEITUNG UND VERFESTIGUNG IN KUBISCH-RAUMZENTRIERTEN METALLEN UND LEGIERUNGEN - 2.*, 1978. **69**(6): p. 355-363.
72. Schneider, A.S., et al., *Correlation between Critical Temperature and Strength of Small-Scale bcc Pillars*. *Physical Review Letters*, 2009. **103**(10): p. 105501.
73. Kiener, D., C. Motz, and G. Dehm, *Micro-compression testing: A critical discussion of experimental constraints*. *Materials Science and Engineering: A*, 2009. **505**(1-2): p. 79-87.
74. Azevedo, R.G., et al., *A SiC MEMS Resonant Strain Sensor for Harsh Environment Applications*. *Sensors Journal, IEEE*, 2007. **7**(4): p. 568-576.
75. Lee, S.-W., et al., *Cold-temperature deformation of nano-sized tungsten and niobium as revealed by in-situ nano-mechanical experiments*. *Science China Technological Sciences*, 2014. **57**(4): p. 652-662.

## Appendix A: Pillar dimensions

**Table 12: Pillar dimensions after FIB fabrication, including the aspect ratio and tapering angel.**

	Height, $h$	Top diameter, $d_t$	Base diameter, $d_b$	Aspect ratio, $h/d_t$	Taper angel, $\alpha$
Orientation <235>, red grain					
Pillar 1	2,84	1	1,45	2,8	
Pillar 2	3,47	963nm	1,45	3,6	4
Pillar 3	3,52	940nm	1,42	3,7	
Pillar 4	3,44	963nm	1,38	3,6	
Pillar 5	3,57	1	1,43	3,57	
Pillar 6	3,57	1	1,40	3,57	
Pillar 7	3,60	930nm	1,43	3,87	
Pillar 8	3,22	1	1,45	3,22	
Orientation <149>, blue grain					
Pillar 1	3,59	1	1,50	3,59	
Pillar 2	3,38	1	1,51	3,38	
Pillar 3	3,29	1	1,40	3,29	
Pillar 4	3,58	1	1,53	3,58	
Pillar 5	3,66	950nm	1,60	3,85	
Pillar 6	3,54	1	1,50	3,54	
Orientation <011>, green grain					
Pillar 1	2,79	750nm	1,16	3,72	
Pillar 2	3,08	800nm	1,20	3,85	

## Appendix B: Load-displacement curves

Orientation  $\langle 149 \rangle$ :

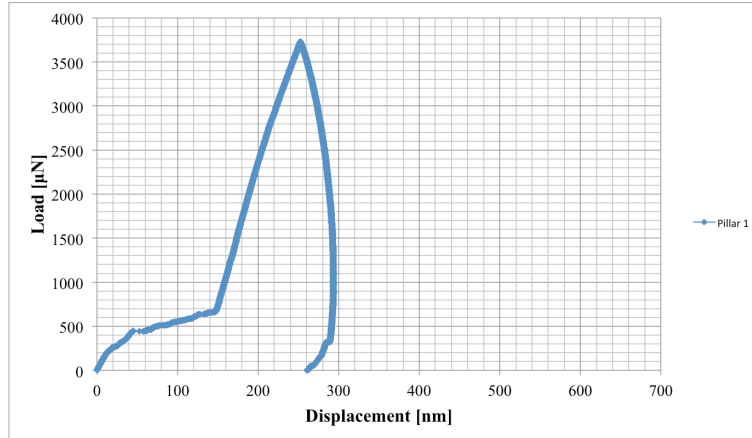


Figure 63: Load-displacement curve from  $\langle 149 \rangle$  oriented pillar 1.

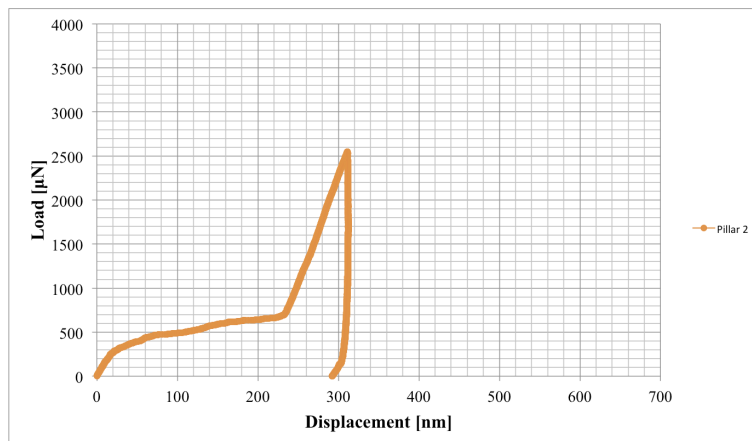


Figure 64: Load-displacement curve from  $\langle 149 \rangle$  oriented pillar 2.

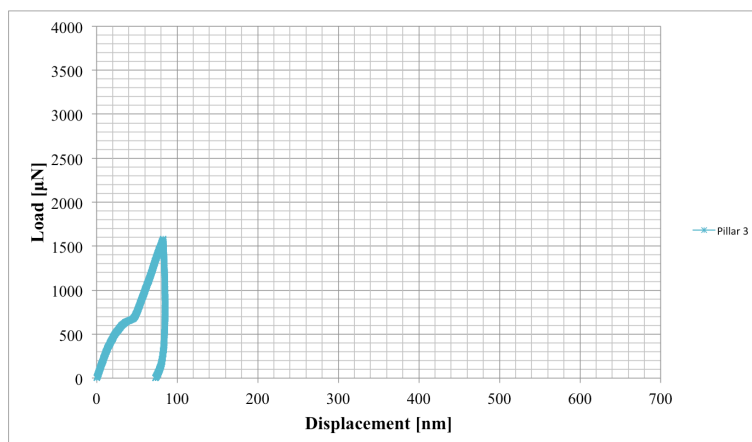
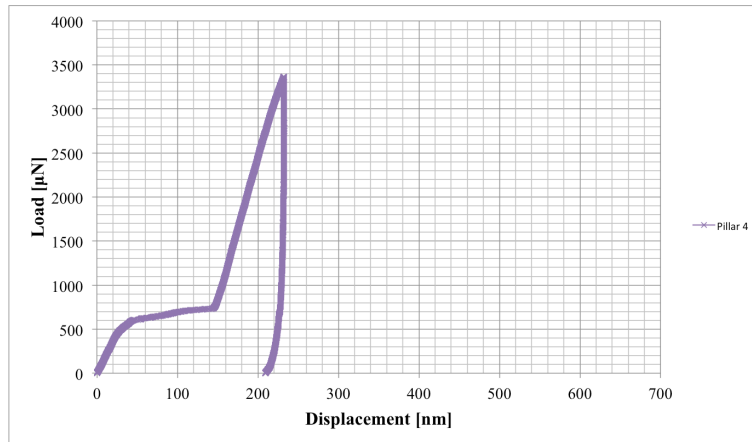
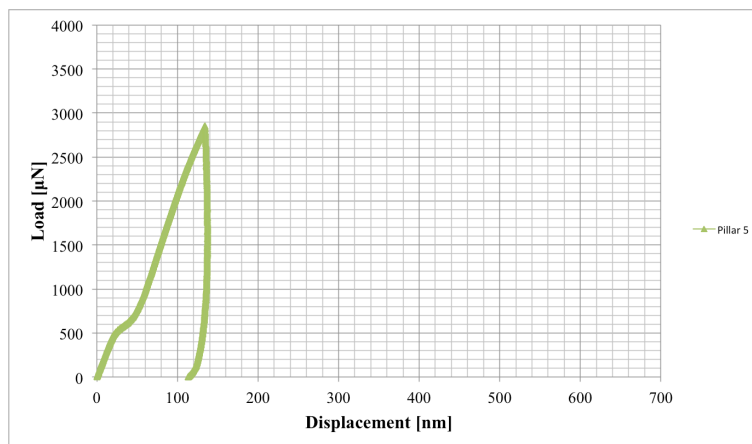


Figure 65: Load-displacement curve from  $\langle 149 \rangle$  oriented pillar 3.



**Figure 66: Load-displacement curve from <149> oriented pillar 4.**



**Figure 67: Load-displacement curve from <149> oriented pillar 5.**

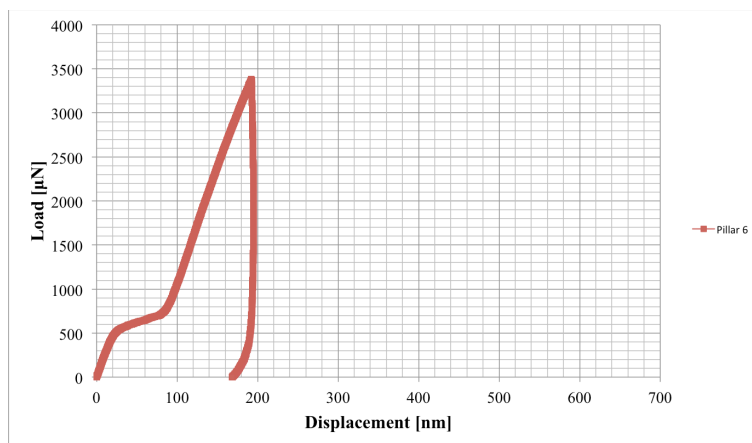


**Figure 68: Load-displacement curve from <149> oriented pillar 6.**

Orientation  $\langle 235 \rangle$ :

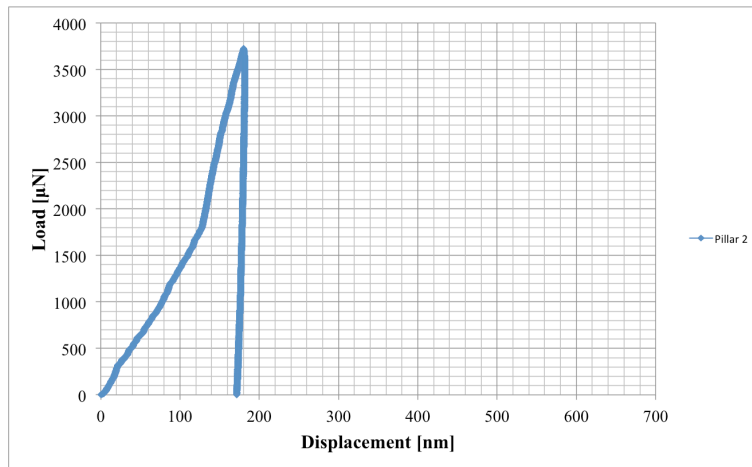


Figure 69: Load-displacement curve from  $\langle 149 \rangle$  oriented pillar 2.

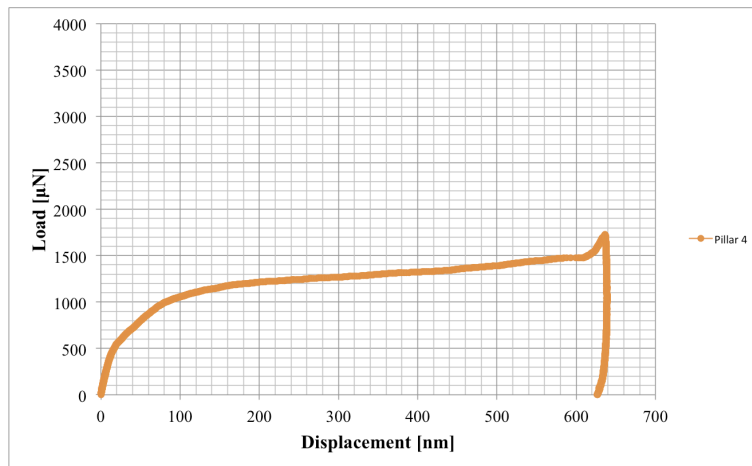


Figure 70: Load-displacement curve from  $\langle 149 \rangle$  oriented pillar 4.

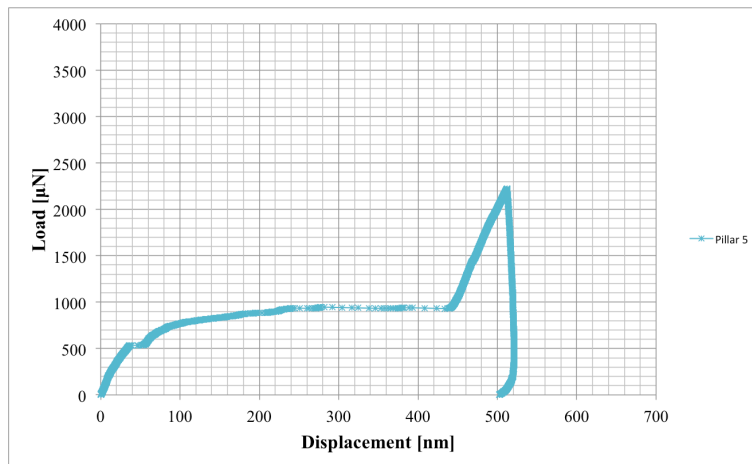


Figure 71: Load-displacement curve from  $\langle 149 \rangle$  oriented pillar 5.

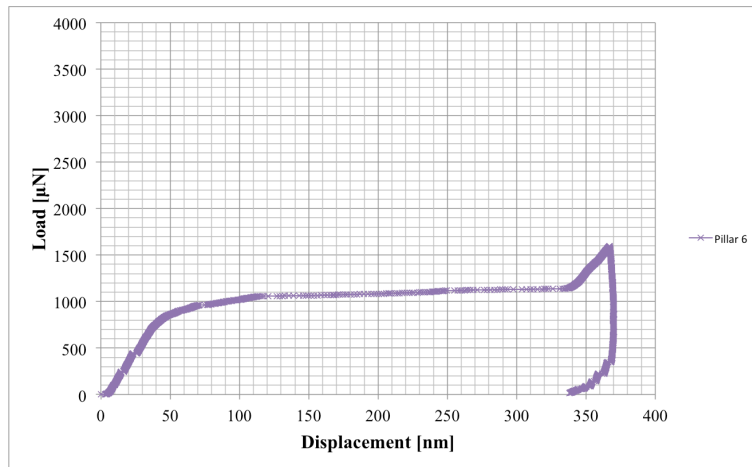


Figure 72: Load-displacement curve from <149> oriented pillar 6.

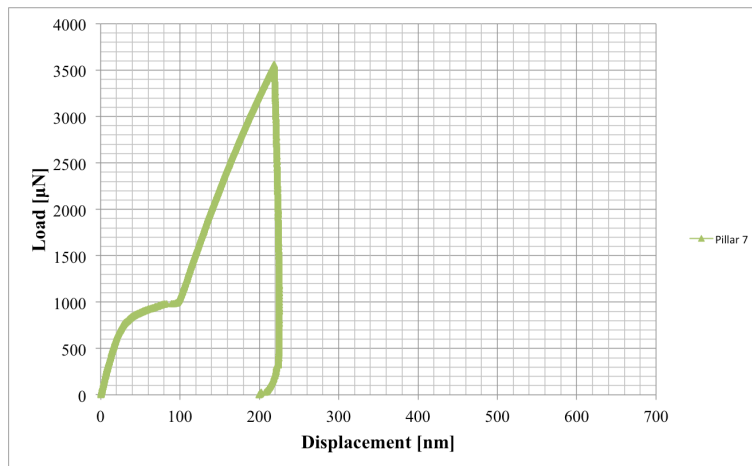


Figure 73: Load-displacement curve from <149> oriented pillar 7.

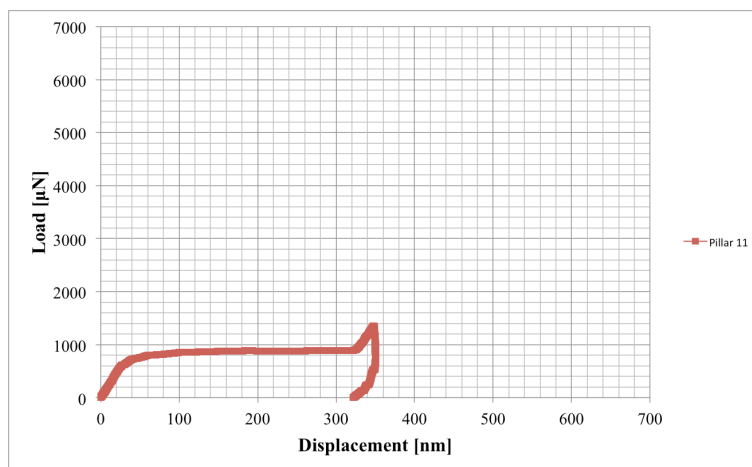


Figure 74: Load-displacement curve from <149> oriented pillar 11.

## Appendix C: Pillars post compression

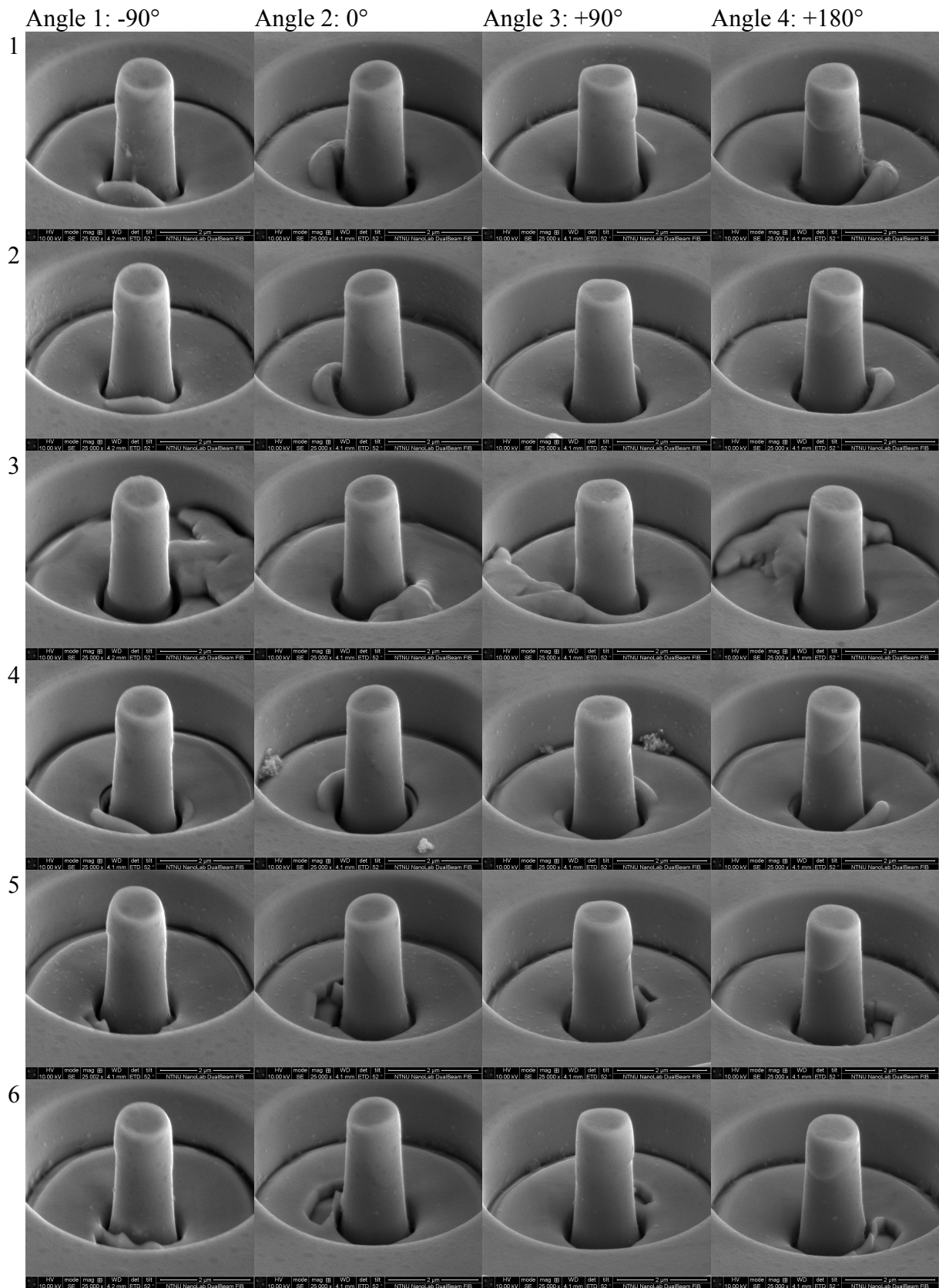
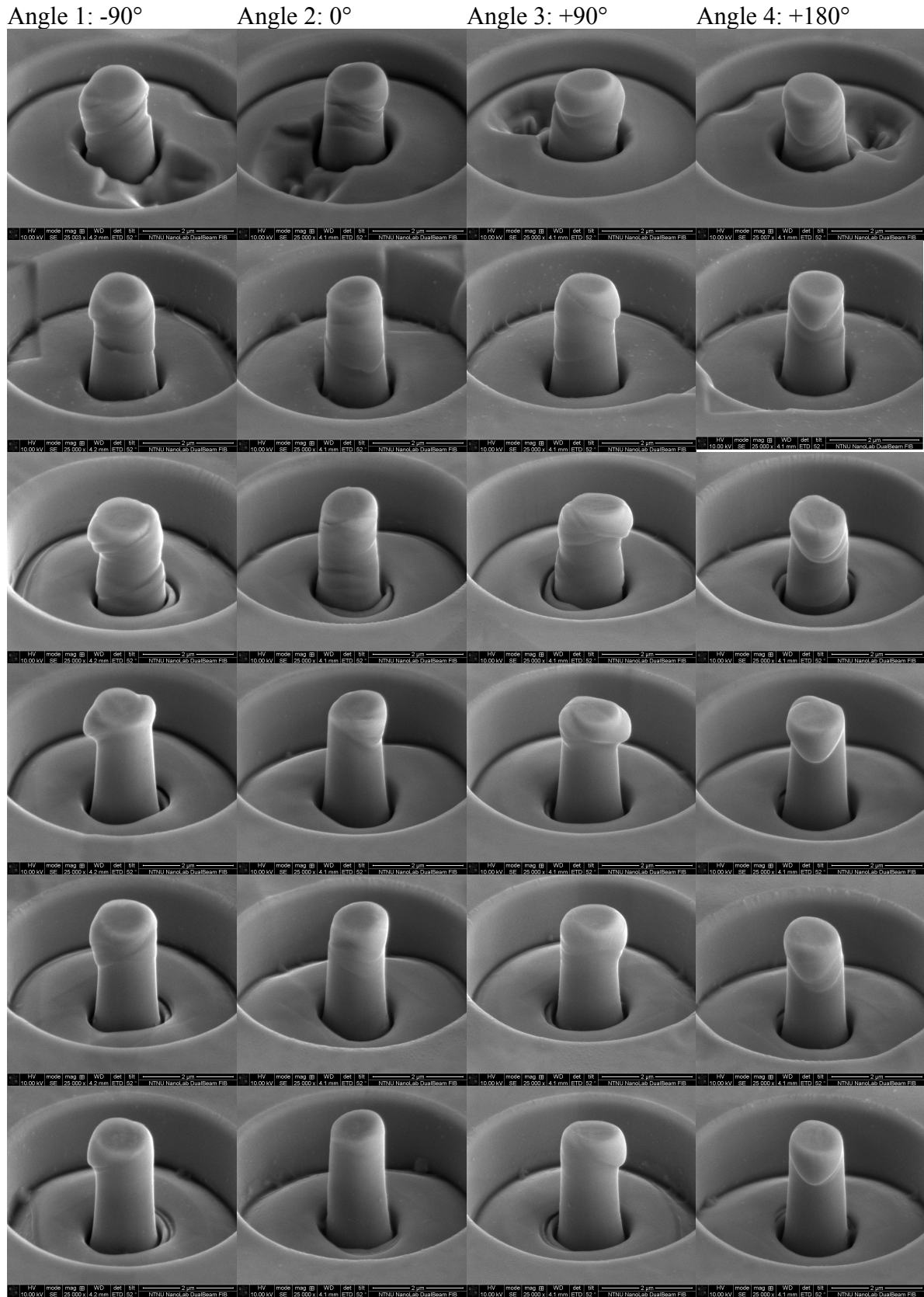


Figure 75: Post compression SEM images of  $\langle 149 \rangle$ -oriented pillars, numbered and viewed from four positions with  $90^\circ$  between each image.

# Orientation <235>





11

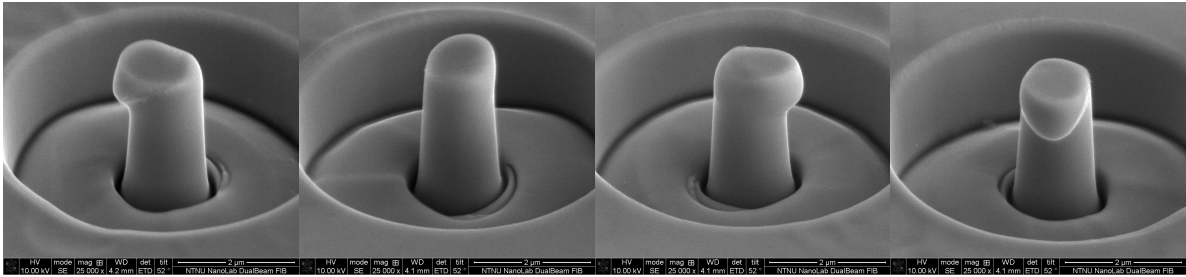


Figure 76: post compression SEM images of  $\langle 235 \rangle$  oriented pillars, numbered and viewed from four positions with  $90^\circ$  between each image.

### Orientation $\langle 011 \rangle$

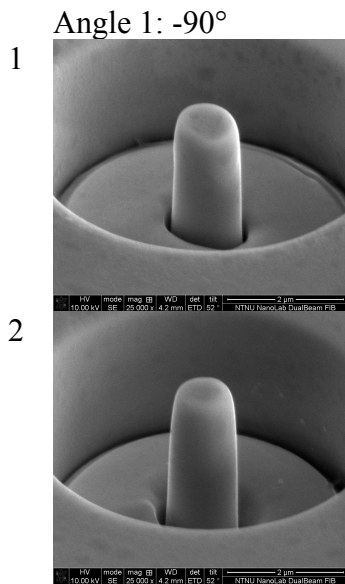


Figure 77: Post compression SEM images of  $\langle 011 \rangle$  oriented pillars, numbered and viewed from one position.

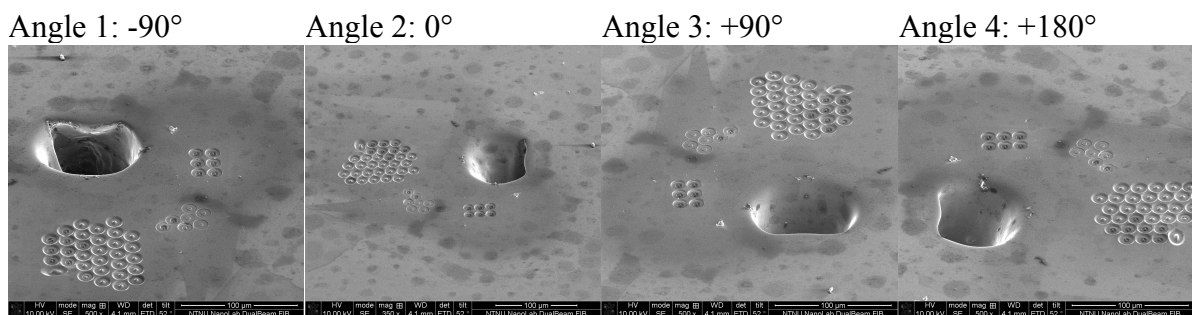


Figure 78: SEM image of the grains used for pillar fabrication imaged in the four similar angles as the pillars.

## Appendix D: Stress-strain

Orientation <149>:

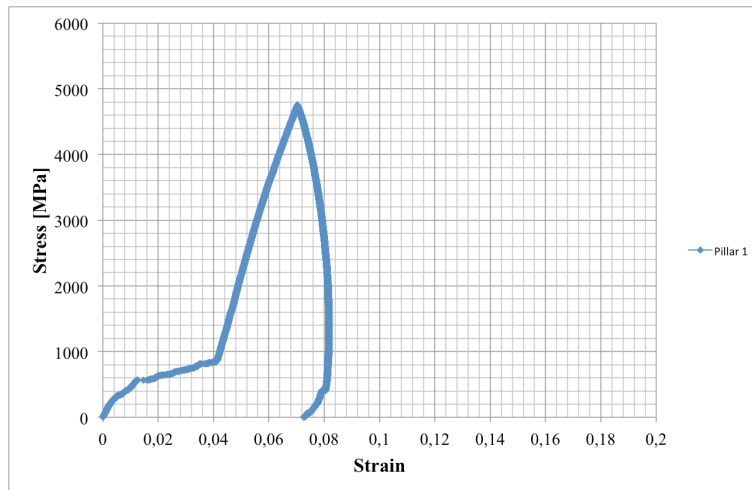


Figure 79: Stress-strain data from <149> oriented pillar 1.

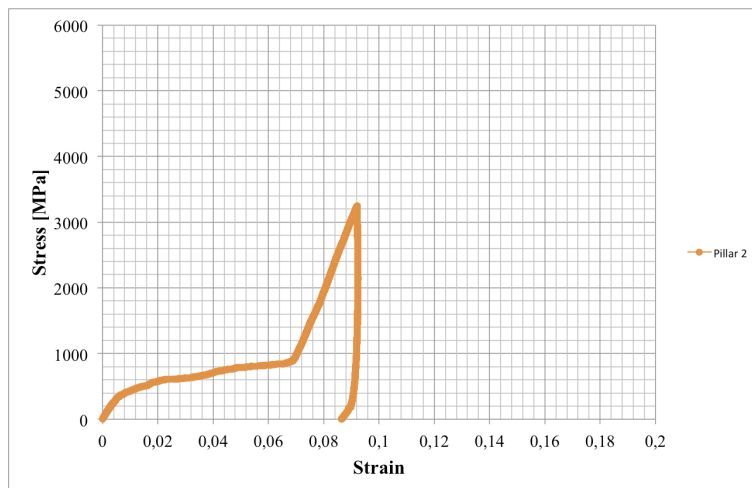


Figure 80: Stress-strain data from <149> oriented pillar 2.

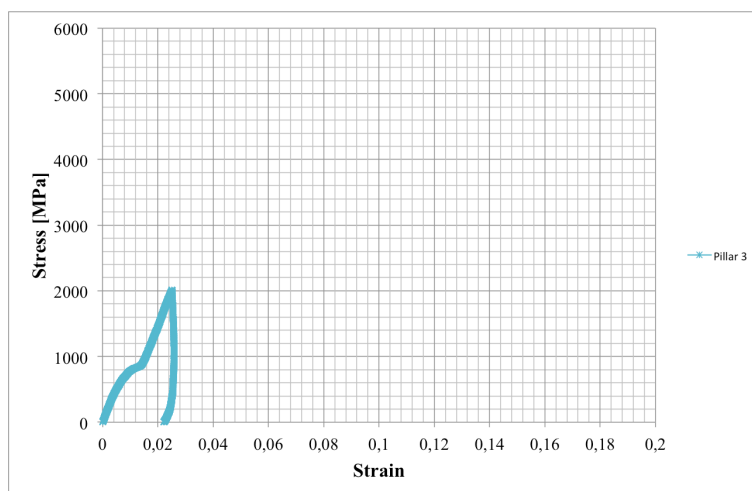


Figure 81: Stress-strain data from <149> oriented pillar 3.

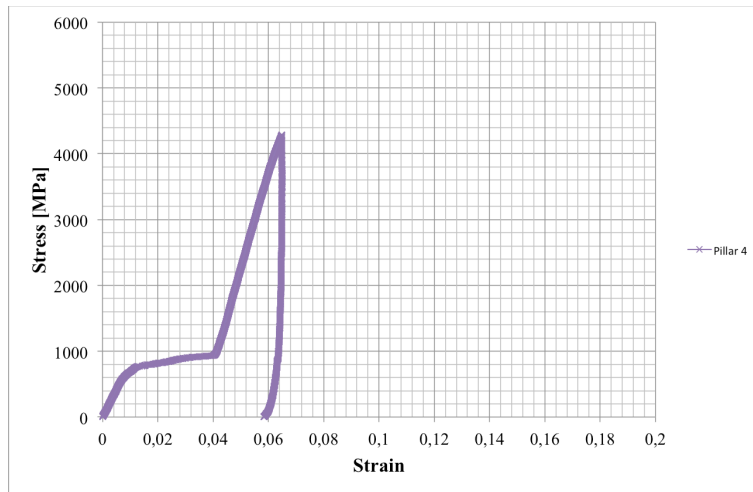


Figure 82: Stress-strain data from <149> oriented pillar 4.

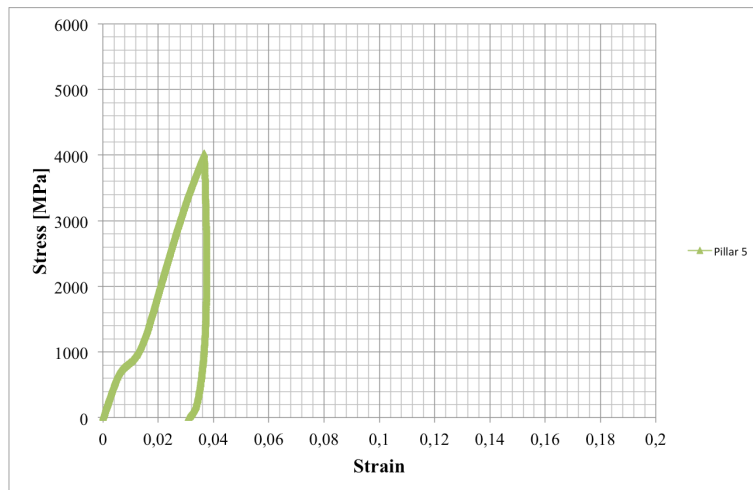


Figure 83: Stress-strain data from <149> oriented pillar 5.

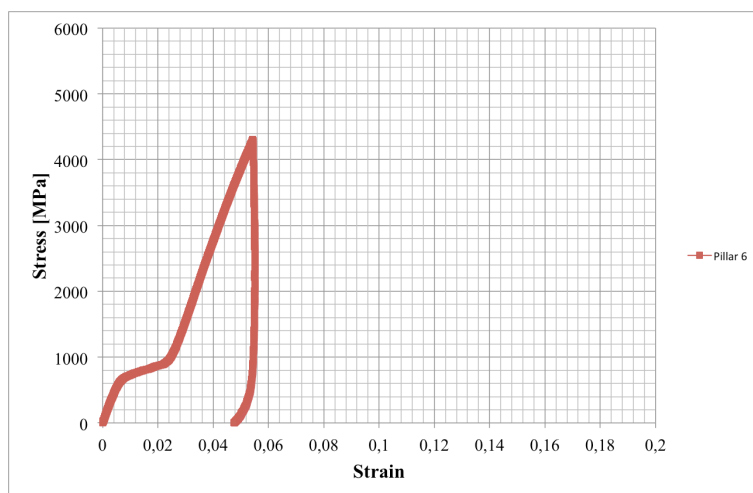
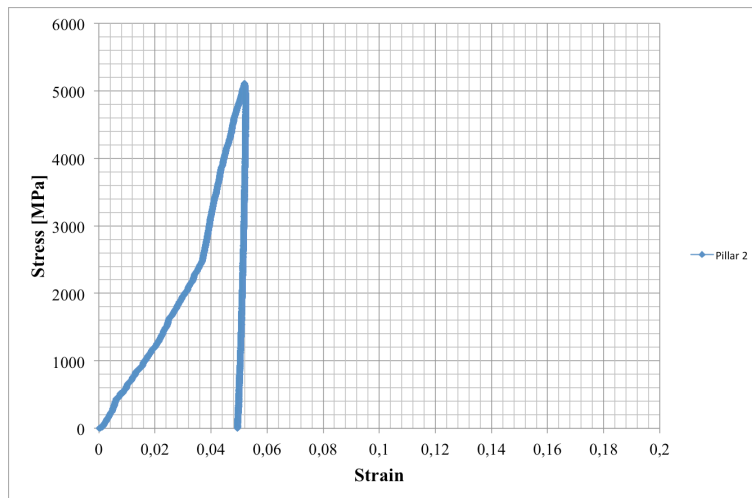
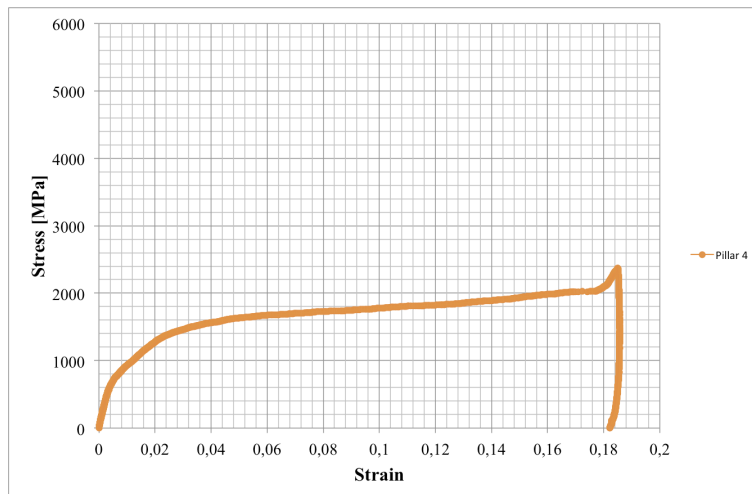


Figure 84: Stress-strain data from <149> oriented pillar 6.

**Orientation <235>:**



**Figure 85: Stress-strain data from <235> oriented pillar 2.**



**Figure 86: Stress-strain data from <235> oriented pillar 4.**

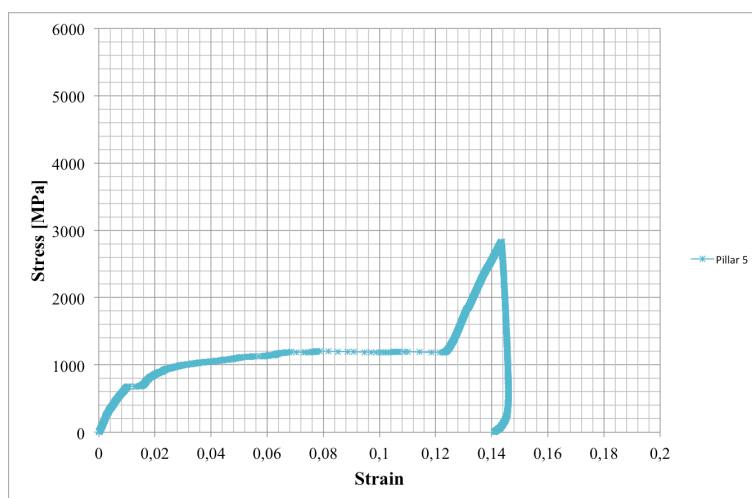


**Figure 87: Stress-strain data from <235> oriented pillar 5.**

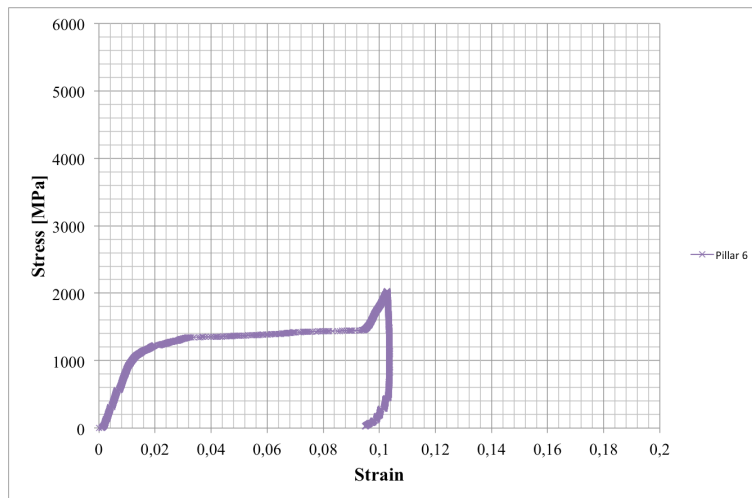


Figure 88: Stress-strain data from <235> oriented pillar 6.

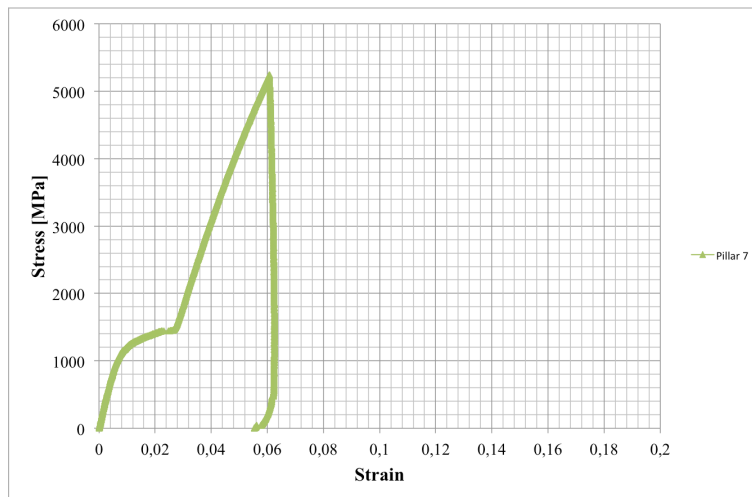


Figure 89: Stress-strain data from <235> oriented pillar 7.

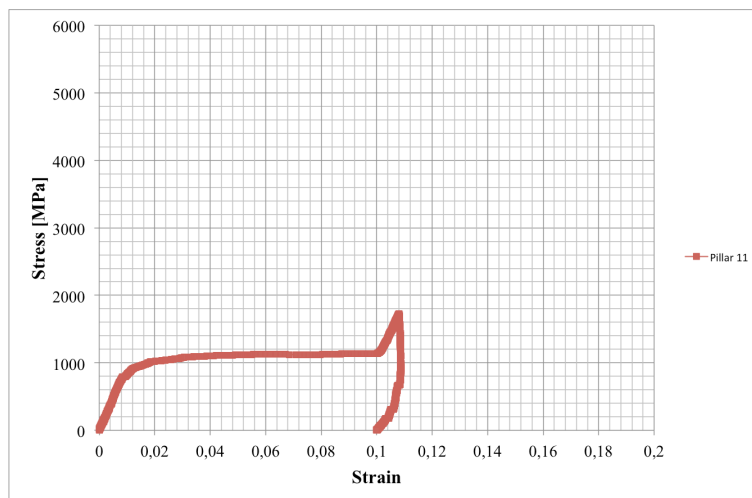


Figure 90: Stress-strain data from <235> oriented pillar 11.

# Appendix E: Thermal drift data

## Drift corrections

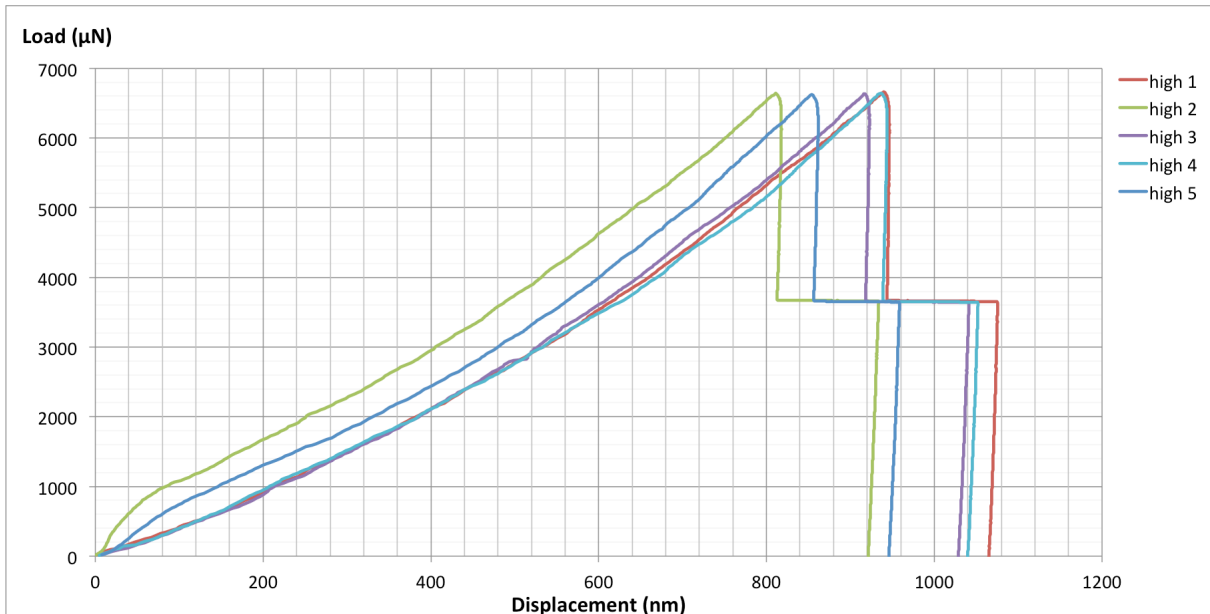


Figure 91: Load vs displacement at room temperature (29°C), with no drift correction

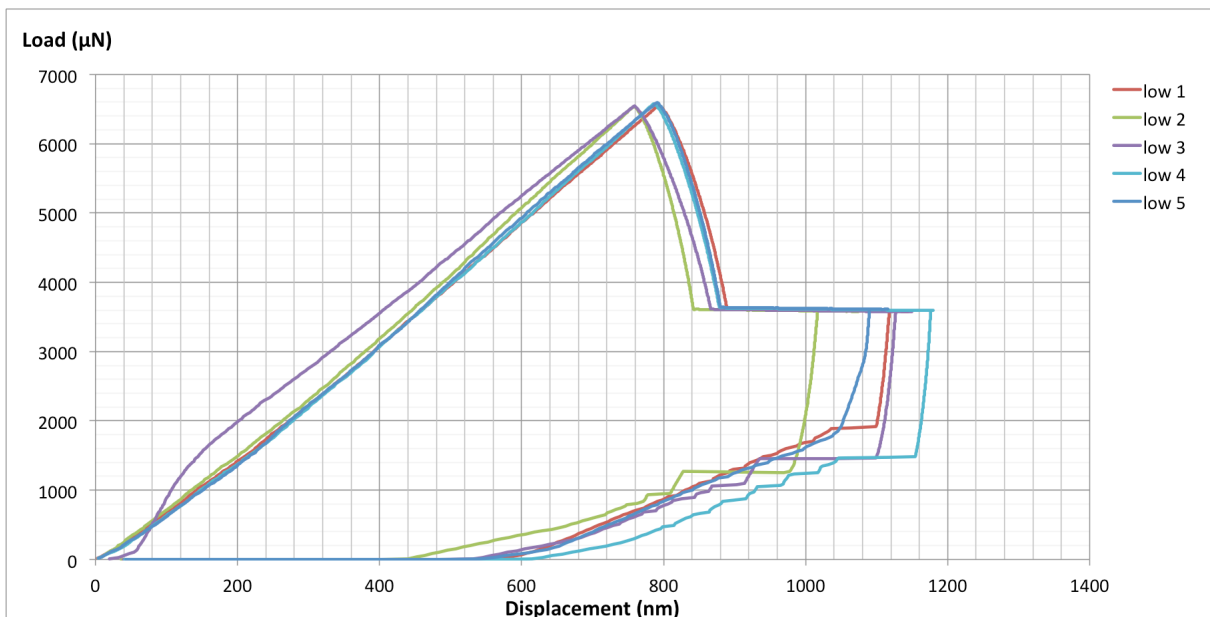


Figure 92: Load vs. displacement at low temperature (-88°C), with no drift correction

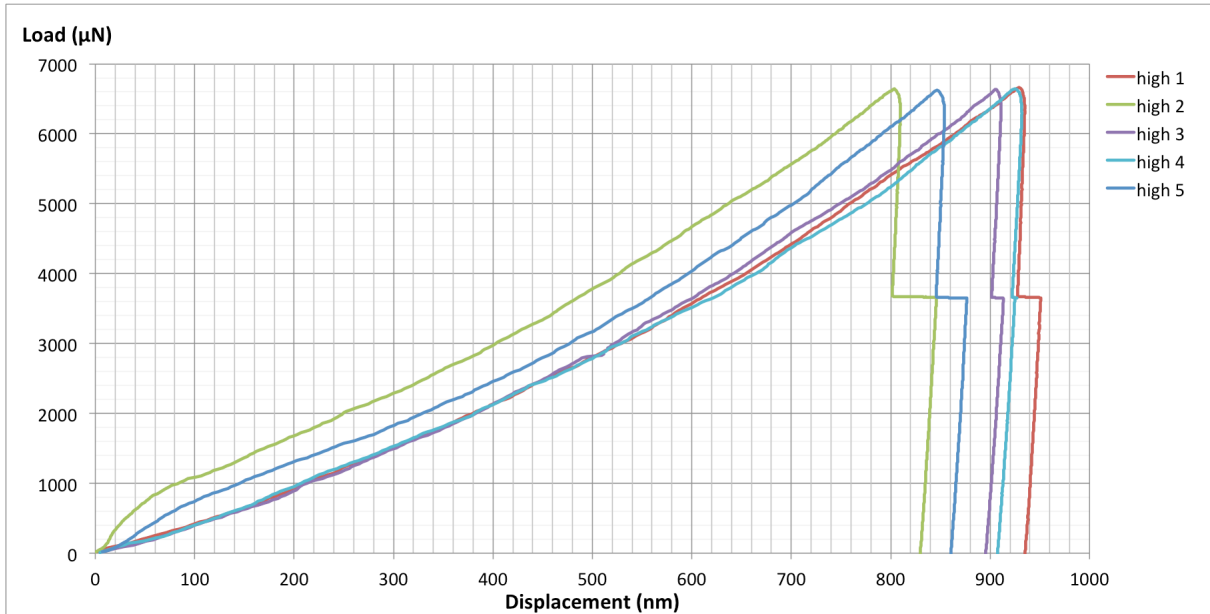


Figure 93: Load vs. displacement at room temperature (29°C), with automated drift correction

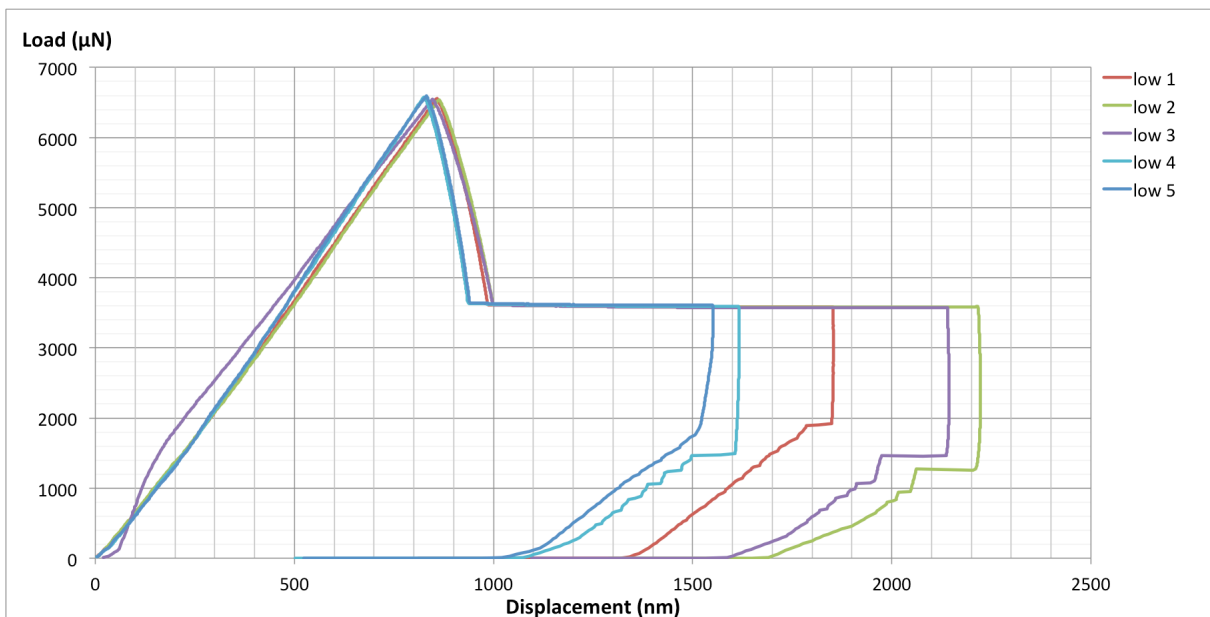


Figure 94: Load vs. displacement at low temperature (-88°C), with automated drift correction

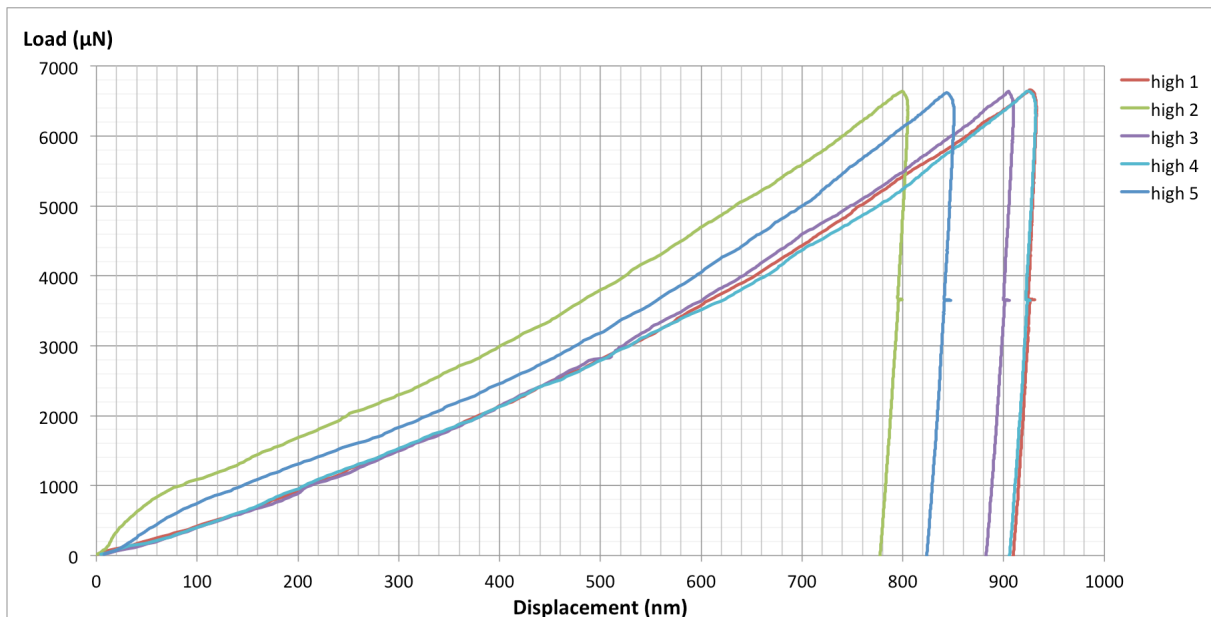


Figure 95: Load vs. displacement at room temperature ( $29^{\circ}\text{C}$ ), with manual drift correction

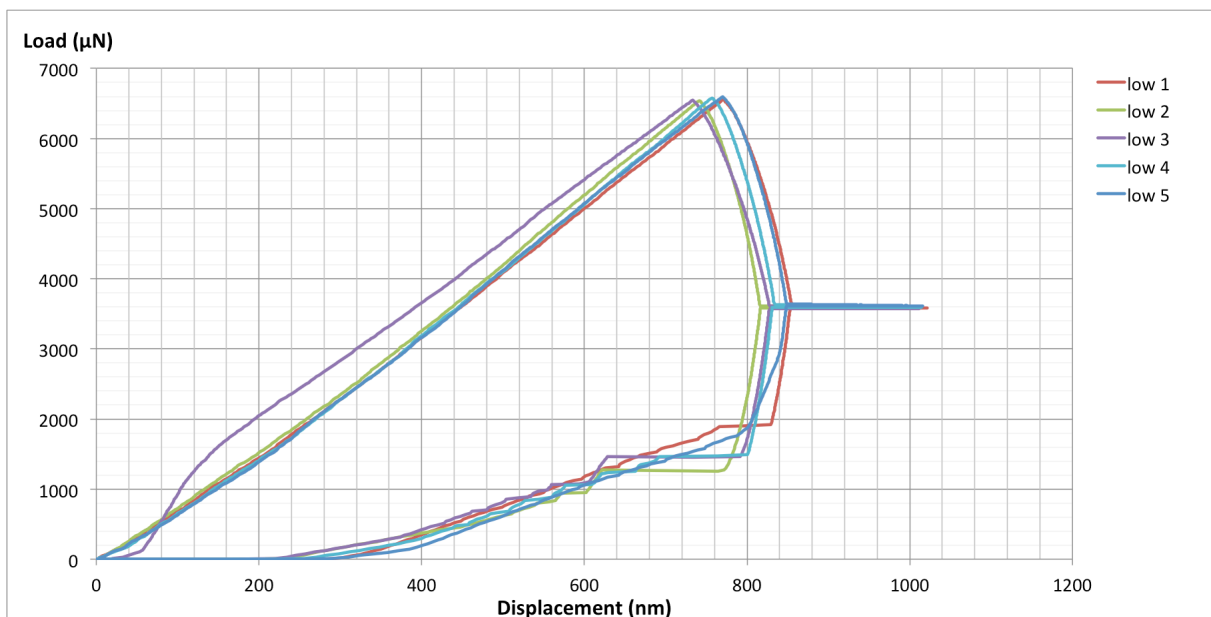


Figure 96: Load vs. displacement at low temperature ( $-88^{\circ}\text{C}$ ), with manual drift correction



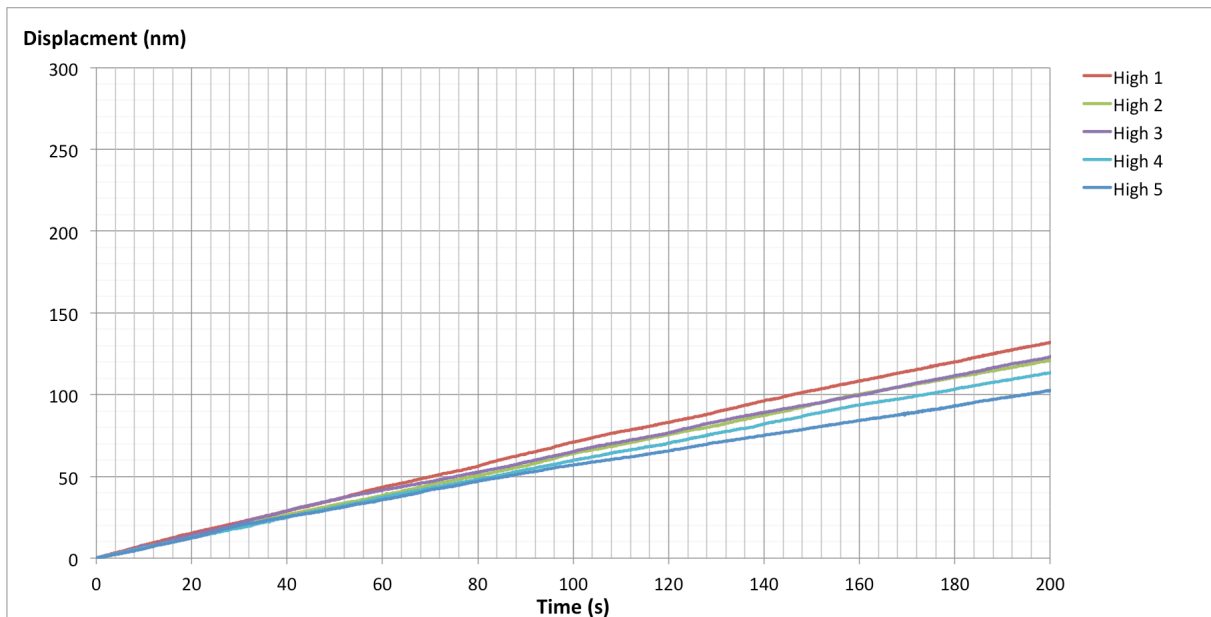


Figure 97: Displacement vs. time at room temperature (29°C)

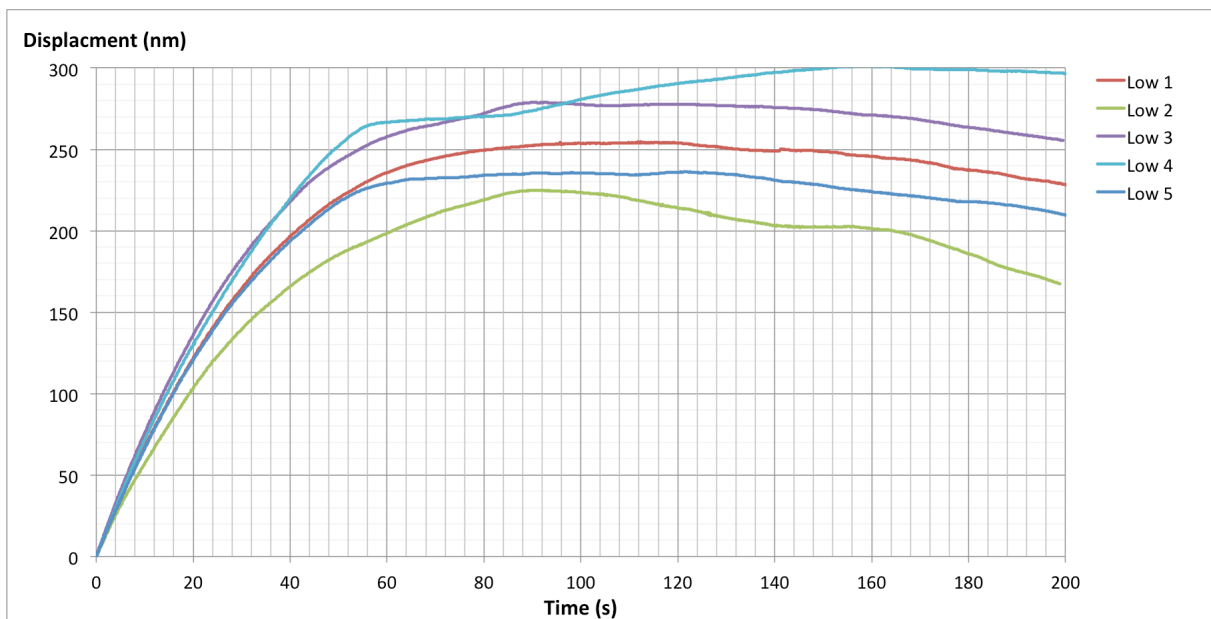
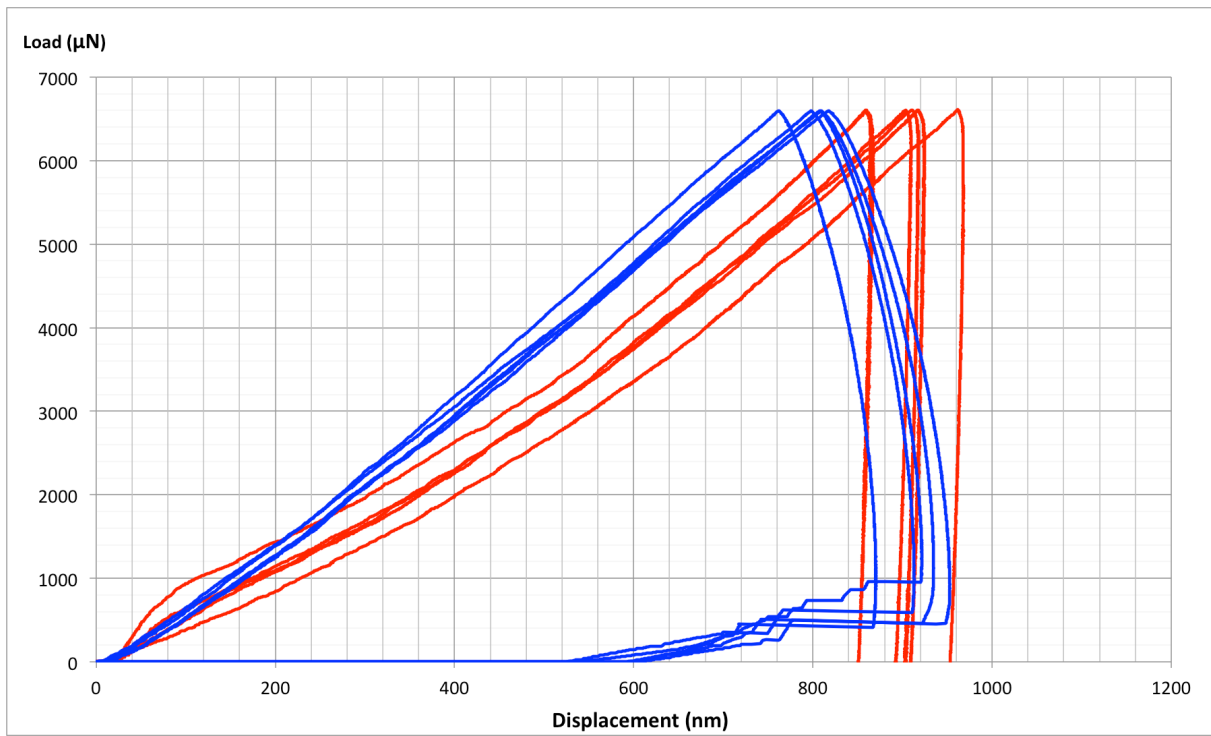


Figure 98: Displacement vs. time at low temperature (-88°C)



**Figure 99: Single indents, the blue graphs are for low temperature (-88°C), the red graphs are for room temperature (29°C)**

# Appendix F: Master thesis Posters

Department of  
Engineering  
Design  
and Materials  
  
Master Thesis  
2014

In-situ Compression testing of  
Nanosized pillars

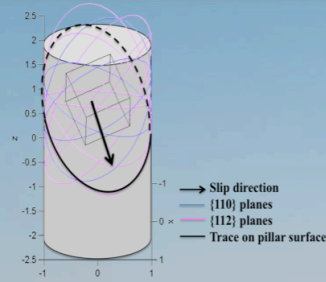
By  
Anette Brocks Hagen



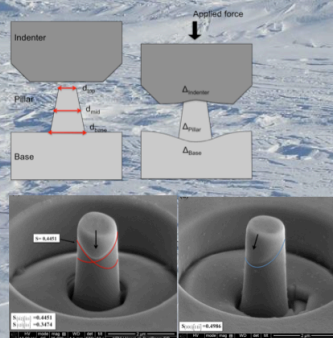
Supervisor: Prof. Dr. Christian Thaulow



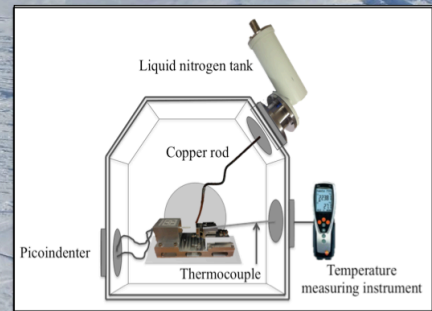
Nanocompression tests was performed with a Picoindenter mounted inside a SEM in order to continuously observe the deformation process *in-situ*. By using a cooling system consisting of a liquid-nitrogen cold finger, the pillar compression tests were conducted at low temperatures (-90°C) related to arctic conditions. From the compression testing, the recorded load-deformation relationships was used for further analyzing together with observed slip traces on the pillar surface.



Slip trace analysis performed after compression tests.



Micropillars after compression with analysed slip traces.



Sample mounted on PicoIndenter and cooled down with a coldfinger connected to a liquid nitrogen tank.

Department of  
Engineering  
Design  
and Materials  
  
Master Thesis  
2014

In-situ Compression testing of  
Nanosized pillars

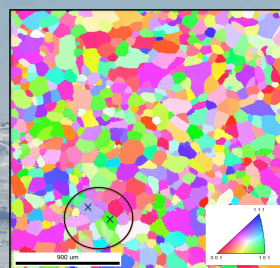
By  
Anette Brocks Hagen



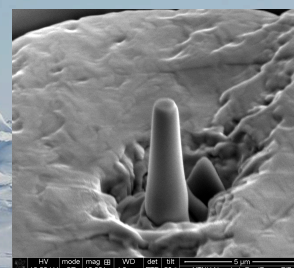
Supervisor: Prof. Dr. Christian Thaulow



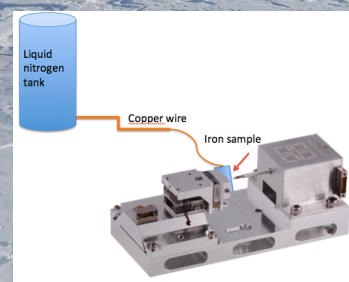
Nanocompression shall be performed with a Picoindenter mounted inside a SEM in order to continuously observe the deformation process *in-situ*. By using a cooling system consisting of a liquid-nitrogen cold finger, the pillar compression shall be conducted at low temperatures (-60°C) related to arctic conditions. From the compression testing, the recorded load-deformation relationships will be used for further analyzing in order to get a detailed understanding of the deformation mechanisms.



EBSD analysis for grain orientation location



Micro-nano pillar fabrication by Focused Ion Beam



Sample mounted on PicoIndenter and cooled down with a copper wire connected to a liquid nitrogen tank.

# Appendix G: Poster submitted to Nanobrücken workshop

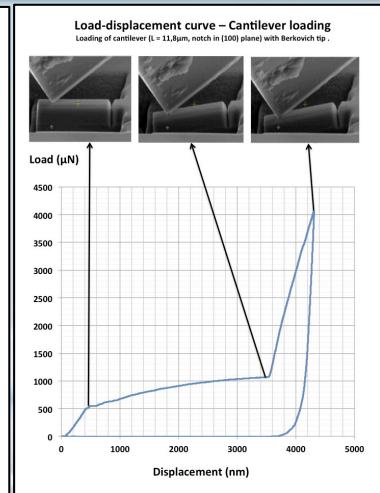
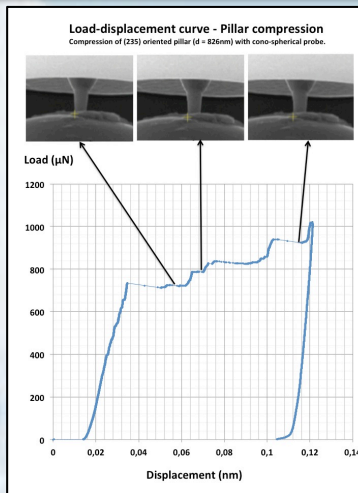
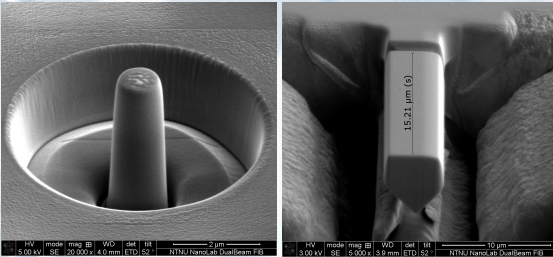
## IN-SITU COMPRESSION- AND FRACTURE MECHANICAL TESTING OF NANOSTRUCTURES

The arctic is an appealing new ventures area. However the environment is extremely demanding due to harsh climate and low temperatures, down to  $-60^{\circ}\text{C}$ . At this temperature the brittle behavior of materials is of great concern. By cooling the samples during in-situ testing, valuable information about active slip systems, local deformation behavior, fracture toughness and CTOD at low temperatures may be obtained.

In-situ nanomechanical testing has shown to be a valuable method, suitable for analyzing local deformation behavior.

Nanomechanical testing procedure:

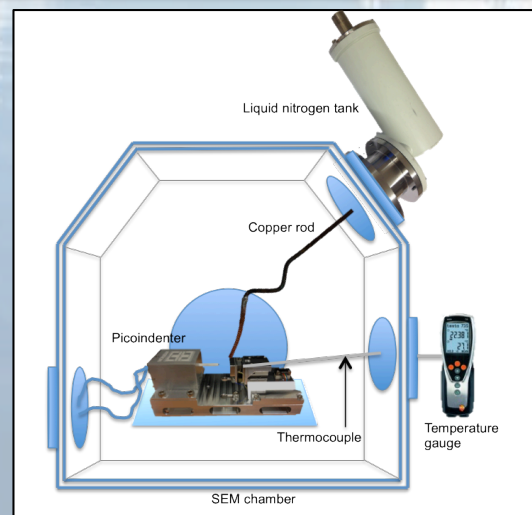
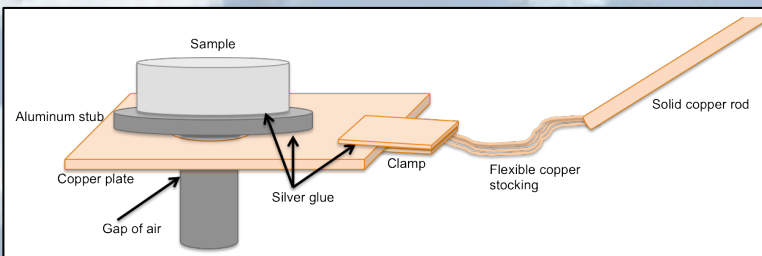
- Electron Backscatter Diffraction to determine crystallographic orientation
- Microsized cantilevers and nanosized pillars were fabricated using Focused Ion Beam milling
- In-situ loading and compression



Further work include cooling of the sample during in-situ nanomechanical testing, in order to obtain information about deformation behavior at low temperatures.

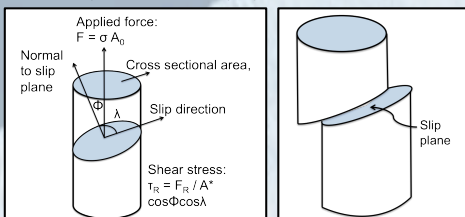
Cooling set-up during in-situ testing:

- The sample will be cooled down to about  $-60^{\circ}\text{C}$
- A liquid nitrogen tank will be mounted to the SEM port and connected to the sample by a thermal conductive set-up
- Silver glue will be used between the parts to ensure a stable set-up and good thermal conductivity
- The sample temperature will be measured with thermocouples



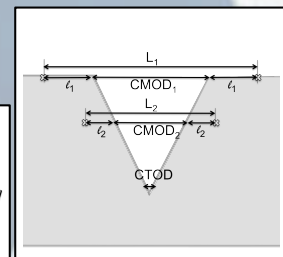
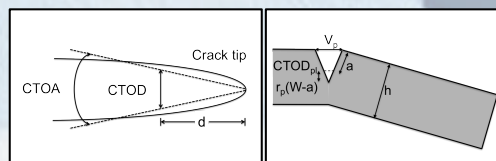
**Crystallographic slip:**

- CRSS produced on slip system



**Crack tip opening displacement (CTOD):**

- Direct measurement
- Hinge model
- Double gauge method/  $\delta_5$



Kristine Greina<sup>1</sup>, Anette Brocks Hagen<sup>1</sup>, Professor Christian Thaulow<sup>1</sup>, Bjørn R. S.


Rogne<sup>1</sup>, Afroz Barnoush<sup>1</sup>, Nousha Kheradmand<sup>1</sup> and Odd Magne Akselsen<sup>2</sup>

<sup>1</sup>The Norwegian University of Science and Technology (NTNU), Department of Engineering Design and Materials (IPM), Trondheim, Norway.

<sup>2</sup>SINTEF Materials and chemistry, Trondheim, Norway.

[krisgrei@stud.ntnu.no](mailto:krisgrei@stud.ntnu.no)

# Appendix H: Risk evaluation

NTNU	Risikovurdering				Utarbeidet av	Nummer	Dato
					HMS-avd.	HMSRV2601	22.03.2011
HMS					Godkjent av	Rektor	01.12.2006

**Enhet:**

**Linjeleder:**

**Deltakere ved kartleggingen (m/ funksjon):** Anette Brocks Hagen (Master student), Christian Thaulow (hovedveileder), Bjørn Rune Rogne (PhD)  
**Risikovurderingen gjelder hovedaktivitet:** Masteroppgave student Anette Brocks Hagen. IN-SITU COMPRESSION TESTING OF NANOSIZED PILLARS

**Signaturer:** Ansvarlig veileder: *Anette Brocks Hagen*

Student: *Anette B. Hagen*

**Dato:** 20 januar 2014

ID nr	Aktivitet fra kartleggings-skjemaet	Mulig uønsket hendelse/ belastning	Vurdering av sannsynlighet (1-5)	Vurdering av konsekvens:				Risiko-Verdi (menneske)	Kommentarer/status Forslag til tiltak
				Menneske (A-E)	Ytre miljø (A-E)	Øk/ materiell (A-E)	Om-dørme (A-E)		
	Use of FIB	Voltage Radiation Gallium-gas	1	E	D	D	A	1E	Good protection for voltage and radiation
	Use of FIB	Damage on equipment	3	A	A	C	B	3A	Risk is minimized with proper training
	Use of SEM	Voltage radiation	1	E	D	D	A	1D	Good protection for voltage and radiation
	Use of SEM	Damage on equipment	3	A	A	C	B	3C	Risk is minimized with proper training
	Use of liquid nitrogen	cold burns	1	E	A	A	A	1E	caution when working with liquid nitrogen
	Use of liquid nitrogen	asphyxiation	1	E	B	B	A	1E	Follow safety instructions in the risk assessment.

NTNU	Kartlegging av risikofylt aktivitet			Utarbeidet av	Nummer	Dato
HMS				HMS-avd.	HMSRV2601	22.03.2011
		Godkjent av		Erstatter		
		Rektor		01.12.2006		

**Dato:** 20 januar 2014

**Enhet:**  
**Linjeleder:**  
**Deikere ved kartleggingen (m/ funksjon):** Anette Brocks Hagen (Master student), ChristianThaulow (hovedveileder), Bjørn Rune Rogne (PhD)  
**Kort beskrivelse av hovedaktivitet/hovedprosess:** Masteroppgave student Anette Brocks Hagen. IN-SITU COMPRESSION TESTING OF NANOSIZED PILLARS

**Er oppgaven rent teoretisk? (JA/NEI):** Nei  
**Signaturer:** Ansvarlig veileder: *Ju. Thaulow* Student: *Anette B. Hagen*

ID nr.	Aktivitet/prosess	Ansvarlig	Eksisterende dokumentasjon	Eksisterende sikringstiltak	Lov, forskrift o.l.	Kommentar
	Use of Focused Ion Beam (FIB)	Anette B. Hagen	User safety manual	FIB-course (NanoLab) Cleanroom course	User Guide	
	Use of Scanning Electron Microscope (SEM) combined with PicoIndenter	Bjørn Rune Rogne/ Anette B. Hagen	User safety manual	SEM-seminar Training session	User Guide	
	Cleaning of material surface in ethanol	Anette B. Hagen	Data sheet for ethanol		Ventilation room	
	use of liquid nitrogen (transport, storage, filling, use)	Anette B. Hagen/ Jorleif Hjeltn	Risk assessment for working with liquid nitrogen	instruktion by an employee who is aware of the risks involved		

NTNU	Risikovurdering			Utarbeidet av	Nummer	Dato
				HMS-avd.	HMSRV/2601	22.03.2011
HMS				Godkjent av		Erstatter
				Rektor		01.12.2006



**Sannsynlighet vurderes etter følgende kriterier:**

Svært liten 1	Liten 2	Middels 3	Stor 4	Svært stor 5
1 gang pr 50 år eller sjeldnere	1 gang pr 10 år eller sjeldnere	1 gang pr år eller sjeldnere	1 gang pr måned eller sjeldnere	Skjer ukentlig

**Konsekvens vurderes etter følgende kriterier:**


Gradering	Menneske	Ytre miljø Vann, jord og luft	Øk/materiell	Omdømme
E Svært Alvorlig	Død	Svært langvarig og ikke reversibel skade	Drifts- eller aktivitetsstans > 1 år.	Troverdighet og respekt betydelig og varig svekket
D Alvorlig	Alvorlig personskade. Mulig uførhet.	Langvarig skade. Lang restitusjonstid	Driftsstans > ½ år Aktivitetsstans i opp til 1 år	Troverdighet og respekt betydelig svekket
C Moderat	Alvorlig personskade.	Mindre skade og lang restitusjonstid	Drifts- eller aktivitetsstans < 1 mnd	Troverdighet og respekt svekket
B Liten	Skade som krever medisinsk behandling	Mindre skade og kort restitusjonstid	Drifts- eller aktivitetsstans < 1uke	Negativ påvirkning på troverdighet og respekt
A Svært liten	Skade som krever førstehjelp	Ubetydelig skade og kort restitusjonstid	Drifts- eller aktivitetsstans < 1dag	Liten påvirkning på troverdighet og respekt

**Risikoverdi = Sannsynlighet x Konsekvens**

Beregn risikoverdi for Menneske. Enheten vurderer selv om de i tillegg vil beregne risikoverdi for Ytre miljø, Økonomi/materiell og Omdømme. I så fall beregnes disse hver for seg.

**Til kolonnen "Kommentarer/status, forslag til forebyggende og korrigerende tiltak":**

Tiltak kan påvirke både sannsynlighet og konsekvens. Prioriter tiltak som kan forhindre at hendelsen inntreffer, dvs. sannsynlighetsreduserende tiltak foran skjerpet beredskap, dvs. konsekvensreduserende tiltak.

NTNU		Risikomatrix		Dato	
				08.03.2010	
HMS/KS				Erstatter	
		utarbeidet av		Nummer	
		HMS-avd.		HMSRY2604	
		godkjent av			
		Rektor		09.02.2010	



**MATRISSE FOR RISIKOVURDERINGER ved NTNU**

KONSEKVENSENS	Svært alvorlig	E1	E2	E3	E4	E5
	Alvorlig	D1	D2	D3	D4	D5
	Moderat	C1	C2	C3	C4	C5
	Liten	B1	B2	B3	B4	B5
	Svært liten	A1	A2	A3	A4	A5
	Svært liten	Liten	Middels	Stor	Svært stor	
<b>SANNSYNLIGHET</b>						

**Prinsipp over akseptkriterium. Forklaring av fargene som er brukt i risikomatriksen.**

Farge	Beskrivelse
Rød	Uakseptabel risiko. Tiltak skal gjennomføres for å redusere risikoen.
Gul	Vurderingsområde. Tiltak skal vurderes.
Grønn	Akseptabel risiko. Tiltak kan vurderes ut fra andre hensyn.